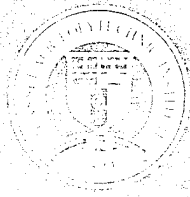


Final Technical Report

STATIC AND FATIGUE DAMAGE IN  
HIGH TEMPERATURE COMPOSITES

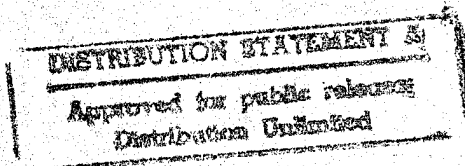


Rensselaer

19951206 032

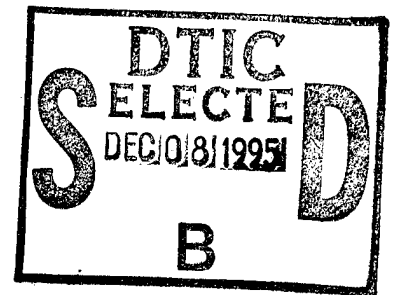
Rensselaer Polytechnic Institute

Troy, New York 12180



DTIC QUALITY INSPECTED 1

Final Technical Report



STATIC AND FATIGUE DAMAGE IN  
HIGH TEMPERATURE COMPOSITES

by

G.J. Dvorak and Y.A. Bahei-El-Din

Department of Civil and Environmental Engineering  
and  
Center for Composite Materials and Structures  
Rensselaer Polytechnic Institute  
Troy, New York 12180-3590

Submitted to  
Dr. Walter F. Jones

Air Force Office of Scientific Research  
110 Duncan Avenue, Suite B115  
Bolling Air Force Base, Washington, DC

Contract Number F-4962092-J-0391

September 14, 1995

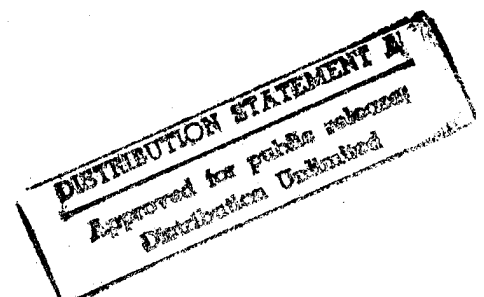


# TABLE OF CONTENTS

	PAGE
ABSTRACT	3
1. INTRODUCTION	4
2. EXPERIMENTAL INVESTIGATION OF ISOTHERMAL STATIC AND FATIGUE BEHAVIOR OF SIGMA/TIMETAL 21S LAMINATES	6
2.1 Materials and Specimens	6
2.2 Experiments	7
2.3 The Neat Matrix	8
2.4 Laminates	9
3. MODELING OF THERMOMECHANICAL BEHAVIOR OF HIGH TEMPERATURE METAL MATRIX COMPOSITE LAMINATES	15
3.1 Constitutive Equations of the Fiber and Matrix	15
3.2 Micromechanical Models of Composite Laminates	19
3.2.1 Model selection	19
3.2.2 Transformation field analysis	19
3.2.3 Modeling of interface damage	24
3.2.4 Finite element scheme	25
3.3 Interpretation of Isothermal Static and Fatigue Data of Sigma/Timetal 21S Laminates	28
3.3.1 Hot isostatic pressing	28
3.3.2 Static loading	30
3.3.3 Isothermal load cycles	31
4. CONCLUSIONS	34
ACKNOWLEDGEMENT	35
REFERENCES	36
APPENDIX	41
TABLES	43
FIGURES	49

Accession For	
NTIS GRA&I	<input checked="" type="checkbox"/>
DTIC TAB	<input type="checkbox"/>
Unannounced	<input type="checkbox"/>
Justification	
By	
Distribution/	
Availability Codes	
Dist	Avail and/or Spec
A-1	

## ABSTRACT

This final report presents the experimental and theoretical work performed in our research program on static and fatigue damage in high temperature composites. The theoretical part focused on development and implementation of a new Transformation Field Analysis (TFA) for inelastic laminates, which employs unit-cell, periodic array models, as well as averaging micromechanical models together with any constitutive law for thermo-viscoplastic and other inelastic deformation. Moreover, we have initiated modeling of damage by debonding and frictional sliding at the fiber interface, using the TFA computational scheme and the finite element method.

In the experimental program, we examined the effect of static and cyclic loading (at 0.1 and 0.001 Hz) on the inelastic response of and damage development in  $(0)_4$ ,  $(0/90)_s$  and  $(0/\pm 45/90)_s$  SiC/Ti (Sigma/Timetal 21S) laminates, and the Timetal 21S matrix, at 650°C and 21°C. At the elevated temperature, viscoplastic deformation of the matrix can be observed even at relatively low applied stresses. At both temperatures, reduction of unloading elastic moduli of the laminates, which indicates onset of damage by interface decohesion, also starts after loading to relatively low stresses. The cyclic loading rate has no effect on endurance of the  $(0/90)_s$  and  $(0/\pm 45/90)_s$  laminates loaded by constant amplitude tension at 650°C. In the  $(0)_4$  laminate, higher endurance limits were detected at 0.1 Hz than at 0.001 Hz. However, regardless of rate and layup, the total strain at failure under both static and cyclic loading at 650°C, was measured at  $1 \pm 0.1\%$ .

The experimental results are interpreted by micromechanical models developed in the theoretical work. The effects of temperature and time variations on the constitutive response of the matrix and fiber are considered. The results show that the inelastic deformation of the titanium matrix, assisted by extensive fiber debonding in the off-axis plies, promotes stress transfer to the fibers in the 0-degree plies. Under repeated loads, the fiber strain increase gradually at a certain rate, which depends on the applied load frequency, and the laminate fails when the fiber strain reaches a critical value.

## 1. INTRODUCTION

Fatigue failure in fibrous composite laminates is typically associated with internal stress redistribution during cyclic loading that results in stress buildup and overloading of the fibers in certain plies. Under axial loading of laminated plate specimens used in most experiments, this happens in the fibers of the 0-degree plies. Several distinct mechanisms may participate in the stress redistribution. For example, in inviscid elastic-plastic systems at room temperature, matrix cracking and/or fiber-matrix debonding in the off-axis plies causes reduction of stiffness of the damaged plies, so that an increasing part of the applied load is supported by the axial plies.

A different mechanism operates in the present SiC/Ti system at elevated temperatures, where the matrix is viscoplastic and thus its deformation depends on the time spent at a particular load level. While both static strength and isothermal endurance limits of such laminates are relatively high, it is well known that both the lack of thermomechanical compatibility between the fiber and matrix, and the relatively low strength of the fiber-matrix interface, make the laminates susceptible to interface decohesion, fiber sliding, matrix cracking, and other forms of distributed damage. Environmental exposure is also a factor at higher temperatures. For example, the hold time at maximum stress in isothermal fatigue tests performed in a high temperature air environment can severely decrease the fatigue life of a titanium matrix composite [1]. The stress amplitude, frequency, and the ratio of maximum to minimum stress have all been found to affect the fatigue behavior of unidirectional composites under isothermal as well as thermomechanical loading conditions [2-5]. Failure is generally preceded with matrix transverse cracking and caused by overloading the fibers.

Similar effects accompanied with more complex damage mechanisms have been observed in titanium matrix laminates. Under isothermal, and in-phase thermomechanical fatigue loading, debonding of the off-axis plies is the dominant damage mode [6-8].

Time-dependent deformation of the matrix is significant under isothermal and in-phase loading conditions [5, 8-10]. In contrast, matrix flow is nearly absent under out-of-phase thermomechanical load cycles. In this case, microcracking of the matrix followed by fiber breakage is the dominant damage mode. In any event, failure of the composite is again caused by overloading the fibers in the  $0^\circ$  plies.

In this report, we present the results of isothermal, at  $21^\circ\text{C}$  and  $650^\circ\text{C}$ , static and cyclic loading experiments, and their theoretical interpretation, on  $(0)_4$ ,  $(0/90)_s$  and  $(0/\pm 45/90)_s$  Sigma/Timetal 21S laminates. Elastic and inelastic response, damage accumulation detected by measuring changes in secant and unloading elastic moduli, and failure strains were recorded. While there are many differences in the behavior of the tested laminates, it turns out that the strains at failure are remarkably consistent and independent of loading conditions. At room temperature the axial strain in the  $0^\circ$  ply is in the range of 0.5-0.6%, while at  $650^\circ\text{C}$  this strain, including the thermal strain, was equal to 0.9-1.1%.

The experimentally observed fatigue behavior of the Sigma/Timetal 21S laminates have been simulated by micromechanical models. A summary of the theoretical approach for analysis of fibrous composite laminates is presented and followed by numerical simulations of the experiments. The results indicate that cyclic loading, combined with fabrication and processing, produce complex internal stress states in the plies and in the fiber and matrix phases and cause interface decohesion by sliding or separation under overall loads which are only a fraction of the ultimate strength. Comparison of the predicted results with experimental data suggest that fiber overloading is responsible for fatigue failure under constant temperature. At failure, the computed overall axial strains for all laminates fall within a narrow band of  $1.0 \pm 0.1\%$ , which compares favorably with the strain range measured experimentally.

## 2. EXPERIMENTAL INVESTIGATION OF ISOTHERMAL STATIC AND FATIGUE BEHAVIOR OF SIGMA/TIMETAL 21S LAMINATES

### 2.1 Materials and Specimens

The material studied herein is a Timetal 21S matrix reinforced by continuous aligned Sigma fibers. The Timetal 21S material is a metastable beta titanium alloy with the composition (Ti-15Mo-3Nb-3Al-.2Si) produced in foil form by TIMET, Inc., Denver, Colorado. The Sigma fiber is a silicon-carbide monofilament with a structured carbon-titanium boride coating manufactured by British Petroleum. The fiber diameter is  $100\mu\text{m}$  (0.004 in.). Fabrication of silicon-carbide/titanium composite panels typically involves hot isostatic pressing of alternating layers of titanium foil and tapes of aligned fibers, held in place by molybdenum wires. In particular, the Sigma/Timetal 21S composite panels, supplied by Wright Laboratories, were pressed at  $899^{\circ}\text{C}$  ( $1650^{\circ}\text{F}$ ) under a hydrostatic pressure of 103.5 MPa (15 Ksi) for 2 hours. Subsequent treatment involved aging at  $621^{\circ}\text{C}$  ( $1150^{\circ}\text{F}$ ) for 8 hours in a vacuum of  $10^{-5}$  torr.

The material was received as flat plate panels, measuring 210 mm (8.25 in.) in direction of the  $0^{\circ}$  fiber, in three layups,  $(0)_4$ ,  $(0/90)_s$ , and  $(0/\pm 45/90)_s$ . C-scan images of the laminated panels provided by the manufacturer did not reveal any major defects. The fiber volume fraction computed from cross section images taken for the received panels was found to be 28.2% for the  $(0)_4$  unidirectional composite, 32.5% for the  $(0/90)_s$  cross ply, and 34.1% for the  $(0/\pm 45/90)_s$  laminate. An unreinforced plate manufactured by hot isostatic pressing of Timetal 21S foil was also received for evaluation of the neat matrix properties. Specimens with straight edges were cut from the panels using a diamond cutoff wheel. At 3000 rpm and a feed rate of 8 mm per minute, this cutting method preserved the laminate integrity at the cut section and provided a smooth edge. The nominal width of the specimens was 10 mm (0.4 in.) for the neat matrix specimens and the  $(0)_4$  laminate, and 12.5 mm (0.5 in.) for the  $(0/90)_s$  and the  $(0/\pm 45/90)_s$  laminates. Surfaces of the

specimens were chemically cleaned before testing. Aluminum tabs were bonded to the ends of the specimens using 3M single part epoxy adhesive and cured at 107°C (225°F). The tabs were 1.6 mm (1/16 in.) thick and 25.4 mm (1.0 in.) long, providing a clear length of 160 mm (6.25 in.) for heating the gauge area and cooling the grips as explained in the next section.

## 2.2 Experiments

Axial mechanical loading of the specimens was applied by a MTS 810 uniaxial testing machine through screw loaded flat grips. Heating of the specimens was achieved by a steel succesor tube which enclosed the specimen and was heated by direct induction using a 5 KW solid state heating unit. The succesor tube was 25.4 mm (1.0 in.) in diameter and 100.0 mm (4.0 in.) long. This allowed cooling water pipes to be installed adjacent to the grips. Temperature measurements and control were performed with thermocouples. Figure 1 shows the temperature profile measured along a Sigma/Timetal specimen heated in the succesor furnace. A uniform temperature was maintained in the 50.8 mm (2.0 in.) long center zone, while the grips were kept at room temperature.

Strain measurements were made using a MTS high temperature extensometer with alumina rods 25.4 mm (1.0 in.) apart. The extensometer rods have 45° knife edges which were mounted at the specimen edge through holes drilled in the succesor furnace. Mounting the extensometer rods at the specimen edge rather than the flat side prevented bending of the specimen by the rods pressure.

Both static and fatigue tests were conducted on the neat matrix and the composite laminate specimens at a constant temperature as described in the subsequent sections. The load and temperature control, and the data aquisition were performed by a dedicated personal computer.

### 2.3 The Neat Matrix

The time-dependent behavior of the Timetal 21S material under static loading at 650°C was examined in a multistep creep test. Load was applied at 50 MPa/min to stress levels of 50, 75, 100, 125, and 150 MPa and maintained for 6 hours, Fig. 2. The thermal strain caused by heating the specimen from room temperature to 650°C was found to be 0.61%. Under static loading at 650° the Young's elastic modulus was 64.0 GPa and the yield strength 30.0 MPa. The total strain recorded under the multistep creep load is also shown in Fig. 2. The creep strain rates corresponding to each stress level are shown in Fig. 3. Data from these and related available experiments were utilized in finding matrix elastic and viscoplastic properties, reported in Tables 5 and 6.

Secondary creep at low stress levels, and tertiary creep at high stress levels dominate the response to monotonic or sustained loads at 650°C. The matrix specimen sustained total strain of 10% in this experiment. Of course, in a composite reinforced by stiff fibers, the matrix strain will be limited by the ultimate fiber strain of about 1%. We note that the *in situ* matrix stresses are generated by a complex thermomechanical loading path induced by hot isostatic pressing, cooling to room temperature, reheating to annealing temperature, and after another cooling cycle, to the test temperature of 650°C. Inelastic deformation during these load cycles, and damage development that accompanies the experimental loading program, both contribute to the final stress values. Figures 2 and 3 suggest that even at low stress levels, matrix time-dependent behavior can be significant.

Cyclic loading experiments examined the effect of loading frequency and stress range on strain response of the Timetal 21S. Figure 4 shows the stress history applied to a neat Timetal 21S specimen at 650°C. Axial stress cycles with amplitude  $S_{\max} = 40, 100, 200,$  and 250 were applied, while the stress ratio  $R = S_{\max}/S_{\min}$  was kept constant at 0.1. The loading frequency was changed from fast at 1.0 Hz to slow at 0.01 Hz as indicated in Fig. 4. Figure 6 shows the total strain measured during the entire history applied in this experiment. The Timetal matrix exhibits significant ratcheting under cyclic loading. As

in the static loading case, the cyclic creep strain response shown in Fig. 5 tends to stabilize if the maximum stress does not exceed 200 MPa. Tertiary cyclic creep is observed under load cycles with the stress amplitude of 250 MPa. As indicated in Fig. 6, where the strain developed under each stress range is shown, the ratcheting rate of the Timetal matrix is affected by the stress amplitude and loading frequency.

## 2.4 Laminates

Three laminate layups,  $(0)_4$ ,  $(0/90)_s$ , and  $(0/\pm 45/90)_s$ , were tested under static and cyclic loads applied at constant temperatures of 650°C and 21°C. The elevated temperature experiments were designed to examine the effect of the time-dependent behavior of the matrix and of distributed damage on the overall response. The room-temperature tests were used only to evaluate damage-induced changes of elastic moduli in virgin laminate specimens loaded to different stress levels, and of specimens that survived certain cyclic loading programs at 650°C.

*Static tensile tests* at 650°C are summarized in Table 1, and plotted in Fig. 7. Two loading rates, 0.278 MPa/s and 27.8 MPa/s were employed. Stress rates of the same order were applied in the cyclic loading tests described subsequently. The elastic modulus, ultimate strength, and maximum strain at failure are indicated in Table 1 together with the thermal strains caused by heating to 650°C. The measured stress-strain response for the three laminates is shown in Fig. 7. Constitutive behavior of the Sigma/Timetal 21S composite at 650°C is clearly rate-dependent. Some rate effects in the elastic modulus and in the maximum stress and strain are observed, particularly in the  $(0/90)_s$  and  $(0/\pm 45/90)_s$  laminates, Table 1. In general, slow loading leads to lower matrix stresses and higher fiber stresses, and thus to lower overall strength, as seen in Table 1. However, regardless of the loading rate, the combined mechanical and thermal maximum strain sustained by the laminates was equal to 1.0 – 1.2%.

The laminate thermal strains at the test temperature are also shown in Table 1; they are 25 to 30% lower than the matrix thermal strain of 0.61%. Of course, this reduction is caused by the constraint imposed by the fibers, particularly by the 0-degree fibers which thus support a residual stress. For example, the computed (Section 3.3) fiber axial thermal stress after heating of initially stress-free Sigma/Timetal 21S laminates to 650°C is equal to 634 MPa in the unidirectional laminate; in the  $(0/90)_s$  and  $(0/\pm 45/90)_s$  laminates, the computed 0-degree ply fiber axial stress is equal to 800 MPa. However, these stresses are superimposed with the thermal residual stresses generated during fabrication. Cooldown from processing temperature causes high compressive axial residual stress in the fiber, hence the net axial stress in the fiber after reheating to 650°C is compressive. For the Sigma/Timetal 21S system, this stress was computed as equal to -136 MPa in the unidirectional composite (Table 7), and -55 MPa in either the  $(0/90)_s$  or the  $(0/\pm 45/90)_s$  laminate (Table 8).

The effect of the time-dependent response of the matrix on the overall response of Sigma/Timetal 21S laminates was examined by multistep creep tests. Each specimen of the  $(0)_4$ ,  $(0/90)_s$  and  $(0/\pm 45/90)_s$  laminates was heated to 650°C, and then loaded axially at 50 MPa/min, to a specific tensile stress magnitude which was sustained for 24 hours. Figure 8 shows the overall axial strain recorded in a multistep creep test for two  $(0)_4$  unidirectional specimens, one with sustained axial stress of 50, 100, 150, and 200 MPa, the other with a stress of 300, 400, and 500 MPa. A limited amount of overall creep strain was observed in this composite system due to the axial constraint imposed on the matrix by the elastic Sigma fibers. In elastic deformation at 650°C, the ratio of the matrix to overall axial stress is equal to about 0.4. Under viscoplastic deformation, the matrix stresses are gradually reduced by creep strains at decreasing rates. Figure 8 shows that the second specimen failed at 1% overall strain, after a short creep period at 500 MPa. The total creep strain accumulated in this specimen was computed as equal to 0.2%.

Higher creep strains were found in Fig. 9 for the  $(0/90)_s$ , and in Fig. 10 for the  $(0/\pm 45/90)_s$  laminate, due to the presence of the more compliant off-axis plies. However, as in the unidirectional composite, failure in the  $(0/\pm 45/90)_s$  laminate occurred at approximately 1% overall axial strain. We note that the creep test of the  $(0/\pm 45/90)_s$ , Fig. 10, was interrupted after about 20 hours (point "A" in Fig. 10) due to power failure, and was resumed at the sustained stress of 100 MPa. This caused the discontinuity in the strain rate found at point "A" in Fig. 10.

*Cyclic tensile tests* were conducted on the three laminates at various maximum stresses. The ratio of the maximum to minimum applied stresses,  $R = S_{\max}/S_{\min}$ , was kept constant at 0.1. Two load frequencies were selected, a fast cycle at 0.1 Hz, and a slow cycle at 0.001 Hz. Samples of the raw experimental data obtained for laminates are plotted in Figs. 11–22. In a typical fatigue test, a specimen was first heated to 650°C in 6 minutes and kept at this temperature for 4 minutes. The specimen was then loaded axially to the mean stress in one minute. Next, the mean stress was kept constant for one minute before application of the load cycles.

The temperature and stress histories for the unidirectional  $(0)_4$  laminate under the slow 0.001 Hz, and the fast 0.1 Hz cycles are shown in the insets of Figs. 11 and 12 which display the corresponding strain histories. The stress amplitudes were 450 MPa and 850 MPa, respectively. The recorded stress–strain response is shown in Figs. 13 and 14. Ratcheting of the titanium matrix is reflected in the overall response. Under slow load cycles, higher viscoplastic strains are generated by each load cycle, Fig. 11, hence in only few cycles, the computed *in situ* matrix stress state becomes nearly quasi-isotropic, and the overall response stabilizes. In contrast, several hundred cycles are required to reach a stable overall response when fast load cycles are applied. Similar behavior was found in the  $(0/90)_s$  cross ply, Figs. 15–18, and in the  $(0/\pm 45/90)_s$  laminate, Figs. 19–22.

While in all the tested samples the overall strain at failure is equal to about 1%, the strain accumulation per cycle depends on the loading frequency. This is particularly

evident in the  $(0/\pm 45/90)_s$  sample results shown in Figs. 19 and 20 where the amplitude of 250 MPa is constant while the loading frequency is the only variable. More than 2800 cycles at 0.1 Hz were required to bring the overall strain to the ultimate value, Fig. 20. Under the same overall stress applied at 0.001 Hz, the specimen failed in only 215 cycles.

*Fatigue experiments* conducted on the Sigma/Timetal 21S laminates are summarized in Table 2. The S-N data appear in Fig. 23, which also shows data points for failure in the first cycle, that were not included in Table 2. The observed endurance limits for  $(0/90)_s$  and  $(0/\pm 45/90)_s$  laminates are similar. The  $(0/90)_s$  crossply shows a somewhat longer fatigue life than the  $(0/\pm 45/90)_s$  laminate. Although the S-N data under the fast and slow load cycles are similar, the fatigue life of either laminate is longer at the higher loading frequency. As discussed earlier, this is caused by the slower growth of the matrix creep strains under fast load cycles. According to the data in Fig. 23, the endurance limit of the  $(0/90)_s$  crossply is 300 MPa; for the  $(0/\pm 45/90)_s$  laminate it is 200 MPa.

The unidirectionally reinforced specimens show a more pronounced effect of the loading frequency on the fatigue life, this was also reported by Nicholas and Russ [1]. However, the S-N data in Fig. 23 also indicate significant differences between fatigue lives of two batches of nominally similar unidirectional laminates. Specimens cut from the B-plate had an order of magnitude longer fatigue life than the specimens cut from the A-plate.

*Damage development* was monitored by measuring the unloading elastic moduli and secant moduli of selected specimen. Table 3 shows room-temperature results obtained for the  $(0/90)_s$  layup. One virgin or reference specimen was loaded at a slow rate to the stress levels indicated in the first column of Table 3. At each level, the initial unloading elastic modulus was measured during a complete unloading cycle. This was followed by loading to a higher level and another unloading. The Young's modulus measured during first loading was equal to 171 GPa. Table 3 also shows room-temperature unloading moduli measured by the said procedure on two specimens that survived 110000 and 113750 cycles at  $650^\circ$ ,

respectively. Ultimate failure stress levels for the three specimens are also given in the table. Table 4 presents data from similar tests performed on  $(0/\pm 45/90)_s$  laminates, where the Young's modulus measured during first loading was equal to 178 GPa.

In both laminates, the unloading moduli are lower than the respective initial (loading) magnitudes, and decrease with the rising applied stress. This is indicative of damage, such as interface debonding and sliding in the virgin reference samples, and also of matrix and fiber cracking in those exposed to isothermal fatigue, and of progressive opening of new or pre-existing separations with higher applied stresses. Indeed, matrix cracks were detected on micrographs of sectioned samples, and so was interface decohesion, but no attempt was made to quantify such observations. It is clear, however, that the present laminates are very prone to damage, even at static loads well below ultimate strength.

Damage development was also detected by measuring changes in the secant moduli computed from the hysteresis loops, such as those appearing in Fig. 13. Results obtained on two  $(0)_4$  specimens from plate "A" cycled at 0.001 Hz are shown in Fig. 24, where the secant modulus reduction is related to the overall axial strain. The initial 10–15% reduction of the secant modulus was probably caused by viscoplastic deformation of the matrix, which stabilizes after a few cycles at about 0.85–0.9% overall axial strain. Additional cycles caused further reductions in the secant modulus that continue until failure; this indicated evolution of distributed damage. In contrast, the reduced secant modulus of a  $(0)_4$  specimen from plate "B", which survived 1750 cycles at a higher maximum stress of 600 MPa, remained stable up to 0.96% overall axial strain.

*Total axial strain prior to failure* was measured on all fatigue specimens; for all three laminates the magnitudes remained within the range of  $1.0 \pm 0.1$  %, Fig. 25. Since the residual thermal and inelastic strains are mostly relieved by damage, this suggests that failure of the tested composites was caused by overloading the Sigma fibers in the  $0^\circ$  ply which can sustain an ultimate strain of approximately 1% at 650°C. This critical strain

appears to be a useful design criterion, providing that the contribution due to damage can be properly accounted for.

### 3. MODELING OF THERMOMECHANICAL BEHAVIOR OF HIGH TEMPERATURE METAL MATRIX COMPOSITE LAMINATES

#### 3.1 Constitutive Equations of the Fiber and Matrix

Both constituents are regarded as homogeneous solids with known, temperature-dependent thermo-elastic properties; both phases are isotropic in the present application, but the analysis can accommodate any actual material symmetry. The fiber remains elastic until failure. The matrix is elastic if loaded within a certain equilibrium surface in the stress space, but becomes viscoplastic if loaded beyond this surface. The inelastic response of the matrix is derived here from a unified viscoplastic theory described by Bahei-El-Din et al. [11] and Shah [12]. In either phase, the total strain rate  $\dot{\epsilon}_{ij}$  is additively decomposed into elastic, thermal, and inelastic components,

$$\dot{\epsilon}_{ij} = \dot{\epsilon}_{ij}^e + \dot{\epsilon}_{ij}^t + \dot{\epsilon}_{ij}^{in} \quad (1)$$

The elastic and thermal rates are found from

$$\dot{\epsilon}_{ij}^e = M_{ijkl}^e(\theta) \dot{\sigma}_{kl} \quad (2)$$

$$\dot{\epsilon}_{ij}^t = [(dM_{ijkl}^e(\theta)/d\theta) \sigma_{kl} + \delta_{ij} \beta(\theta)] \dot{\theta} \quad (3)$$

where  $\theta$  is current temperature,  $M_{ijkl}^e(\theta)$  is the elastic compliance,  $\delta_{ij}$  is the Kronecker tensor and  $\beta(\theta)$  is linear thermal expansion coefficient; (3) follows from (A-1) in Appendix.

The inelastic strain is found as a function of the overstress measured from an equilibrium yield surface which contains all stress states that can be reached from the current state by purely elastic deformation [11, 12]. The equilibrium surface is given by

$$g = \frac{3}{2} (s_{ij}^* - a_{ij}) (s_{ij}^* - a_{ij}) - (Y + Q)^2 = 0 \quad (4)$$

where  $s_{ij}^*$  is the deviatoric equilibrium stress tensor,  $a_{ij}$  denotes the center of the yield surface,  $Y = Y(\theta)$  is the initial yield stress in tension, independent of the loading rate, and  $Q = Q(\theta)$  is an isotropic hardening function.

For a given stress state  $s_{ij}$  outside the surface (4), there exists an equilibrium stress  $s_{ij}^*$  which satisfies (4) such that the stress points  $s_{ij}$  and  $s_{ij}^*$ , and the center of the equilibrium surface  $a_{ij}$  are collinear;

$$s_{ij}^* = \left[ \frac{2(Y + Q)^2}{3(s_{k\ell} - a_{k\ell})(s_{k\ell} - a_{k\ell})} \right]^{\frac{1}{2}} (s_{ij} - a_{ij}) + a_{ij}. \quad (5)$$

The effective overstress  $R$  is a measure of the distance between the actual stress point  $s_{ij}$  and the equilibrium stress point  $s_{ij}^*$ . It vanishes if the stress point lies on, or falls inside the yield surface. In particular,

$$\begin{aligned} R &= \left[ \frac{3}{2} (s_{ij} - s_{ij}^*)(s_{ij} - s_{ij}^*) \right]^{\frac{1}{2}} && \text{if } g(s_{ij} - a_{ij}) > 0, \\ R &= 0 && \text{if } g(s_{ij} - a_{ij}) \leq 0. \end{aligned} \quad (6)$$

The inelastic strain rate is then written as

$$\dot{\epsilon}_{ij}^{\text{in}} = \sqrt{(3/2)} k(\theta) R^{p(\theta)} n_{ij}, \quad (7)$$

where the functions  $k(\theta)$  and  $p(\theta)$  are material parameters and  $n_{ij}$  is a unit normal to the yield surface (4) at the current equilibrium stress point. From (4) one finds this as

$$n_{ij} = \frac{(s_{ij}^* - a_{ij})}{[(s_{k\ell}^* - a_{k\ell})(s_{k\ell}^* - a_{k\ell})]^{\frac{1}{2}}} = \sqrt{(3/2)} \frac{(s_{ij}^* - a_{ij})}{(Y + Q)}. \quad (8)$$

The evolution equation for  $Q$  which includes the effect of inelastic deformation and thermal recovery on the yield stress is given as

$$\dot{Q} = q(\theta) [Q_a(\theta) - Q] \dot{\bar{\epsilon}}^{in} - b_r(\theta) |Q - Q_r(\theta)|^{(n_r(\theta)-1)} [Q - Q_r(\theta)] . \quad (9)$$

The functions  $q(\theta)$ ,  $Q_a(\theta)$ ,  $b_r(\theta)$ ,  $Q_r(\theta)$ , and  $n_r(\theta)$  are material parameters, total ( $Q_r = 0$ ) or partial ( $Q_r \neq 0$ ) thermal recovery is represented by the second term in (9), and  $\dot{\bar{\epsilon}}^{in}$  is the effective inelastic strain rate;

$$\dot{\bar{\epsilon}}^{in} = \left[ \frac{2}{3} \dot{\epsilon}_{ij}^{in} \dot{\epsilon}_{ij}^{in} \right]^{\frac{1}{2}} = k(\theta) R^{p(\theta)} ; \quad \dot{\epsilon}_{kk}^{in} = 0 . \quad (10)$$

In analogy to (9), and permitting complete thermal recovery of kinematic hardening, the evolution equation for the center  $a_{ij}$  of the yield surface can be written as

$$\dot{a}_{ij} = \dot{\mu} \nu_{ij} - v_r(\theta) \bar{a}^{(w_r(\theta)-1)} a_{ij} , \quad \bar{a} = (a_{k\ell} a_{k\ell})^{\frac{1}{2}} , \quad (11)$$

where  $v_r(\theta)$  and  $w_r(\theta)$  are material parameters. The unit tensor  $\nu_{ij}$  defines the direction of translation of the yield surface in the deviatoric stress space, and can be specified according to the hardening rules applied in rate-independent plasticity theories. If the Phillips hardening rule is selected, then

$$\nu_{ij} = \dot{s}_{ij} / (\dot{s}_{k\ell} \dot{s}_{k\ell})^{\frac{1}{2}} \quad \text{if } \dot{s}_{ij} \neq 0 , \quad (12)$$

$$\nu_{ij} = n_{ij} \quad \text{if } \dot{s}_{ij} = 0 . \quad (13)$$

The factor  $\dot{\mu}$  in (11) is found from Prager's consistency condition  $\dot{g} = 0$ , with translation of the yield surface specified by the first term in (11). The result is

$$\dot{\mu} = \sqrt{(2/3)} k(\theta) R^{p(\theta)} [H(\theta) - q(\theta)[Q_a(\theta) - Q]] / n_{k\ell} \nu_{k\ell} . \quad (14)$$

A variant of the two-surface plasticity theory by Dafalias and Popov [13] is used to describe evolution of the instantaneous tangent modulus  $H$ :

$$H(\theta) = H_o(\theta) + h(\theta) [\delta / (\delta_o - \delta)]^{m(\theta)} , \quad (15)$$

$$\delta = \left[ \frac{3}{2} (\bar{s}_{ij} - s_{ij}^*)(\bar{s}_{ij} - s_{ij}^*) \right]^{\frac{1}{2}} , \quad (16)$$

where  $\delta$  is the distance between the stress point  $s_{ij}^*$  on the equilibrium surface and a point  $\bar{s}_{ij}$  on the bounding surface with normal equals  $n_{ij}$ , and  $\delta_0$  is the value of  $\delta$  at the onset of inelastic deformation. When the equilibrium stress point lies on the bounding surface, the plastic tangent modulus  $H(\theta)$  assumes the asymptotic value  $H_0(\theta)$ , which together with the parameters  $h(\theta)$  and  $m(\theta)$  need to be determined experimentally. In analogy with the equilibrium yield surface, thermal recovery of isotropic as well as kinematic hardening of the bounding surface can be included in the model. This is omitted here for brevity. We only mention that the recovery terms for isotropic and kinematic hardening of the bounding surface assume a form similar to those suggested above for the yield surface, but with new material parameters which we denote by script letter. For example, the Mises form of the bounding surface is written as

$$\mathcal{J} = \frac{3}{2} (s_{ij} - a_{ij}) (s_{ij} - a_{ij}) - (\mathcal{Y} + \mathcal{Z})^2 = 0, \quad (17)$$

where  $a_{ij}$  is the center of the bounding surface in the deviatoric stress space,  $\mathcal{Y} = \mathcal{Y}(\theta)$  is the bounding stress given by the intersection of the asymptotic part of the uniaxial stress-plastic strain curve and the stress axis, and  $\mathcal{Z} = \mathcal{Z}(\theta)$  is an isotropic hardening function.

In the Sigma/Timetal 21S system, the fiber was regarded as elastic and the matrix as thermo-viscoplastic. Elastic moduli of the Sigma fiber were assumed to be the same as those of the SCS6 fiber, and the material parameters for the Timetal 21S were derived, in part, from experiments performed at NASA Langley Research Center [14, 15]. Isotropic hardening of the equilibrium (4) and bounding (17) surfaces was neglected; thermal recovery in (9) and (11) was minor. The material parameters remaining after reductions appear in Tables 5 and 6.

## 3.2 Micromechanical Models of Composite Laminates

### 3.2.1 Model selection

Among the available approaches to modeling of inelastic composite materials, we use here the transformation field analysis (TFA) of the inelastic lamina [16] in conjunction with the laminated plate theory for symmetric laminates subjected to uniform in-plane overall stresses, out-of-plane normal stress, and changes in temperature. When used with a selected micromechanical model, the TFA method provides piecewise uniform approximations of the phase stress and strain fields that are then utilized in finding the overall instantaneous stiffness, compliance, and the thermal stress and strain tensors of the plies and laminate. The governing equations of the TFA method are described in some detail below. These equations were incorporated in a finite element procedure [17], as summarized in the sequel, and implemented in the VISCOPAC program [18] for a class of averaging micromechanical models. Specifically, the vanishing fiber diameter [19, 20], the self-consistent [21], and the Mori-Tanaka [22, 23] models are included. Work in progress uses the Periodic Hexagonal Array (PHA) model [24, 25] that provides piecewise uniform approximations of the local fields in the matrix, fiber, and at their interfaces, and can thus follow more closely their evolution along the local loading path.

### 3.2.2 Transformation field analysis

A representative volume of a fibrous composite ply is considered, under uniform overall stress or strain, and a uniform change in temperature. The goal is to estimate the stress and (small) strain averages caused in the elastic fiber and inelastic matrix by the applied loads. In the transformation field analysis, these averages are found by superposition of two load systems, one consisting of the applied mechanical loads, in the form of uniform overall stress or strain, and one associated with internal eigenstrains that include thermal strains, any inelastic strains, and also equivalent eigenstrains designed to simulate damage development, e. g., by fiber sliding and debonding. This identification of

thermal, inelastic and damage-induced deformations with eigenstrains, implies that both load systems act on an elastic, undamaged composite. Of course, except for the thermal strains, the eigenstrain load system is not known *a priori*, it is evaluated incrementally from certain governing equations provided by the transformation analysis method.

The procedure has been described in several references, for example in [16] and [26]. An exposition of these results, that is particularly easy to implement, uses symbolic notation where boldface lower case letters represent symmetric second-order tensors written as (6x1) matrices, and boldface capital letters denote symmetric fourth-order tensors written as (6x6) matrices. Connections with the notation used in Section 2 are easily established. For example, the strain tensor  $\epsilon_{ij}$ , with the symmetry  $\epsilon_{ij} = \epsilon_{ji}$ , is written as  $\epsilon = \{\epsilon_{11} \ \epsilon_{22} \ \epsilon_{33} \ 2\epsilon_{23} \ 2\epsilon_{31} \ 2\epsilon_{12}\}^T$ ; fourth-order tensors having at least the symmetries  $A_{ijkl} = A_{jikl} = A_{ijlk}$  are reduced to (6x6) matrices  $A$ , such that  $AA^{-1} = A^{-1}A = I$ , the identity matrix.

The selected representative volume  $V$  of a composite ply is assumed to contain many fibers and be loaded by an overall stress  $\sigma$  or strain  $\epsilon$ , both macroscopically uniform. A certain subdivision of  $V$  into subvolumes  $V_r$ ,  $V_s$  is chosen ( $r, s = 1, 2, \dots N$ ). In what follows,  $N = 2$ , and  $V_r$ ,  $V_s$  will be either fiber or matrix volumes  $V_f$  or  $V_m$ , ( $r, s = f, m$ ).

The elastic constitutive relations for the fiber and matrix phases with initial strains or eigenstrains  $\mu_r$  and eigenstresses  $\lambda_r = -L_r \mu_r$  are written as

$$\sigma_r = L_r \epsilon_r + \lambda_r \qquad \epsilon_r = M_r \sigma_r + \mu_r. \qquad (18)$$

The  $L_r$  and  $M_r = L_r^{-1}$  are phase elastic stiffness and compliance matrices, discussed in the Appendix. The  $\mu_r$  is the total eigenstrain that would remain in the phase volume  $V_r$  after complete local unloading to zero stress, whereas the eigenstress  $\lambda_r$  is seen to represent the total stress caused in a fully constrained volume  $V_r$  by the eigenstrain  $\mu_r$ . It then follows that  $\lambda_r = -L_r \mu_r$ . Since the  $L_r$  and  $M_r$  depend only on elastic moduli, assumed to be constant at a given temperature, (18) can be readily converted into a rate form,

$$\dot{\sigma}_r = L_r \dot{\epsilon}_r + \dot{\lambda}_r \quad \dot{\epsilon}_r = M_r \dot{\sigma}_r + \dot{\mu}_r \quad (19)$$

With reference to (1), (3) and (7), the eigenstrain rate  $\dot{\mu}_r$  that represents the thermal and inelastic deformation, may be written as

$$\dot{\epsilon} = \dot{\epsilon}^e + \dot{\mu} \quad \dot{\mu} = \dot{\epsilon}^t + \dot{\epsilon}^{in} \quad (20)$$

The superposition of the two load states employed in the transformation field method provides the following form of the local fields,

$$\dot{\epsilon}_r = A_r \dot{\epsilon} + \sum_s D_{rs} \dot{\mu}_s, \quad r, s = f, m \quad (21)$$

$$\dot{\sigma}_r = B_r \dot{\sigma} + \sum_s F_{rs} \dot{\lambda}_s.$$

The  $\dot{\epsilon}$  and  $\dot{\sigma}$  denote the uniform overall strain and stress rates applied to the representative volume, and  $A_r$  and  $B_r$  are mechanical strain and stress concentration factor matrices. The  $D_{rs}$  and  $F_{rs}$  are transformation concentration factors, which evaluate the contribution to the local field in  $V_r$ , caused by a uniform transformation field of unit magnitude present in  $V_s$ . Both the mechanical and transformation concentration factors depend only on elastic moduli and phase geometry, and thus remain constant, except under large changes in geometry or temperature which affect the elastic moduli. In the latter case, the concentration factors are recalculated to reflect such changes, c. f., §3.2.3 below.

Of course, (19) can be applied to any number of subdivisions of the representative volume. However, we limit our attention to phase average fields in two-phase solids. Then, the concentration factors can be found in a very simple form [16, 27, 28], involving only overall elastic moduli  $L$ , or compliances  $M$ , and the known phase elastic moduli and volume fractions,

$$A_r = (L_r - L_s)^{-1} (L - L_s) / c_r ,$$

$$r, s = f, m \quad (22)$$

$$B_r = (M_r - M_s)^{-1} (M - M_s) / c_r ,$$

$$D_{rf} = (I - A_r) (L_f - L_m)^{-1} L_f \quad D_{rm} = - (I - A_r) (L_f - L_m)^{-1} L_m , \quad (23)$$

$$F_{rf} = (I - B_r) (M_f - M_m)^{-1} M_f \quad F_{rm} = - (I - B_r) (M_f - M_m)^{-1} M_m .$$

The overall elastic stiffness can be either measured, bracketed by the Hashin–Rosen or other exact bounds, or estimated by several approximate methods; in this work we use the Mori–Tanaka estimates discussed in the Appendix.

The governing equations for the unknown local eigenstrain rates can be now completed by first substituting for the concentration factors from (22) and (23), and for the eigenstrains from (20). In particular, the  $\dot{\mu}$  in (20) is obtained from (3) and (7), converted into an eigenstress using the relation  $\dot{\lambda} = -L \dot{\mu}$  that follows from (18) or (19), and substituted into (21<sub>2</sub>). Therefore, the eigenstrain rates are replaced by expressions involving increments of temperature and of local stress rates, and (21<sub>2</sub>) is converted into a system of differential equations for evaluation of the local stresses. In a similar way, (21<sub>1</sub>) can be converted into a system of equations for the local strains. Solution techniques for either system are readily available [26].

Once the averages of the local stress or strain rates are known at a particular point of the loading path, the inelastic strains and other local eigenstrains can be found from the phase constitutive relations. Overall averages of the total local stress and strain field rates follow from the connections

$$\dot{\sigma} = \sum_r c_r \dot{\sigma}_r \quad \dot{\epsilon} = \sum_r c_r \dot{\epsilon}_r , \quad (24)$$

while the overall transformation fields are found from,

$$\dot{\lambda} = \sum_r c_r A_r^T \dot{\lambda}_r \quad \dot{\mu} = \sum_r c_r B_r^T \dot{\mu}_r \quad (25)$$

The overall constitutive relations of the ply are then written in a form similar to (18) and (19),

$$\sigma = L \epsilon^0 + \lambda \quad \epsilon = M \sigma^0 + \mu \quad (26)$$

$$\dot{\sigma} = L \dot{\epsilon}^0 + \dot{\lambda} \quad \dot{\epsilon} = M \dot{\sigma}^0 + \dot{\mu},$$

where  $\dot{\sigma}^0$  or  $\dot{\epsilon}^0$  are the overall applied rates, the overall elastic stiffness  $L$  and compliance  $M$  are obtained as in (22), from experimental measurements, bounds, or estimates.

The transformation analysis procedure can be used with any physically acceptable phase constitutive relations and micromechanical technique for elastic composites, including the unit-cell models [24, 25], and also in laminate analysis. The only difference resulting from the various model selection is in the number of subdivisions of the representative volume ( $r = 1, 2, \dots, N$ ), and in evaluation of the concentration factor tensors for each subvolume  $V_r$ . Of course, if more local volumes are used, the piecewise uniform approximation of the local fields found from (21) should be more responsive to the inelastic constitutive relations of the phases and thus more accurate. However, for given constitutive relations, the structure of the governing equations and the solution procedures are identical for all models.

This approach differs from that where the inclusion problem is solved for an elastic matrix whose compliance is identified with the instantaneous viscoplastic compliance derived from the average matrix stress history [29]. The latter calls for repetitive solutions of the inelastic inclusion problem in a generally anisotropic matrix, not needed in our approach; it also may violate (25). On the other hand, if the concentration factors in (21)

are found using a finite element analysis of a subdivided unit cell model, such as the PHA model [24, 25], then the solution of (21) coincides with an inelastic finite element solution [26].

### 3.2.3 Modeling of interface damage

Fiber debonding and/or sliding are usually the initial damage states in fibrous composite plies subjected to off-axis loading of sufficient magnitude. The interface strengths are typically quite small. For example, Clyne and Withers [30] give interface shear strength magnitudes in the range of 50–100 MPa; normal strength values do not appear to be available, but are expected to be lower. Cyclic shear sliding tends to reduce the number of adhering asperities and thus the apparent interface shear strength. Therefore, transverse tension and shear, and longitudinal shear stresses in plies can initiate interface damage. Of course, processing and heat treatment may affect the actual magnitudes; for example, growth of brittle interfacial reaction layers may promote early debonding and matrix crack growth, whereas treatments that promote favorable residual stress states may increase the apparent strength.

However, as long as some adhering asperities are left at the interface after debonding, they should provide for shear stress transfer that may prevent fiber pullout. For example, the average surface shear ( $\tau$ ) and normal ( $\sigma$ ) stresses in the fiber are connected by the force equilibrium relation  $2\pi L\tau = \pi r^2 \sigma$  over a length  $L$  of a fiber with radius  $r$ , i. e.,  $\sigma/\tau = 2L/r$ . If  $L = 25$  mm is selected as a transfer length, and the radius of the Sigma fiber  $r = 50$   $\mu\text{m}$ , then one finds that  $\sigma = 1000 \tau$ . This suggests that large normal stress may be transferred into a fiber even if the interface shear stress is very low. Therefore, apart from fiber breaks, fiber pullout is not expected, and the integrity of the fibrous plies in the axial direction should not be impaired in the presence of fiber sliding.

Guided by results of our related studies, which suggest that large diameter fibers release a substantial amount of energy during debonding and thus experience nearly total,

instantaneous separation, we represented the interface failure under normal or shear stresses by reducing certain fiber stress components to zero through abrupt changes in the fiber elastic moduli. In this part, the fiber was regarded as transversely isotropic, with moduli equal to isotropic material magnitudes (see the Appendix). If the interface normal stress component reached the selected strength magnitude of 50 MPa, then the transverse shear and Young's moduli  $G_T^f$  and  $E_T^f$  were reduced to zero. Similarly, if the interface longitudinal shear stress exceeded the selected 80 MPa shear strength, the longitudinal shear modulus  $G_L^f$  was reduced to zero. This approach has been implemented in the transformation analysis method. The ply elastic moduli in (22) and (23) have been found by the Mori-Tanaka method. After fiber moduli reductions, the ply stiffnesses and compliances, as well as the concentration factors, were reevaluated and introduced in the governing equations (21). More advanced stages of damage, such as matrix cracking and fiber breaks, were not considered in the present analysis.

#### 3.2.4 Finite element scheme

We now consider the finite element solution for an assemblage of  $M$  elements interconnected at  $N$  nodal points subjected to concentrated loads  $p_i(t)$ ,  $i = 1, 2, \dots, N$ , and uniform temperature variation  $\theta_m(t)$ ,  $m = 1, 2, \dots, M$ . Incorporating the transformation field analysis described above in the initial strain finite element formulation given by Zienkiewicz and Corneau [31], Bahei-El-Din [17] developed a finite element scheme for multiphase materials and structures. For two-phase materials with the rate-dependent behavior described in Section 2, the algorithm for computing the time-rate of the nodal displacements,  $\dot{\mathbf{a}}_i$ ,  $i = 1, 2, \dots, N$ , element overall strains and stresses,  $\dot{\epsilon}_m$ ,  $\dot{\sigma}_m$ ,  $m = 1, 2, \dots, M$ , and phase strains and stresses,  $\dot{\epsilon}_r$ ,  $\dot{\sigma}_r$ ,  $r = 1, 2$ , is outlined for infinitesimal strains as follows [17]:

1. Compute the overall stiffness matrix  $\mathbf{K}$  at current temperature:

$$\mathbf{K}_{ij} = \sum_{m=1}^M \int_{V_m} [\Lambda_i^m]^T \mathbf{L}_m(\theta_m) \Lambda_j^m dV_m$$

where the coefficient matrix  $\Lambda_m$  defines the element average strains,  $\dot{\epsilon}_m$ , in terms of the nodal displacements,  $\dot{\mathbf{a}}_m$ ;  $\dot{\epsilon}_m = \Lambda_m \dot{\mathbf{a}}_m$ . The form of  $\Lambda_m$  depends on the shape functions selected to represent the displacement field in the elements. If the strains in element  $m$  is required to be uniform, as for example in idealization of two-phase materials by averaging models, then the displacement shape functions must be linear in the coordinates  $x_j$ ,  $j = 1, 2, 3$ , and matrix  $\Lambda_m$  is constant.

2. For elements  $m = 1, 2, \dots, M$ :

- a) From the constitutive law presented in eqs. (1)–(3), and (7), compute the transformation strain rate at temperature  $\theta_m$  for phases  $r = 1, 2$  as the sum of viscoplastic and thermal components;

$$\dot{\mu}_{ij}^{(rm)} = \left[ \alpha_{ij}^{(rm)} + \left( \partial M_{ijk1}^{(rm)} / \partial \theta \right) \sigma_{kl}^{(rm)} \right] \dot{\theta}_m + \left[ k(\theta) R^{p(\theta)} \right]_{rm} \nu_{ij}^{(rm)},$$

$$\dot{\mu}_{rm} = \{ \mu_{11} \ \mu_{22} \ \mu_{33} \ 2\mu_{23} \ 2\mu_{31} \ 2\mu_{12} \}_{rm}.$$

- b) Compute the inelastic strain rate at time  $t$  for element  $m$ ;

$$\dot{\mu}_m = c_1 \mathbf{B}_1^T(\theta_m) \dot{\mu}_{1m} + c_2 \mathbf{B}_2^T(\theta_m) \dot{\mu}_{2m}.$$

- c) Compute the contribution of element  $m$  to nodal load rates;

$$\dot{\mathbf{f}}_i^m = - \int_{V_m} [\Lambda_i^m]^T \mathbf{L}_m(\theta_m) \dot{\mu}_m dV_m.$$

where  $\mathbf{L}_m$  is the overall stiffness matrix of element  $m$  evaluated at the current temperature of the element.

3. Assemble current rates of nodal loads:

$$\dot{\mathbf{f}}_i = \dot{\mathbf{p}}_i - \sum_{m=1}^M \dot{\mathbf{f}}_i^m.$$

4. Compute rates of nodal deflections at time  $t$ :

$$\dot{\mathbf{a}} = \mathbf{K}^{-1} \dot{\mathbf{f}}$$

5. For elements  $m = 1, 2, \dots, M$ ;

a) Compute overall strain rate;  $\dot{\epsilon}_m = \Lambda_m \dot{\mathbf{a}}_m$ ,

b) Compute overall stress rate;  $\dot{\sigma}_m = \mathbf{L}_m(\theta_m) (\dot{\epsilon}_m - \dot{\mu}_m)$ ,

c) For phase  $r = 1, 2$ , of element  $m$ ;

– Compute local strain rate;  $\dot{\epsilon}_r = \mathbf{A}_r(\theta_m) \dot{\epsilon} + \mathbf{D}_{r1}(\theta_m) \dot{\mu}_1 + \mathbf{D}_{r2}(\theta_m) \dot{\mu}_2$ ,

– Compute local stress rate;  $\dot{\sigma}_r = \mathbf{L}_r(\theta_m) (\dot{\epsilon}_r - \dot{\mu}_r)$ .

The above rate equations are assembled into a system of first order differential equations (ODE) of the form

$$\dot{\mathbf{y}}_j(t) = \mathbf{g}_j(t, y_1, y_2, \dots, y_R). \quad (27)$$

The unknown functions  $\mathbf{g}_j$ ,  $j = 1, 2, \dots, R$ , are identified with the nodal displacements  $\mathbf{a}_i$ ,  $i = 1, 2, \dots, N$ , the element stress  $\sigma_m$  and strain  $\epsilon_m$ ,  $m = 1, 2, \dots, M$ , the phase stress  $\sigma_r$  and strain  $\epsilon_r$ ,  $r = 1, 2$ , and any internal variables required to define the eigenstrain rate  $\dot{\mu}_r$ , e.g. the scalar function  $R$  as in eq. (6). Assuming elastic response of the phases in the initial state, the rate equations can be integrated for a specified time period using an ODE solver for stiff differential equations which are normally encountered in viscoplastic response modeled with the power law adopted in eq. (7). Implementation of the finite element algorithm in the VISCOPAC program [18] used the Gear method for stiff equations [32, 33].

### 3.3 Interpretation of Isothermal Static and Fatigue Data of Sigma/Timetal 21S Laminates

The fatigue experiments described in Section 2 are simulated using the analytical/numerical approach described above. The computations were performed for several specimens of the Sigma/Timetal 21S,  $(0)_4$ ,  $(0/90)_s$ , and  $(0/\pm 45/90)_s$  laminates tested in the experimental program. Fabrication by hot isostatic pressing, which has a significant effect on the overall response, was modeled first. Subsequent loading consisted of axial tension/tension load cycles at a specified amplitude and frequency, after a uniform change of temperature from 21°C to 650°C in 6 minutes. Assuming that the overall stress and strain were uniform in the gauge section the specimen, where the strain measurements were made, the response of the laminates under the applied load was determined from the classical laminated plate theory for in-plane loading, modeled with the finite element method.

A schematic of the finite element model for laminates is shown in Fig. 26 for the  $(0/\pm 45/90)_s$  layup. Each unidirectional ply is represented by one hexahedral element. The overall elastic moduli of the plies, and the phase mechanical and transformation concentration factors were derived from the Mori-Tanaka model of the fibrous microstructure. As described in Section 3.3, interface failure by fiber separation was assumed to take place when the maximum interface normal stress component reached a selected normal bond strength magnitude  $\sigma_b$ , and by fiber sliding when the maximum interface longitudinal shear stress exceeded a selected shear bond strength  $\tau_b$ . In analysis of the Sigma/Timetal 21S system,  $\sigma_b = 50$  MPa and  $\tau_b = 80$  MPa were assumed for the interface strength magnitudes against separation and sliding, respectively.

#### 3.3.1 Hot isostatic pressing

Fabrication of the Sigma/Timetal 21S laminates by hot isostatic pressing was conducted at 899°C (1650°F) and 103.5 MPa (15 ksi) hydrostatic pressure for 2 hours. In the analytical simulation, we assumed that the laminate is free of internal stresses at the

fabrication temperature where the matrix yield stress is very low, Table 6. Subsequent cooling to room temperature was completed in 3 minutes and followed by aging at 621°C (1150°F) for 8 hours. Figure 27 shows the temperature and load history applied during fabrication and aging. We note that the actual aging period of 8 hours, during which the titanium matrix remained elastic, has been reduced to 2 hours in Fig. 27.

The average residual stresses, referred to the local coordinate system  $\bar{x}_j$ ,  $j = 1, 2, 3$ , Fig. 26, caused by fabrication in the fiber and matrix of the  $(0)_4$  unidirectional laminate are shown in Table 7 after cooldown to room temperature and subsequent reheating to the test temperature (650°C). The fiber supports a compressive axial residual stress  $\sigma_{11}$ , which increases the apparent strength of the composite under subsequent axial tensile loading. The fiber also supports a compressive transverse stress  $\sigma_{22}$  after fabrication. A more detailed study of the local fields computed in a composite cylinder model of a unidirectional titanium matrix composite [34] indicated that the radial residual stress at the fiber interface was indeed compressive, and thus supportive of interface bonding. This suggests that tensile hoop stress is present in the matrix at the fiber interface. This may promote radial cracking in the matrix and open the way for environmental degradation of the fiber, particularly at high temperature. The magnitude of the residual stresses may be adjusted somewhat by varying the cooling rate and the magnitude of the HIP pressure [34, 35].

The local stresses caused in the plies of quasi-isotropic  $(0/90)_s$  and  $(0/\pm 45/90)_s$  laminates by the thermomechanical loads applied in the HIP process are expected to be independent of the fiber orientation [36, 37]. Table 8 shows the residual stresses found in a typical ply of these laminates and in the fiber and matrix phases after cooldown to room temperature and subsequent reheating to the test temperature (650°C). As in the unidirectional composite, the residual axial fiber stress  $\sigma_{11}$  is compressive and thus helps to reduce the tensile stress magnitude under subsequent tensile mechanical loading. However, a tensile residual stress  $\sigma_{22} = 15$  MPa is present in the fiber at 650°C, which may promote debonding under subsequent axial tension loading. Of course, under the selected value of

the interface normal bond strength  $\sigma_b = 50$  MPa, the fiber interface remains intact at the test temperature of 650°C.

The overall axial strains were measured experimentally at 650°C as 0.40, 0.46, and 0.45% in the  $(0)_4$ ,  $(0/90)_s$ , and  $(0/\pm 45/90)_s$  laminates, respectively, Table 1. They compare well with the computed strains of 0.377% for the  $(0)_4$  unidirectional composite, and 0.424% for each of the quasi-isotropic  $(0/90)_s$  and  $(0/\pm 45/90)_s$  laminates.

### 3.3.2 Static loading

In the actual fatigue experiments, Section 2.4, mechanical loading to the mean stress was applied in one minutes and kept constant for one minute before application of the load cycles. Consequently, the mean stress load rates varied according to the stress range selected for the various layups. In the numerical simulation of this load step, fiber debonding and sliding took place in the off-axis plies under overall axial tensile stress magnitudes lower than the mean stress, with interface normal strength  $\sigma_b = 50$  MPa and shear strength  $\tau_b = 80$  MPa. Figures 28 and 29 show variation of the transverse normal stress and longitudinal shear stress in the fully bonded fiber of the off-axis plies of the Sigma/Timetal 21S  $(0/90)_s$  and  $(0/\pm 45/90)_s$  laminates as a function of the applied tensile axial stress at the two applied loading rates. The offset stress found at zero overall load represents the residual stress after fabrication, Table 8. At the selected  $\sigma_b = 50$  MPa, fiber debonding initiates under an overall axial stress of about 25 MPa. Similarly, initiation of interface sliding in the 45° plies at  $\tau_b = 80$  MPa takes place while the overall axial stress is less than 100 MPa. However, at these overall load magnitudes, the rate of loading has no significant effect on the local stresses.

To illustrate the extent of interface damage which is likely to take place in the Sigma/Timetal 21S specimens during the fatigue tests, we computed the local stresses in a  $(0/\pm 45/90)_s$  laminate loaded by an overall axial stress at 2.75 MPa/s. This rate corresponds to loading to the mean stress of the 300–30 MPa stress range in one minute.

Table 9 shows the computed local stresses in the plies and in the fiber and matrix phases at the onset of interface failure in the individual plies, together with the corresponding overall stress magnitudes. Interface failure initiates in the 90-degree fiber when the transverse tensile stress reaches the selected interface strength of 50 MPa, at an overall axial stress of only 18 MPa. Subsequent loading to 26 MPa caused fiber debonding in the  $\pm 45$ -degree plies, followed by debonding of the 0-degree fiber at 59 MPa. Finally, the magnitude of longitudinal shear stress in the fiber of the  $\pm 45$ -degree plies reached the selected shear strength of 80 MPa at overall axial stress of 65 MPa.

Under subsequent loading, the debonded fibers in the off-axis plies as well as the 0-degree ply fibers, support only axial normal stresses. Consequently, the stiffness of the off-axis plies in the loading direction is reduced substantially, and the axial stress concentration factor, given by the ratio of the local to overall axial stress increments, increases in the 0-degree layer. For example, as seen from Table 9, this ratio increased from 2.8 at the overall stress of 18 MPa, where all fibers are still perfectly bonded, to 4.2 at 65 MPa, where the fiber were debonded in all plies. The corresponding ratios for the fiber stress in the 0-degree ply are 5.4 and 9.4, which indicate a substantial increase in the fiber stress in the axial direction due to interface damage of the off-axis plies. At 165 MPa, the overall axial strain was computed at 0.72%, slightly above the measured value of 0.64%.

### 3.3.3 Isothermal load cycles

*The Local stresses* computed for the Sigma/Timetal 21S (0/ $\pm 45$ /90)<sub>s</sub> laminate subjected to axial tension/tension load cycles at 650°C, with maximum stress  $S_{\max} = 300$  MPa,  $S_{\min}/S_{\max} = 0.1$ , and a period of 1000s/cycle are summarized in Figs. 30–39. Figure 30 shows the load history during the eleven cycles sustained by the specimen in the actual experiments, Section 2.4. Figure 3 shows the average stresses generated in the 0° ply, and Figs. 32 and 33 provide the local stress averages in the fiber and matrix. The ply and local stresses in the  $\pm 45$ -degree plies are shown in Figs. 34–36,

and the stresses in the 90-degree ply are presented in Figs. 37–39. The ratcheting behavior found in the stress histories is caused by the viscoplastic response of the titanium matrix, modeled by the constitutive equations given in Section 3.1. In general, the matrix stresses are relaxed and the fiber axial stress in all plies is enhanced under the applied tension/tension load cycles. Under slow load cycles applied at 0.001 Hz, a nearly steady state response is reached after only few cycles.

The cyclic stress maxima and minima computed in the first cycle and in the failure cycle 11 are shown in Table 10 under the cyclic loading conditions indicated in Fig. 30 for the slow fatigue cycles at 0.001 Hz (Figs. 31–39). The stresses computed for a fast cycle at 0.1 Hz under the same loading conditions are also indicated. Another test sample subjected to the same load amplitudes, but at 0.1 Hz, survived 207 cycles, Table 2. In this case, the computed local stresses reached a steady state after 90 cycles. The local stresses were then extrapolated to the failure cycle using a logarithmic function of the cycle number;  $\sigma = A + B \log N$ , where  $N$  is the cycle number, and  $A$  and  $B$  are fitting parameters to be computed from the data at the steady state. For example, using the computed data at cycles 91, 92, and 93, at which the local stresses stabilize, the average axial stress  $\sigma_{11}$  in the  $0^\circ$  ply is extrapolated to the failure cycle 207 using the above logarithmic equation with  $A = 735.7$ , and  $B = 63.2$ .

The rate effect on the local stresses is evident in the results given in Table 10 for the first cycle. For example, the matrix axial normal stress  $\sigma_{11} = 119$  MPa when computed in the  $0^\circ$ -degree ply at  $S_{\max} = 300$  MPa under 0.001 Hz. At 0.1 Hz and  $S_{\max} = 300$  MPa,  $\sigma_{11}^m = 206$  MPa. In contrast, the axial stress in the  $0^\circ$  fiber is elevated at the slow loading rate. The maximum fiber stress found at failure, however, appears to be independent of the loading frequency. Specifically, the axial stress computed in the  $0^\circ$  fiber at failure is 1981 MPa under 0.001 Hz, and 1988 MPa under 0.1 Hz. This suggests that failure of the laminate is controlled by the strength of the fiber in the  $0^\circ$  ply, and that the fatigue life is dependent on the rate at which the fiber tensile strength is reached.

Both the average transverse and longitudinal shear stresses in the  $0^\circ$  ply matrix are low in plies with debonded fibers, and decrease with cycling. Also, the maximum axial stress in the  $\pm 45^\circ$  fiber  $\sigma_{11} = 687$  MPa, and remains low in the  $\pm 45^\circ$  fiber.

A *failure Criterion* may be postulated for laminates subjected to cyclic axial loading based on the preceding discussion of local stresses. In particular, a one-parameter criterion based on the tensile strength, or ultimate strain of the  $0^\circ$  ply, or its fiber may be representative of the observed fatigue behavior. The overall axial strains measured at failure for the Sigma/Timetal 21S laminates tested in the experimental program under tension/tension load cycles applied at  $650^\circ\text{C}$  are shown in Table 2.

Although the measured fatigue life of the tested laminates varied with the load frequency, Fig. 23, the overall strains measured at failure were not frequency-dependent. Moreover, the measured failure strains appear to be independent of both the layup and the stress amplitude. This is shown in Figs. 40 and 41 where the overall strain at failure is plotted as a function of the number of cycles. The measured strains, represented by the closed symbols, fall within a narrow range in the order of  $1.0 \pm 0.1$  % for both the fast and the slow load cycles.

Predictions of the overall strains are indicated by the open symbols in Figs. 40 and 41. The computed strains are consistent with the measured values and fall in the experimental strain range. This suggests that the fatigue life of composite laminates can be estimated based on the computed total overall strain. For a ductile matrix with rate-dependent behavior, such as the titanium matrix examined here, the number of cycles for reaching the critical strain magnitude is a function of the load frequency.

## 6. CONCLUSIONS

The experimental results show that at 650°C, viscoplastic deformation of the Timetal 21S matrix can be detected even at relatively low applied stresses. At both 650°C and 21°C, reduction of unloading elastic moduli of the  $(0/90)_s$  and  $(0/\pm 45/90)_s$  laminates was observed after either cyclic or static loading to relatively low tensile stresses. This indicates onset of damage. In static tests at room temperature, interface decohesion and fiber sliding appear to be the principal damage modes. In fatigue tests at 650°C, matrix cracking is also present. The cyclic loading rate has no effect on endurance of the  $(0/90)_s$  and  $(0/\pm 45/90)_s$  laminates loaded by constant amplitude tension at 650°C. In the  $(0)_4$  laminate, higher endurance limits were observed at 0.1Hz than at 0.001 Hz. However, regardless of rate and layup, the total strain at failure under both static and cyclic loading at 650°C, was measured at  $1\pm 0.1\%$ . In room temperature static tests, the failure strain was measured at 0.5–0.6%,

Micromechanical modeling of viscoplastic composite laminates with the transformation field analysis (TFA) and the finite element method has been described and applied to Sigma/Timetal 21S laminates using the Mori–Tanaka model for unidirectional composites. The computed results provide a qualitative evaluation of the local stresses under fabrication and subsequent loading, and point to possible causes of fatigue failure in  $(0/90)_s$  and  $(0/\pm 45/90)_s$  laminates.

Under constant temperature, the fiber stresses in the  $0^\circ$  plies increase with the number of cycles, until a certain overloading situation is reached. The rate of change of the fiber stress with cycles is reflected by the ratcheting rate of the viscoplastic titanium matrix, particularly at high temperature, and is a function of the loading frequency. The axial stresses estimated in the  $0^\circ$  fiber under identical isothermal loading conditions, but different frequencies are equal. Substantial interface damage is expected to take place in

the fiber of the off-axis plies, but the matrix stresses are small and may not cause significant matrix cracking.

The fatigue data measured for the Sigma/Timetal 21S laminates under various stress amplitudes, and two frequencies which differ by two orders of magnitude, suggest a one-parameter failure criterion based on a  $1 \pm 0.1$  % ultimate strain of the  $0^\circ$  ply, or its fiber, at  $650^\circ\text{C}$ . This maximum measured strain is closely approximated by the strain computed at the failure cycle using the micromechanical TFA/FE modeling approach.

### ACKNOWLEDGEMENT

This work was supported by the Air Force Office of Scientific Research and was performed in cooperation with the NIC program at Wrights Patterson Laboratory. Drs. Walter Jones, Ted Nicholas, and Joseph Zuiker served as contract monitors and advisors.

## REFERENCES

1. T. Nicholas and S.M. Russ, 'Elevated temperature fatigue behavior of SCS-6/Ti-24Al-11Nb,' *Materials Science and Engineering A153*, 514-519 (1992).
2. W.D. Pollock and W.S. Johnson, *Characterization of unnotched SCS-6/Ti-15-3 metal matrix composite at 650°C*, NASP TM 102699, 1990.
3. S.M. Russ, T. Nicholas, M. Bates and S. Mall, 'Thermomechanical fatigue of SCS-6/Ti-24Al-11NB metal matrix composites,' in *Failure Mechanisms in High Temperature Composite Materials*, G.K. Haritos, G. Newaz and S. Mall, eds., AD-Vol. 22/AMD-Vol. 122, American Society for Mechanical Engineers, New York, 1991, pp. 37-43.
4. R.W. Neu and T. Nicholas, 'Thermomechanical fatigue of SCS-6/Timetal 21S under out-of-phase loading,' in *Thermomechanical Behavior of Advanced Structural Materials*, W.F. Jones, ed., AD-Vol. 34/AMD-Vol. 173, American Society for Mechanical Engineers, New York, 1993, pp. 97-111.
5. R.W. Neu and T. Nicholas, 'Effect of laminate orientation on the thermomechanical fatigue behavior of a titanium matrix composite,' *J. Composites Tech. Res.* 16, 214-244 (1994).
6. T. Nicholas, J.L. Kroupa and R.W. Neu, 'Analysis of a [0/90] metal matrix composite under thermomechanical fatigue loading,' *Composites Engineering* 3, 675-689 (1993).
7. M.G. Castelli, *Thermomechanical fatigue damage/failure mechanisms in SCS-6/Timetal 21S [0/90]<sub>s</sub> composite*, NASA CR-191115, NASA Lewis Research Center, Cleveland, OH, 1993.

8. K.A. Hart and S. Mall, 'Response of a quasi-isotropic metal matrix composite under thermomechanical fatigue', in *Thermomechanical Behavior of Advanced Structural Materials*, W.F. Jones, ed., AD-Vol. 34/AMD-Vol. 173, American Society for Mechanical Engineers, New York, 1993, pp. 47-60.
9. R.R. Cervay,  $\sigma/\beta 21S$  Physical and mechanical property evaluation, NASP Report 1169, 1994.
10. W.S. Johnson, M. Mirdamadi and Y.A. Bahei-El-Din, 'Stress-strain analysis of a  $[0/90]_{2s}$  titanium matrix laminate subjected to a generic hypersonic flight profile', *J. Composites Tech. Res.* 15, 297-303 (1993).
11. Y.A. Bahei-El-Din, R.S. Shah and G.J. Dvorak, 'Numerical analysis of the rate-dependent behavior of high temperature fibrous composites,' in *Mechanics of Composites at Elevated and Cryogenic Temperatures*, S.N. Singhal, W.F. Jones, T. Cruse and C.T. Herakovich, eds., AMD-vol. 118, American Society of Mechanical Engineers, New York, 1991, pp. 67-78.
12. R.D. Shah, *Modeling and analysis of high temperature inelastic deformation in metal matrix composites*, Ph.D. Thesis, Rensselaer Polytechnic Institute, Troy, New York, 1991.
13. Y.F. Dafalias and E.P. Popov, 'Plastic internal variables formalism of cyclic plasticity,' *J. Appl. Mech.* 43, 645-651 (1976).
14. W.S. Johnson, M. Mirdamadi and Y.A. Bahei-El-Din, 'Stress-strain analysis of a  $[0/90]_{2s}$  titanium matrix laminate subjected to a generic hypersonic flight profile,' *J. Composites Tech. Res.* 15, 297-303 (1993).
15. W.S. Johnson and M. Mirdamadi, M., Private communication, 1993.
16. G.J. Dvorak, 'Transformation field analysis of inelastic composite materials,' *Proceedings of the Royal Society London A* 437, 311-327 (1992).
17. Y.A. Bahei-El-Din, 'Finite element analysis of viscoplastic composite materials and structures,' *Mechanics of Composite Materials and Structures*, in print.

18. Y.A. Bahei-El-Din, *VISCOPAC finite element program for viscoplastic analysis of composites, User's manual*, Structural Engineering Department, Cairo University, Giza, Egypt, 1993.
19. G.J. Dvorak and Y.A. Bahei-El-Din, 'Plasticity Analysis of Fibrous Composites,' *J. Appl. Mech.* **49**, 327-335 (1982).
20. Y.A. Bahei-El-Din, 'Plasticity Analysis of Fibrous Composite Laminates Under Thermomechanical Loads,' in *Thermal and Mechanical Behavior of Ceramic and Metal Matrix Composites*, ASTM STP 1080, J.M. Kennedy, H.H. Moeller and W.S. Johnson, eds., American Society for Testing and Materials, Philadelphia, 1990, pp. 20-39.
21. R. Hill, 'Theory of mechanical properties of fiber-strengthened materials-III, Self-consistent model,' *J. Mech. Phys. Solids* **13**, 189-198 (1965).
22. T. Mori and K. Tanaka, 'Average stress in matrix and average elastic energy of materials with misfitting inclusions,' *Acta Metall.* **21**, 571-574 (1973).
23. Y. Benveniste, 'A new approach to the application of Mori-Tanaka's theory in composite materials,' *Mech. Materials* **6**, 147-157 (1987).
24. G.J. Dvorak and J.L. Teply, 'Periodic hexagonal array models for plasticity analysis of composite materials,' in *Plasticity Today: Modelling, Methods and Applications, W. Olsak Memorial Volume*, A. Sawczuk and V. Bianchi, eds., Elsevier Scientific Publishing Co., Amsterdam, 1985, pp. 623-642.
25. J.L. Teply and G.J. Dvorak, 'Bounds on overall instantaneous properties of elastic-plastic composites,' *J. Mech. Phys. Solids* **36**, 29-58 (1988).
26. G.J. Dvorak, Y.A. Bahei-El-Din and A.M. Wafa, 'Implementation of the transformation field analysis for inelastic composite materials,' *Computational Mechanics* **14**, 201-228 (1994).

27. G.J. Dvorak, 'Plasticity theories for fibrous composite materials,' In *Metal Matrix Composites, Mechanisms and Properties*, R.K. Everett and R.J. Arsenault, eds., vol. 2, Academic Press, Boston, 1991, pp. 1-77.
28. G.J. Dvorak and Y. Benveniste, 'On transformation strains and uniform fields in multiphase elastic media,' *Proceedings of the Royal Society London A* **437**, 291-310 (1992).
29. R. Hill, 'A self-consistent mechanics of composite materials," *J. Mech. Phys. Solids* **13**, 213-222 (1965).
30. T.W. Clyne and P.J. Withers, *An Introduction to Metal Matrix Composites*, Cambridge University Press, Cambridge, 1993.
31. O.C. Zienkiewicz and I.C. Corneau, 'Viscoplasticity-plasticity and creep in elastic solids - a unified numerical solution approach,' *Int. J. Numer. Methods Engng.* **8**, 821-845 (1974).
32. C.W. Gear, *Numerical Initial Value Problems in Ordinary Differential Equations*, Prentice-Hall, Englewood Cliffs, New Jersey, 1971.
33. A.C. Hindmarsh, *GEAR: Ordinary differential equations system solver*, Lawrence Livermore Laboratory, Report UCID-30001, Revision 3, 1974.
34. Y.A. Bahei-El-Din and G.J. Dvorak, 'Mechanics of hot isostatic pressing of a densified unidirectional SiC/Ti composite,' *Acta Metallurgica et Materialia* **43**, 2531-2539 (1995).
35. Y.A. Bahei-El-Din, G.J. Dvorak and J.F. Wu, 'Mechanics of hot isostatic pressing in intermetallic matrix composites,' *J. Materials Science* **30**, 1-23 (1995).
36. Y.A. Bahei-El-Din, 'Uniform fields, yielding and thermal hardening in fibrous composite laminates,' *Int. J. Plasticity* **8**, 867-892 (1992).
37. G.J. Dvorak, T. Chen, and J.L. Teply, 'Thermomechanical stress fields in high-temperature fibrous composites: II. Laminated plates,' *Composites Science and Technology* **43**, 359-368 (1992).

38. R. Hill, 'Elastic properties of reinforced solids: Some theoretical principles,' *J. Mech. Phys. Solids* 11, 357–372 (1963).
39. T. Chen, G.J. Dvorak, and Y. Benveniste, 'Mori–Tanaka estimates of the overall elastic moduli of certain composite materials,' *J. Appl. Mech.* 59, 539–546 (1992).

## APPENDIX

Suppose that the fiber and matrix moduli and coefficients of thermal expansion are represented by continuous functions of temperature  $\theta$ , derived from experimental data. After a uniform change  $\Delta\theta$ , from a reference temperature  $\theta_0$ , applied under a uniform stress  $\sigma_r$ , an unconstrained phase deforms uniformly,

$$\epsilon_r = \mathbf{M}_r(\theta) \sigma_r + \int_{\theta_0}^{\theta} \mathbf{m}_r(\theta) d\theta. \quad (\text{A-1})$$

If the temperature changes under an applied uniform strain, the stress is:

$$\sigma_r = \mathbf{L}_r(\theta) \left[ \epsilon_r - \int_{\theta_0}^{\theta} \mathbf{m}_r(\theta) d\theta \right], \quad (\text{A-2})$$

where  $r = f, m$  denotes the phase,  $\mathbf{L}_r(\theta)$  and  $\mathbf{M}_r(\theta) = [\mathbf{L}_r(\theta)]^{-1}$  are temperature dependent, (6x6) phase stiffness and compliance matrices,  $\mathbf{m}_r(\theta)$  is the (6x1) thermal strain vector of expansion coefficients, their particular forms depend on the elastic symmetry of the phase.

For a transversely isotropic solid, with  $x_1$  as the axis of rotational symmetry, and compliance matrix  $\mathbf{M}$ , the constitutive relation  $\epsilon = \mathbf{M} \sigma$  is written using the engineering moduli

$$\begin{Bmatrix} \epsilon_{11} \\ \epsilon_{22} \\ \epsilon_{33} \\ 2\epsilon_{23} \\ 2\epsilon_{31} \\ 2\epsilon_{12} \end{Bmatrix} = \begin{bmatrix} 1/E_{11} & -\nu_{21}/E_{22} & -\nu_{31}/E_{33} & 0 & 0 & 0 \\ & 1/E_{22} & -\nu_{32}/E_{33} & 0 & 0 & 0 \\ & & 1/E_{33} & 0 & 0 & 0 \\ & & & 1/G_{23} & 0 & 0 \\ & & & & 1/G_{12} & 0 \\ & \text{SYM.} & & & & 1/G_{12} \end{bmatrix} \begin{Bmatrix} \sigma_{11} \\ \sigma_{22} \\ \sigma_{33} \\ \sigma_{23} \\ \sigma_{31} \\ \sigma_{12} \end{Bmatrix}. \quad (\text{A-3})$$

The stiffness  $\mathbf{L} = \mathbf{M}^{-1}$  is best written in terms of Hill's [38] moduli,

$$\begin{aligned} k &= -[1/G_{23} - 4/E_{22} + 4\nu_{21}^2/E_{11}]^{-1}, & \ell &= 2k \nu_{21} \\ n &= E_{11} + 4k \nu_{21}^2 = E_{11} + \ell^2/k, & m &= G_{23}, \quad p = G_{12}. \end{aligned}$$

The constitutive relation  $\sigma = \mathbf{L} \epsilon$  then is

$$\begin{Bmatrix} \sigma_{11} \\ \sigma_{22} \\ \sigma_{33} \\ \sigma_{23} \\ \sigma_{31} \\ \sigma_{12} \end{Bmatrix} = \begin{bmatrix} n & \ell & \ell & 0 & 0 & 0 \\ & (k+m) & (k-m) & 0 & 0 & 0 \\ & & (k+m) & 0 & 0 & 0 \\ & & & m & 0 & 0 \\ & \text{SYM.} & & & p & 0 \\ & & & & & p \end{bmatrix} \begin{Bmatrix} \epsilon_{11} \\ \epsilon_{22} \\ \epsilon_{33} \\ 2\epsilon_{23} \\ 2\epsilon_{31} \\ 2\epsilon_{12} \end{Bmatrix}. \quad (\text{A-4})$$

Estimates of the overall moduli  $L$  of heterogeneous solids by the Mori-Tanaka method are given in references [22, 23]. Also, the following formulas for the overall Hill's moduli of a fibrous composite in terms of the local moduli and the fiber volume fraction  $c_f$  were derived by Chen et al. [39] for the Mori-Tanaka method;

$$p = \frac{2c_f p_m p_f + c_m(p_m p_f + p_m^2)}{2c_f p_m + c_m(p_f + p_m)}, \quad (\text{A-5})$$

$$m = \frac{m_m m_f (k_m + 2m_m) + k_m m_m (c_f m_f + c_m m_m)}{k_m m_m + (k_m + 2m_m) (c_f m_m + c_m m_f)}, \quad (\text{A-6})$$

$$k = \frac{c_f k_f (k_m + m_m) + c_m k_m (k_f + m_m)}{c_f (k_m + m_m) + c_m (k_f + m_m)}, \quad (\text{A-7})$$

$$\ell = \frac{c_f \ell_f (k_m + m_m) + c_m \ell_m (k_f + m_m)}{c_f (k_m + m_m) + c_m (k_f + m_m)}, \quad (\text{A-8})$$

$$n = c_m n_m + c_f n_f + (\ell - c_f \ell_f - c_m \ell_m) \frac{\ell_f - \ell_m}{k_f - k_m}. \quad (\text{A-9})$$

Table 1 Results of static tests performed on Sigma/Timetal 21S laminates at 650°C.

Layup	Thermal Strain (%)	Stress Rate (MPa/s)	Elastic Modulus (GPa)	Ultimate Strength (MPa)	Ultimate Strain (%)
(0) <sub>4</sub>	0.40	0.278	130	804 <sup>a</sup>	1.205
		27.80	157	819 <sup>a</sup>	1.040
(0/90) <sub>s</sub>	0.46	0.278	100	408 <sup>a</sup>	1.076
		27.80	125	482 <sup>a</sup>	0.946
(0/±45/90) <sub>s</sub>	0.45	0.278	114	348 <sup>b</sup>	1.227
		27.80	125	431 <sup>a</sup>	0.962

<sup>a</sup> Plate A.

<sup>b</sup> Plate B.

Table 2 Experimental data for isothermal fatigue tests of Sigma/Timetal 21S laminates ( $R = 0.1$ ,  $\theta = 650^\circ\text{C}$ ).

Laminate	f = 0.001 Hz			f = 0.1 Hz		
	S <sub>max</sub> (MPa)	N <sub>f</sub>	ε <sub>ult</sub> (%)	S <sub>max</sub> (MPa)	N <sub>f</sub>	ε <sub>ult</sub> (%)
(0) <sub>4</sub>	700 <sup>bα</sup>	1018*	0.936	850 <sup>b</sup>	1223	1.165
	600 <sup>bβ</sup>	1750*	0.960	775 <sup>b</sup>	558	1.079
	575 <sup>b</sup>	17	0.939	750 <sup>a</sup>	5700	0.993
	562 <sup>a</sup>	2	0.969	725 <sup>b</sup>	2604	1.031
	500 <sup>a</sup>	17	1.074	700 <sup>b</sup>	10191	1.021
	450 <sup>a</sup>	208	1.110			
	425 <sup>a</sup>	2020	1.118			
(0/90) <sub>s</sub>	325 <sup>a</sup>	14	0.989	350 <sup>a</sup>	240	0.960
	300 <sup>a</sup>	1182*	0.904*	325 <sup>a</sup>	15906	0.984
				300 <sup>a</sup>	113750*	0.884*
				200 <sup>a</sup>	110000*	0.755*
(0/±45/90) <sub>s</sub>	300 <sup>a</sup>	11	1.150	300 <sup>b</sup>	207	1.110
	250 <sup>a</sup>	215	1.170	250 <sup>b</sup>	2850	1.070
	250 <sup>b</sup>	1201*	1.152*	250 <sup>b</sup>	12800	1.172
				200 <sup>b</sup>	105515*	0.941*
				200 <sup>b</sup>	18313*	0.960*

<sup>a</sup> Plate A.    <sup>b</sup> Plate B.

<sup>α</sup> 527 cycles at 600-60 MPa + 235 at 650-65 + 251 at 675-67.5 + 5 at 700-70.

\* Survived the number of cycles and strain indicated.

Table 3 Unloading elastic modulus (GPa) measured in quasistatic loading/unloading tests performed on (0/90)<sub>s</sub> Sigma/Timetal 21S laminates at room temperature.

Stress (MPa)	Reference Specimen	Specimen - 1	Specimen - 2
100	160	150	159
200	150	147	150
300	144		147
350	141		
400	136		
450	135	<u>Isothermal fatigue at 650°C:</u>	
475	134		
500	134	200 → 20 MPa	300 → 30 MPa
550	132	0.1 Hz	0.1 Hz
600	130	110000 cycles	113750 cycles
650	129		
<u>S<sub>ult</sub> = 650 MPa</u>		<u>294 MPa</u>	<u>350 MPa</u>

Table 4 Unloading elastic modulus (GPa) measured in quasistatic loading/unloading tests performed on (0/±45/90)<sub>s</sub> Sigma/Timetal 21S laminates at room temperature.

Stress (MPa)	Reference Specimen	Specimen - 1	Specimen - 2
100	155	139	140
200	150	135	135
300	134	125	131
350	125	119	131
400	119		127
		<u>Isothermal fatigue at 650°C:</u>	
		250 → 25 MPa	200 → 20 MPa
		0.001 Hz	0.1 Hz
		1201 cycles	105000 cycles
<u>S<sub>ult</sub> = 437 MPa</u>		<u>400 MPa</u>	<u>400 MPa</u>

Table 5 Elastic moduli and coefficients of thermal expansion

Sigma fiber				Timetal 21S matrix			
$\theta$ (°C)	E (GPa)	$\nu$	$\alpha$ ( $10^{-6}/^{\circ}\text{C}$ )	$\theta$ (°C)	E (GPa)	$\nu$	$\alpha$ ( $10^{-6}/^{\circ}\text{C}$ )
21	393	0.25	3.56	21	116	0.338	8.62
93	390	0.25	3.56	150	116	0.347	8.72
204	386	0.25	3.62	316	104	0.358	9.23
426	378	0.25	3.91	427	103	0.363	9.87
538	374	0.25	4.07	482	96	0.365	10.30
649	370	0.25	4.27	565	86	0.365	11.10
760	365	0.25	4.41	621	80	0.365	11.50
871	361	0.25	4.57	650	64	0.365	11.80
				704	53	0.374	12.00
				760	50	0.382	12.50

Table 6 Viscoplastic parameters for Timetal 21S

$\theta$ (°C)	Y (MPa)	$\mathcal{Y}$ (MPa)	$H_0$ (MPa)	h (MPa)	m	k (MPa) <sup>-p</sup> /s	p
21	925	1000	72	4024	1.365	2.10E-21	8.59
150	925	1000	72	4024	1.365	2.10E-21	8.59
316	645	785	146	5432	1.355	2.92E-16	6.52
427	630	770	143	5432	1.365	1.66E-14	5.62
482	505	615	103	3165	1.478	5.38E-13	6.35
565	190	365	256	6311	1.211	6.07E-12	5.52
621	85	185	149	2618	1.200	6.05E-10	3.58
650	30	87	42	1043	1.000	1.76E-08	2.00
704	24	53	45	829	1.000	1.50E-08	2.00
760	9	20	15	250	1.000	1.00E-08	2.00

Table 7 Nonzero local stress averages (MPa) caused in the fiber and matrix by hot isostatic pressing of a unidirectional Sigma/Timetal 21S composite

Temperature (°C)	Fiber Stresses			Matrix Stresses		
	$\sigma_{11}$	$\sigma_{22}$	$\sigma_{33}$	$\sigma_{11}$	$\sigma_{22}$	$\sigma_{33}$
21	-770	-228	-228	553	158	158
650	-136	-50	-50	94	35	35

Table 8 Nonzero local stress averages (MPa) caused by hot isostatic pressing in the plies of Sigma/Timetal 21S quasi-isotropic  $(0/90)_s$  and  $(0/\pm 45/90)_s$  laminates

Temperature (°C)	Ply Stresses		Fiber Stresses			Matrix Stresses		
	$\sigma_{11}$	$\sigma_{22}$	$\sigma_{11}$	$\sigma_{22}$	$\sigma_{33}$	$\sigma_{11}$	$\sigma_{22}$	$\sigma_{33}$
21	-157	157	-1095	-52	-232	492	302	161
650	-55	55	-293	15	-53	110	82	36

Table 9 Local stress averages (MPa) in plies of a Sigma/Timetal 21S (0/±45/90)<sub>s</sub> laminate caused by overall static axial loading at 650°C.

Ply	Local <sup>a</sup>	Under Overall Axial Stress (MPa)			
	Stress	18	26	59	65
	Component	90° ply debonding	±45° plies debonding	0° ply debonding	±45° plies sliding
0°	$\sigma_{11}^p$	-5	39	210	217
	$\sigma_{22}^p$	54	59	85	40
	$\sigma_{11}^f$	-195	-109	256	320
	$\sigma_{22}^f$	15	20	50	0
	$\sigma_{33}^f$	-53	-55	-65	0
	$\sigma_{11}^m$	127	141	177	145
	$\sigma_{22}^m$	82	86	110	67
	$\sigma_{33}^m$	37	38	45	0
45°	$\sigma_{11}^p$	-33	-10	53	77
	$\sigma_{22}^p$	69	84	47	50
	$\sigma_{12}^p$	15	26	54	54
	$\sigma_{11}^f$	-255	-214	-30	21
	$\sigma_{22}^f$	32	50	0	0
	$\sigma_{33}^f$	-54	-56	0	0
	$\sigma_{12}^f$	20	34	78	80
	$\sigma_{11}^m$	121	131	110	115
	$\sigma_{22}^m$	95	108	80	85
90°	$\sigma_{33}^m$	37	39	0	0
	$\sigma_{12}^m$	11	19	37	37
	$\sigma_{11}^p$	-61	-82	-77	-58
	$\sigma_{22}^p$	84	43	61	65
	$\sigma_{11}^f$	-314	-325	-319	-281
	$\sigma_{22}^f$	50	0	0	0
	$\sigma_{33}^f$	-54	0	0	0
	$\sigma_{11}^m$	115	85	90	97
	$\sigma_{22}^m$	107	72	103	110
	$\sigma_{33}^m$	38	0	0	0

<sup>a</sup>  $\sigma_{ij}^p$  = ply stress,  $\sigma_{ij}^f$  = fiber stress,  $\sigma_{ij}^m$  = matrix stress;  $x_1$  = axial direction

Table 10 Local stress averages (MPa) in the plies of a Sigma/Timetal 21S  
(0/±45/90)<sub>s</sub> laminate, caused by axial load cycles  
(S<sub>max</sub> = 300 MPa, R = 0.1, θ = 650°C).

Ply	Ply Stress	f = 0.001 Hz				f = 0.1 Hz			
		cycle 1		cycle 11 <sup>a</sup>		cycle 1		cycle 207 <sup>a</sup>	
		max.	min.	max.	min.	max.	min.	max.	min.
0°	$\sigma_{11}^p$	786	121	840	165	732	86	882	231
	$\sigma_{22}^p$	23	7	-11	-18	31	27	14	10
	$\sigma_{11}^f$	1749	333	1981	513	1492	243	1988	713
	$\sigma_{11}^m$	119	-25	51	-77	206	-22	117	-103
	$\sigma_{22}^m$	40	13	-19	-31	53	47	23	18
45°	$\sigma_{11}^p$	257	29	302	65	239	8	270	38
	$\sigma_{22}^p$	43	0	1	-33	62	24	15	-24
	$\sigma_{12}^p$	24	-11	18	-16	36	-10	4	-41
	$\sigma_{11}^f$	506	65	687	208	389	-32	613	185
	$\sigma_{11}^m$	84	3	35	-34	135	35	34	-63
	$\sigma_{22}^m$	73	1	2	-56	106	40	23	-41
	$\sigma_{12}^m$	40	-18	31	-26	60	-17	7	-69
90°	$\sigma_{11}^p$	-276	-58	-256	-44	-261	-78	-289	-106
	$\sigma_{22}^p$	67	-8	21	-45	95	22	17	-56
	$\sigma_{11}^f$	-739	-205	-609	-100	-717	-309	-756	-343
	$\sigma_{11}^m$	44	44	-11	-5	54	81	32	59
	$\sigma_{22}^m$	113	-14	35	-76	162	37	28	-94

<sup>a</sup> Number of cycles at failure found experimentally (Table 2)

## FIGURE CAPTIONS

- Figure 1. Temperature profile obtained for a Sigma/Timetal 21S specimen in a succesor furnace
- Figure 2. Applied stress, and measured total strain histories in a multistep creep test for a Timetal 21S specimen at 650°C
- Figure 3. Creep strains computed from the experimental data of Fig. 2
- Figure 4. Cyclic loading applied to a Timetal 21S specimen at 650°C
- Figure 5. Maximum and minimum strains measured under the cyclic loading of Fig. 4
- Figure 6. Maximum and minimum strains produced under each of the cyclic stress ranges of Fig. 4
- Figure 7. Tensile stress-strain data measured for Sigma/Timetal 21S laminates at 650°C under two stress rates
- Figure 8. Total axial strain histories measured in multistep creep tests for two  $(0)_4$  Sigma/Timetal 21S laminates at 650°C
- Figure 9. Total axial strain history measured in a multistep creep test for a  $(0/90)_s$  Sigma/Timetal 21S laminate at 650°C
- Figure 10. Total axial strain history measured in a multistep creep test for a  $(0/\pm 45/90)_s$  Sigma/Timetal 21S laminate at 650°C
- Figure 11. Total axial strain history measured for a  $(0)_4$  Sigma/Timetal 21S laminate at 650°C under the slow load cycles shown in inset
- Figure 12. Total axial strain history measured for a  $(0)_4$  Sigma/Timetal 21S laminate at 650°C under the fast load cycles shown in inset
- Figure 13. Stress-axial strain response measured for a  $(0)_4$  Sigma/Timetal 21S laminate under the slow load cycles shown in inset of Fig. 11
- Figure 14. Stress-axial strain response measured for a  $(0)_4$  Sigma/Timetal 21S laminate under the fast load cycles shown in inset of Fig. 12
- Figure 15. Total axial strain history measured for a  $(0/90)_s$  Sigma/Timetal 21S laminate at 650°C under the slow load cycles shown in inset
- Figure 16. Total axial strain history measured for a  $(0/90)_s$  Sigma/Timetal 21S laminate at 650°C under the fast load cycles shown in inset
- Figure 17. Stress-axial strain response measured for a  $(0/90)_s$  Sigma/Timetal 21S laminate under the slow load cycles shown in inset of Fig. 15
- Figure 18. Stress-axial strain response measured for a  $(0/90)_s$  Sigma/Timetal 21S laminate under the fast load cycles shown in inset of Fig. 16

- Figure 19. Total axial strain history measured for a  $(0/\pm 45/90)_s$  Sigma/Timetal 21S laminate at 650°C under the slow load cycles shown in inset
- Figure 20. Total axial strain history measured for a  $(0/\pm 45/90)_s$  Sigma/Timetal 21S laminate at 650°C under the fast load cycles shown in inset
- Figure 21. Stress-axial strain response measured for a  $(0/\pm 45/90)_s$  Sigma/Timetal 21S laminate under the slow load cycles shown in inset of Fig. 19
- Figure 22. Stress-axial strain response measured for a  $(0/\pm 45/90)_s$  Sigma/Timetal 21S laminate under the fast load cycles shown in inset of Fig. 20
- Figure 23. Maximum stress-cycles to failure (S-N) data measured for Sigma/Timetal 21S laminates at 650°C under two frequencies
- Figure 24. Variation of secant modulus measured in two  $(0)_4$  Sigma/Timetal 21S laminates subjected to cyclic loading at 650°C
- Figure 25. Maximum strains measured at failure in fatigue tests of Sigma/Timetal 21S laminates at 650°C
- Figure 26. Finite element model of a  $(0/\pm 45/90)_s$  laminate
- Figure 27. Thermomechanical loading applied to Sigma/Timetal 21S laminates in fabrication by hot isostatic pressing and aging
- Figure 28. Variation of the transverse normal stress in fully bonded fibers of a Sigma/Timetal 21S  $(0/90)_s$  laminate with the overall axial stress
- Figure 29. Variation of the transverse normal stress, and longitudinal shear stress in fully bonded fibers of a Sigma/Timetal 21S  $(0/\pm 45/90)_s$  laminate with the overall axial stress
- Figure 30. Isothermal cyclic loading applied to a Sigma/Timetal 21S  $(0/\pm 45/90)_s$  laminate
- Figure 31. Stress average computed in the  $0^\circ$  ply of a Sigma/Timetal 21S  $(0/\pm 45/90)_s$  laminate subjected to HIP and isothermal cyclic loading
- Figure 32. Fiber stress average computed in the  $0^\circ$  ply of a Sigma/Timetal 21S  $(0/\pm 45/90)_s$  laminate subjected to HIP and isothermal cyclic loading
- Figure 33. Matrix stress average computed in the  $0^\circ$  ply of a Sigma/Timetal 21S  $(0/\pm 45/90)_s$  laminate subjected to HIP and isothermal cyclic loading
- Figure 34. Stress average computed in the  $45^\circ$  ply of a Sigma/Timetal 21S  $(0/\pm 45/90)_s$  laminate subjected to HIP and isothermal cyclic loading
- Figure 35. Fiber stress average computed in the  $45^\circ$  ply of a Sigma/Timetal 21S  $(0/\pm 45/90)_s$  laminate subjected to HIP and isothermal cyclic loading
- Figure 36. Matrix stress average computed in the  $45^\circ$  ply of a Sigma/Timetal 21S  $(0/\pm 45/90)_s$  laminate subjected to HIP and isothermal cyclic loading
- Figure 37. Stress average computed in the  $90^\circ$  ply of a Sigma/Timetal 21S  $(0/\pm 45/90)_s$  laminate subjected to HIP and isothermal cyclic loading

Figure 38 Fiber stress average computed in the  $90^\circ$  ply of a Sigma/Timetal 21S  $(0/\pm 45/90)_s$  laminate subjected to HIP and isothermal cyclic loading.

Figure 39 Matrix stress average computed in the  $90^\circ$  ply of a Sigma/Timetal 21S  $(0/\pm 45/90)_s$  laminate subjected to HIP and isothermal cyclic loading

Figure 40 Measured and computed maximum overall axial strains in Sigma/Timetal 21S laminates under isothermal fatigue loading conditions shown in Table 2 for the slow cycle at 0.001 Hz

Figure 41 Measured and computed maximum overall axial strains in Sigma/Timetal 21S laminates under isothermal fatigue loading conditions shown in Table 2 for the fast cycle at 0.1 Hz

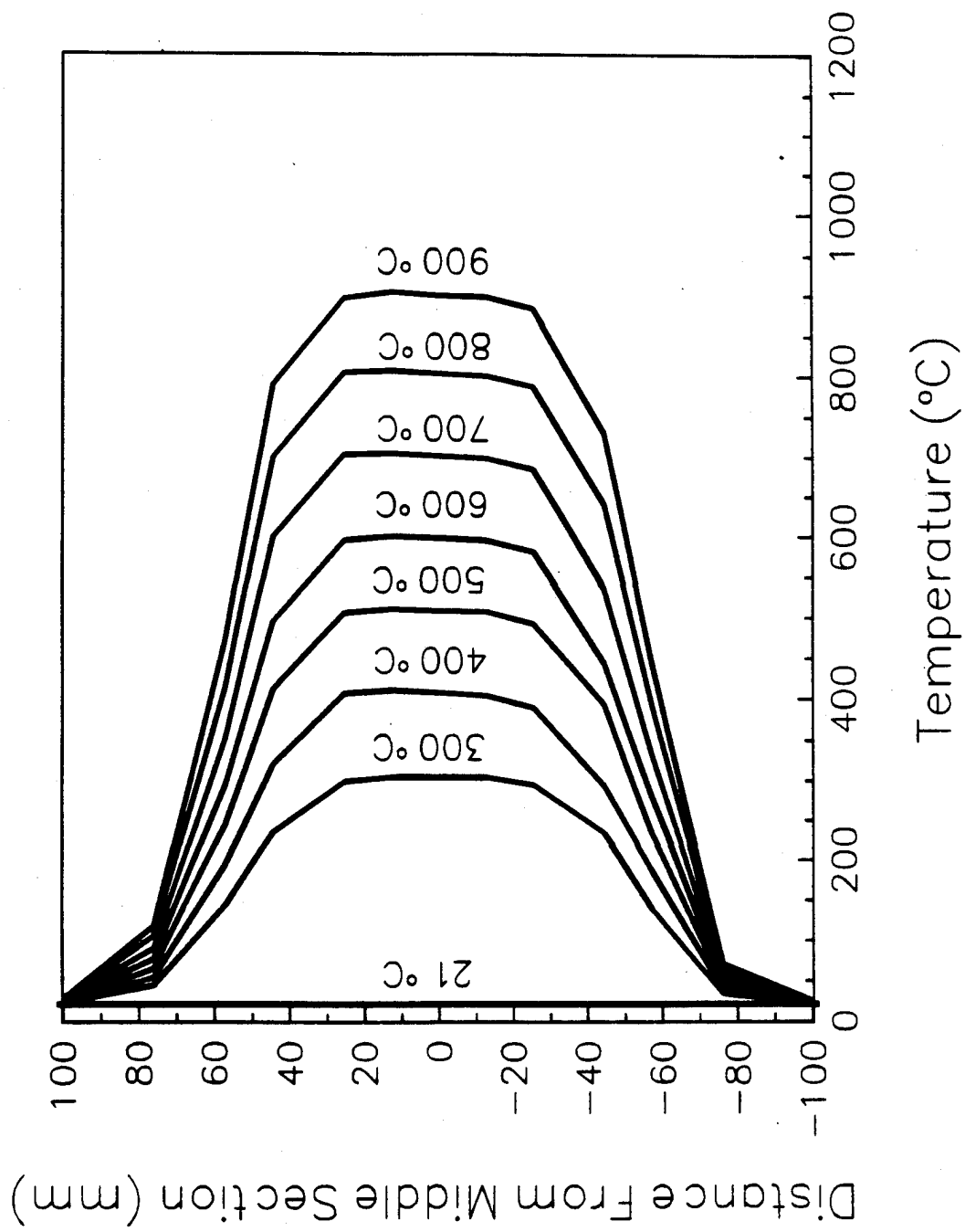


Figure 1. Temperature profile obtained for a Sigma/Timetal 21S specimen in a succceptor furnace

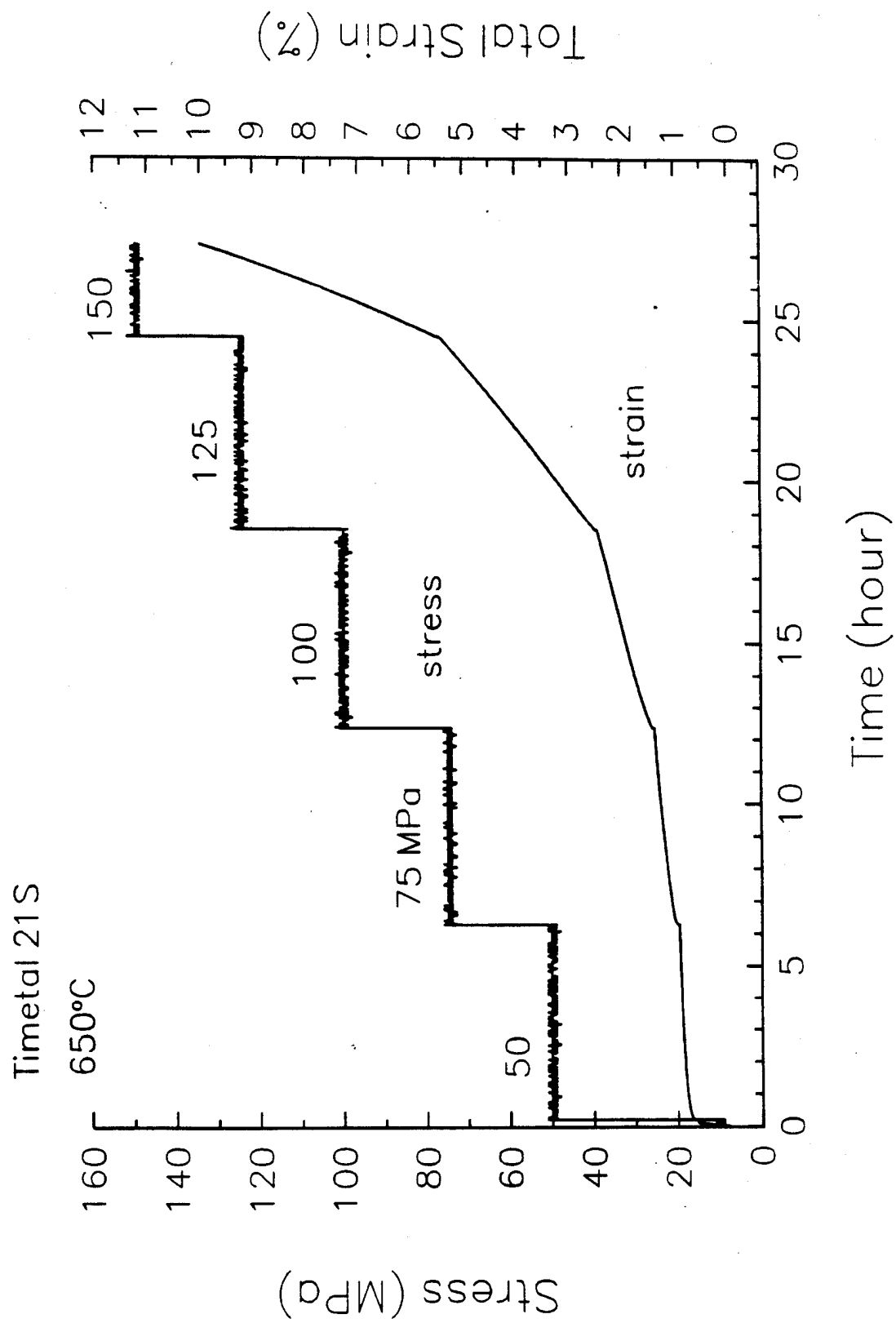


Figure 2. Applied stress, and measured total strain histories in a multistep creep test for a Timetal 21S specimen at 650°C

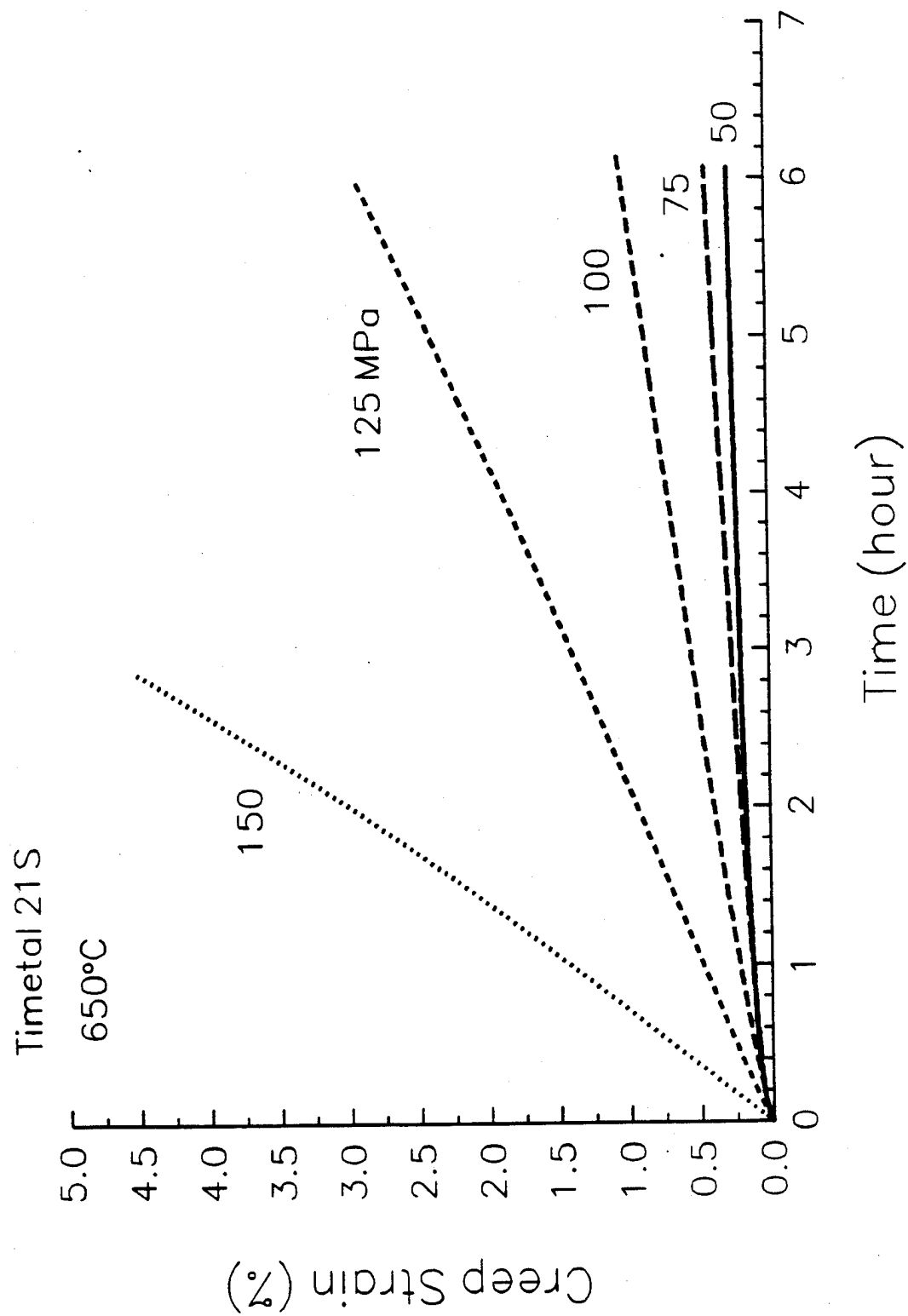


Figure 3. Creep strains computed from the experimental data of Fig. 2

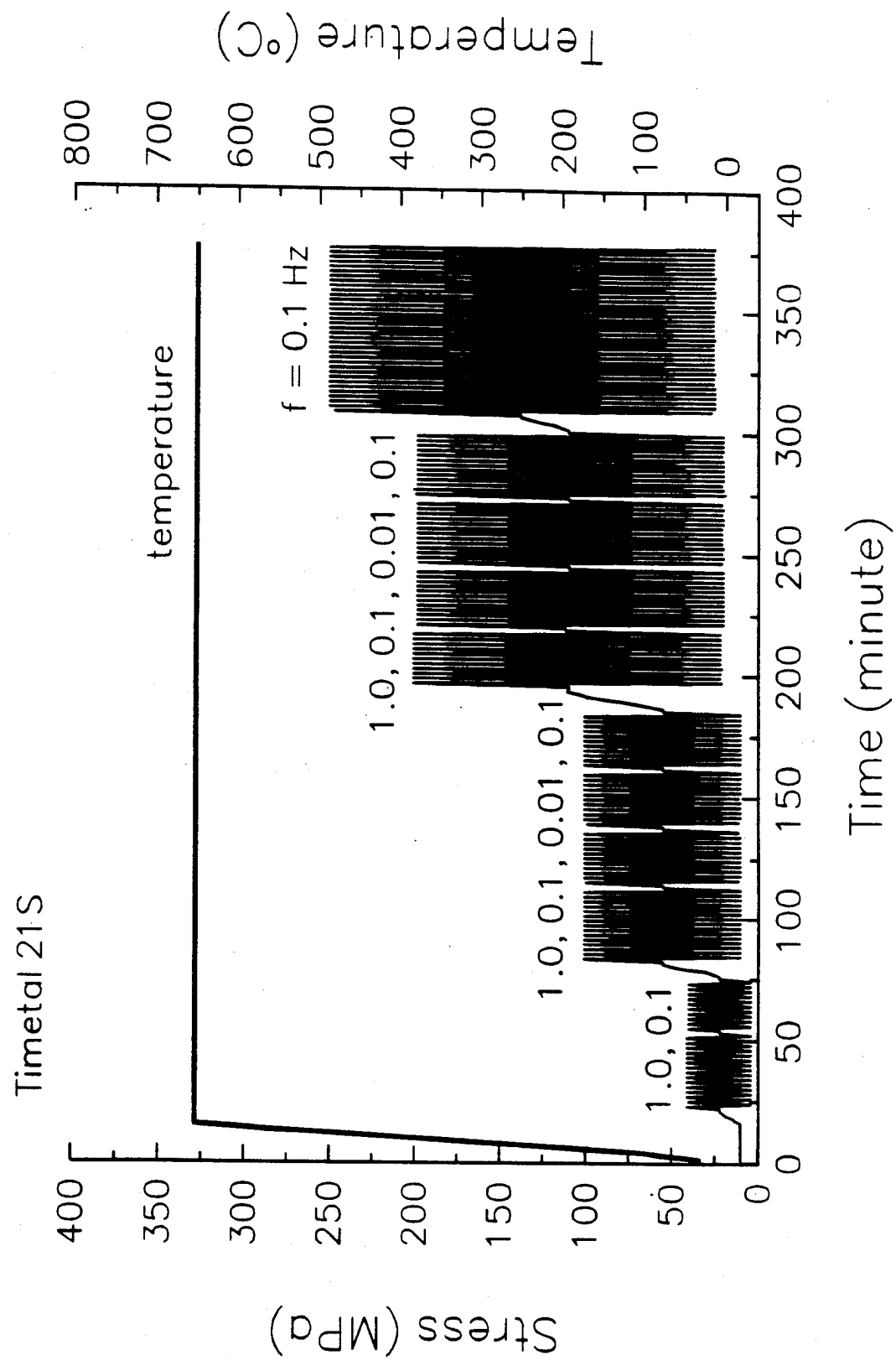
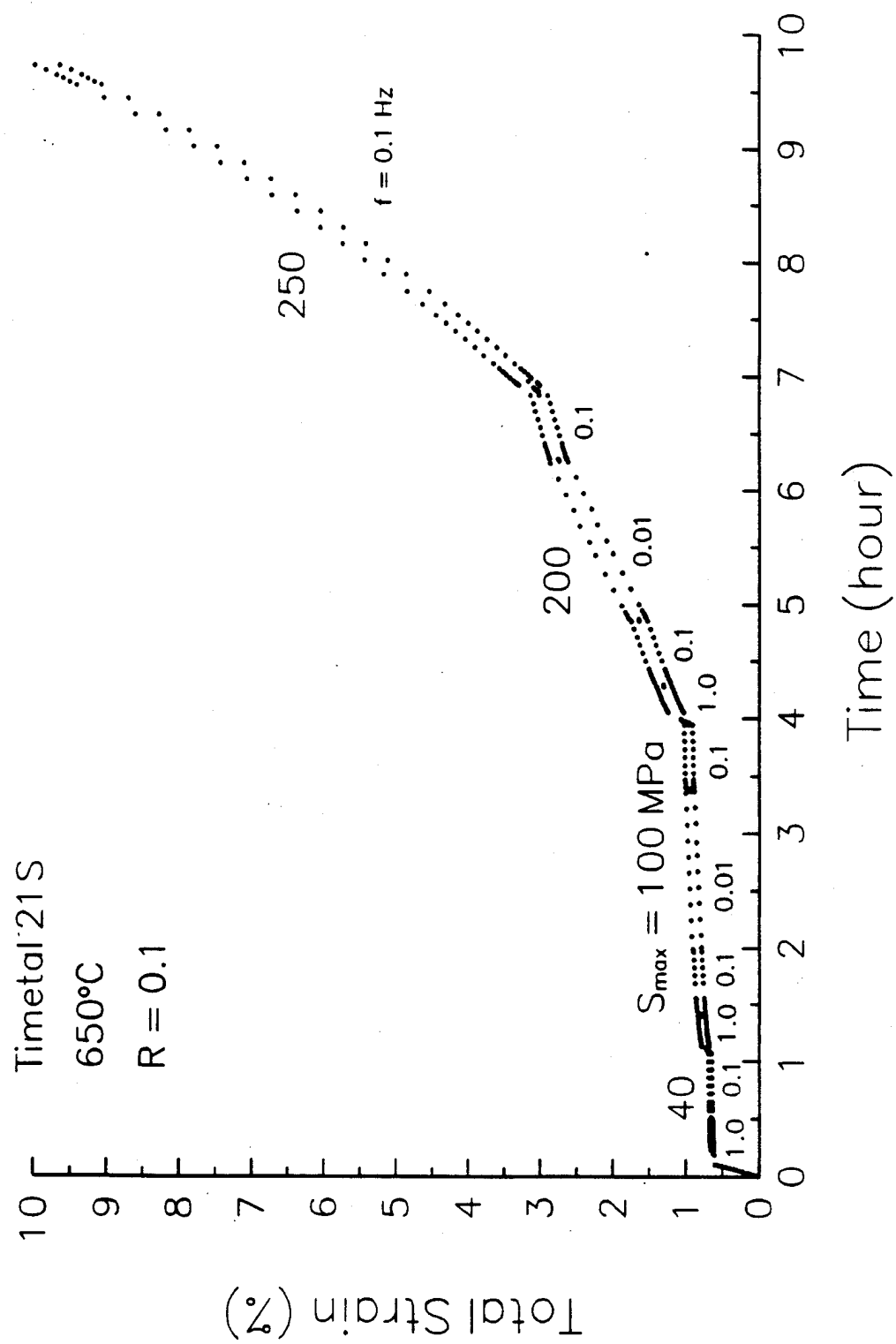


Figure 4. Cyclic loading applied to a Timetal 21S specimen at  $650^{\circ}\text{C}$



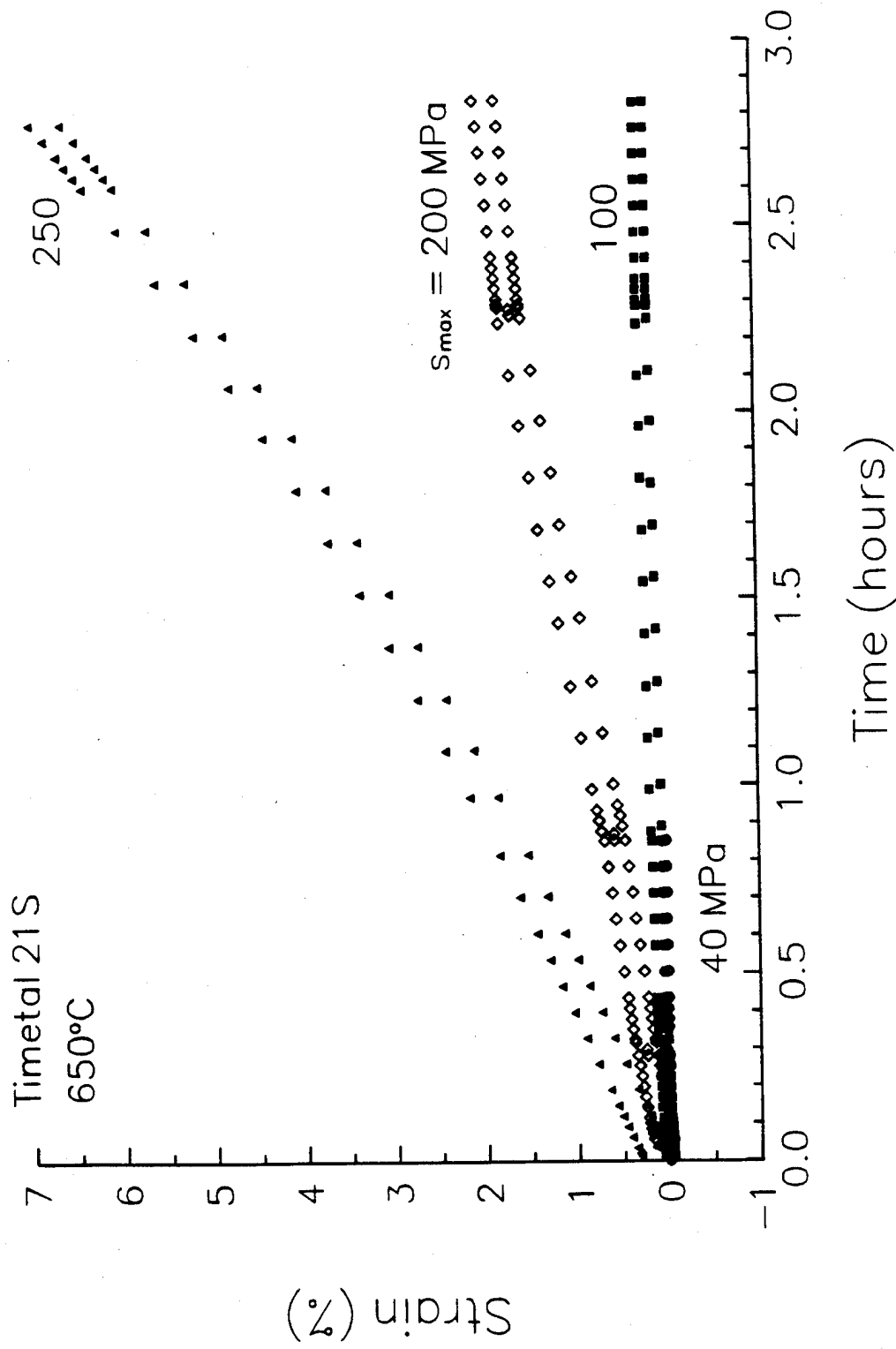


Figure 6. Maximum and minimum strains produced under each of the cyclic stress ranges of Fig. 4

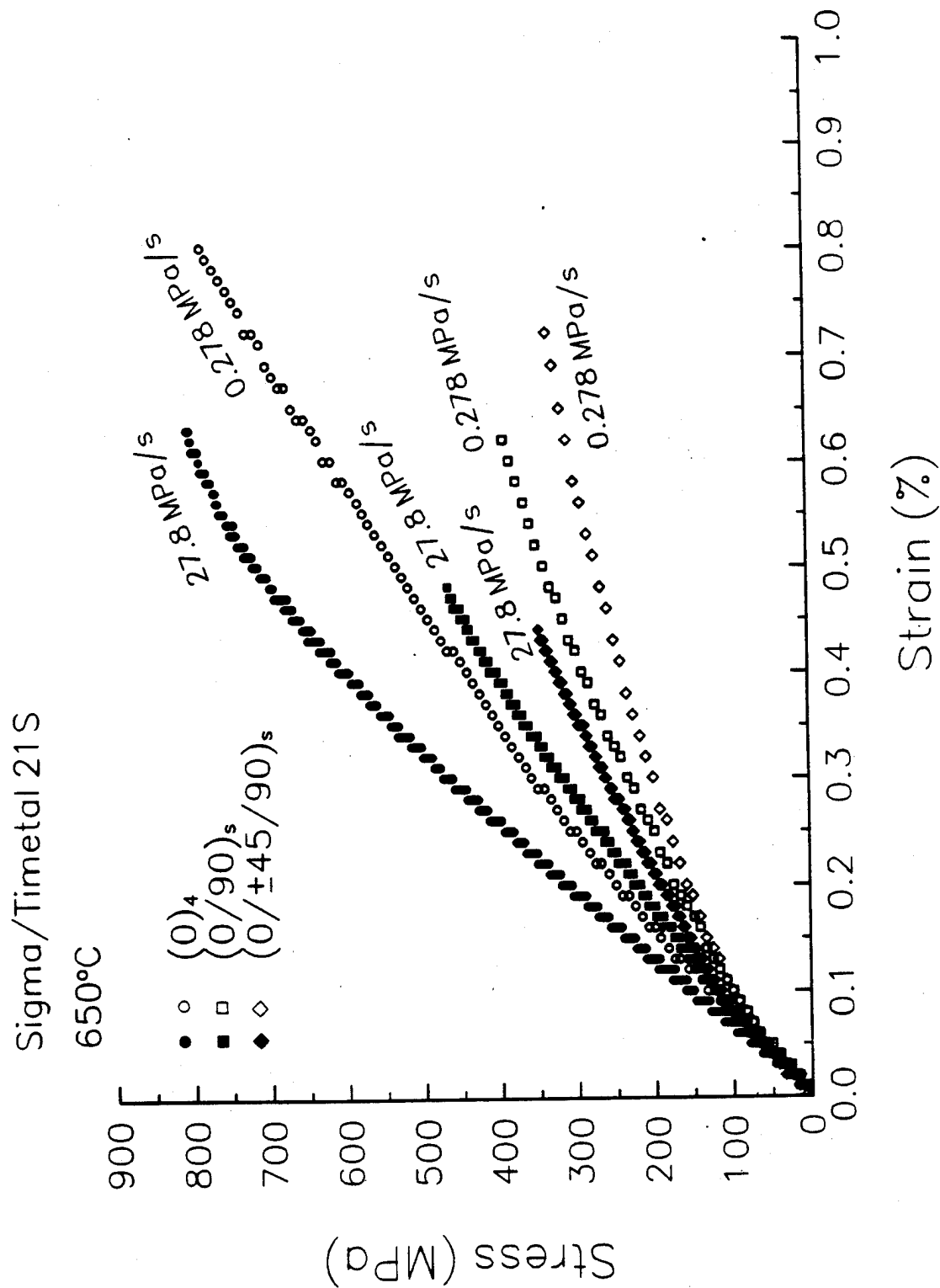


Figure 7. Tensile stress-strain data measured for Sigma/Timetal 21S laminates at 650°C under two stress rates

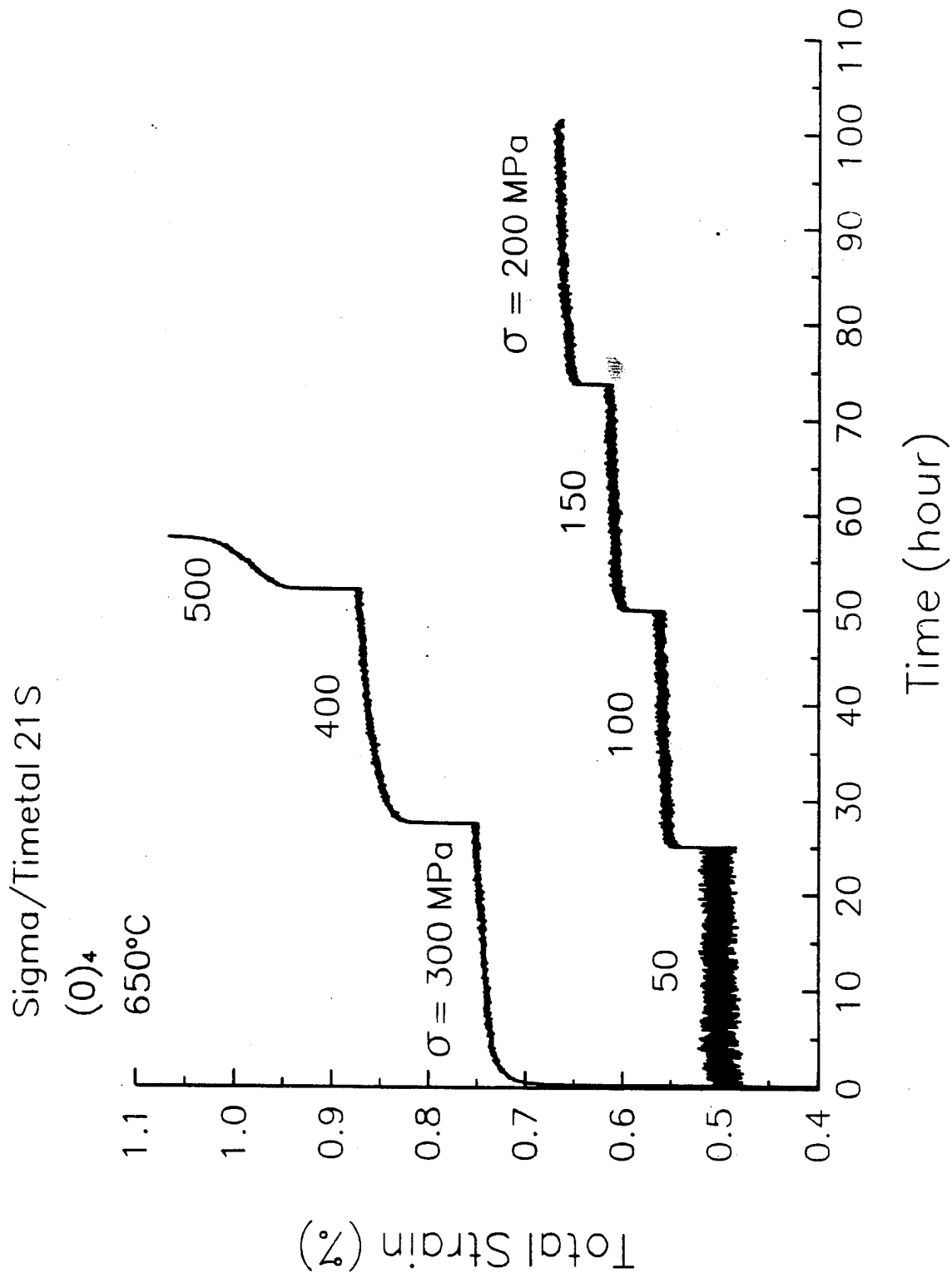


Figure 8. Total axial strain histories measured in multistep creep tests for two  $(0)_4$  Sigma/Timetal 21S laminates at  $650^\circ\text{C}$

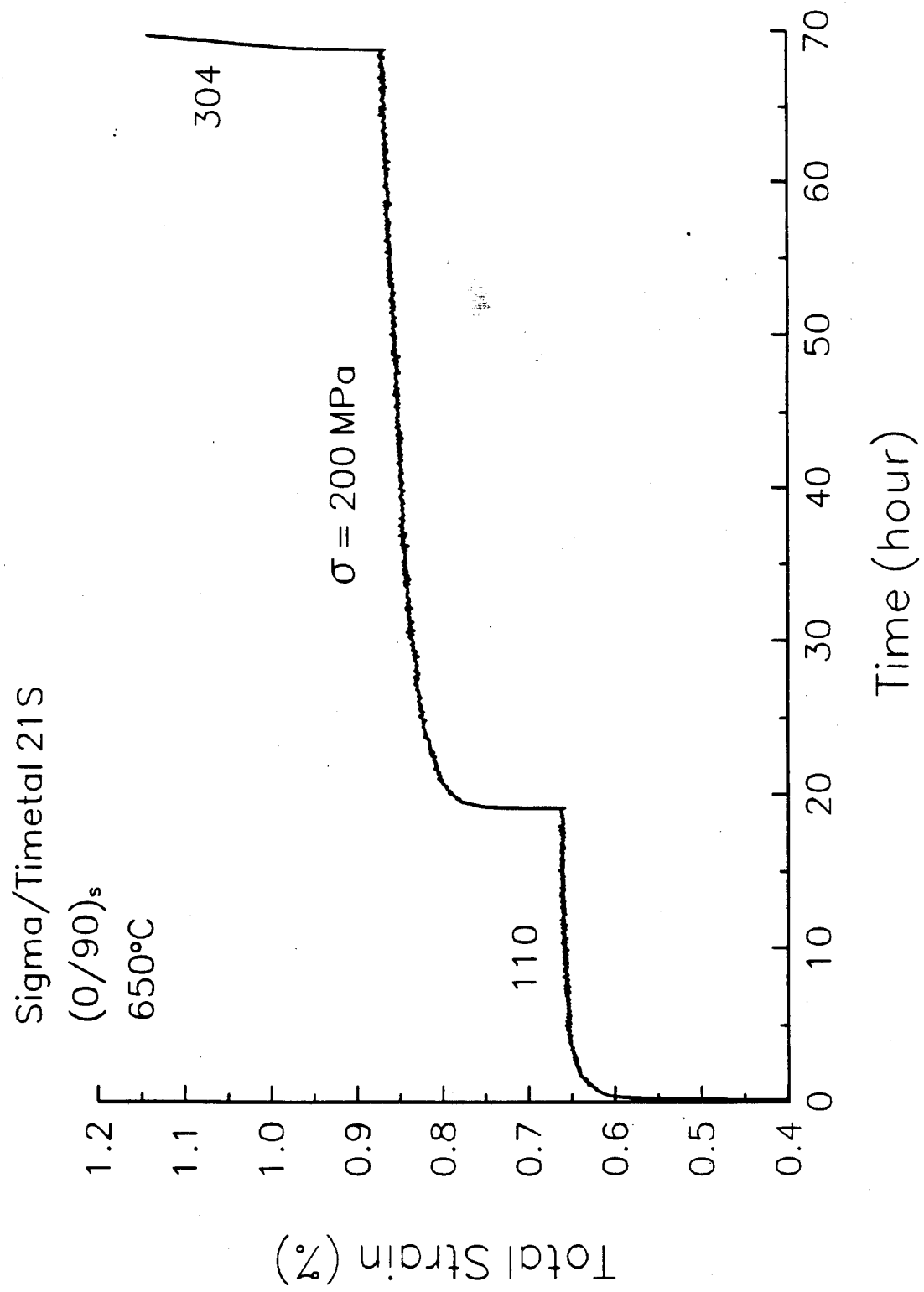


Figure 9. Total axial strain history measured in a multistep creep test for a (0/90)<sub>s</sub> Sigma/Timetal 21S laminate at 650°C

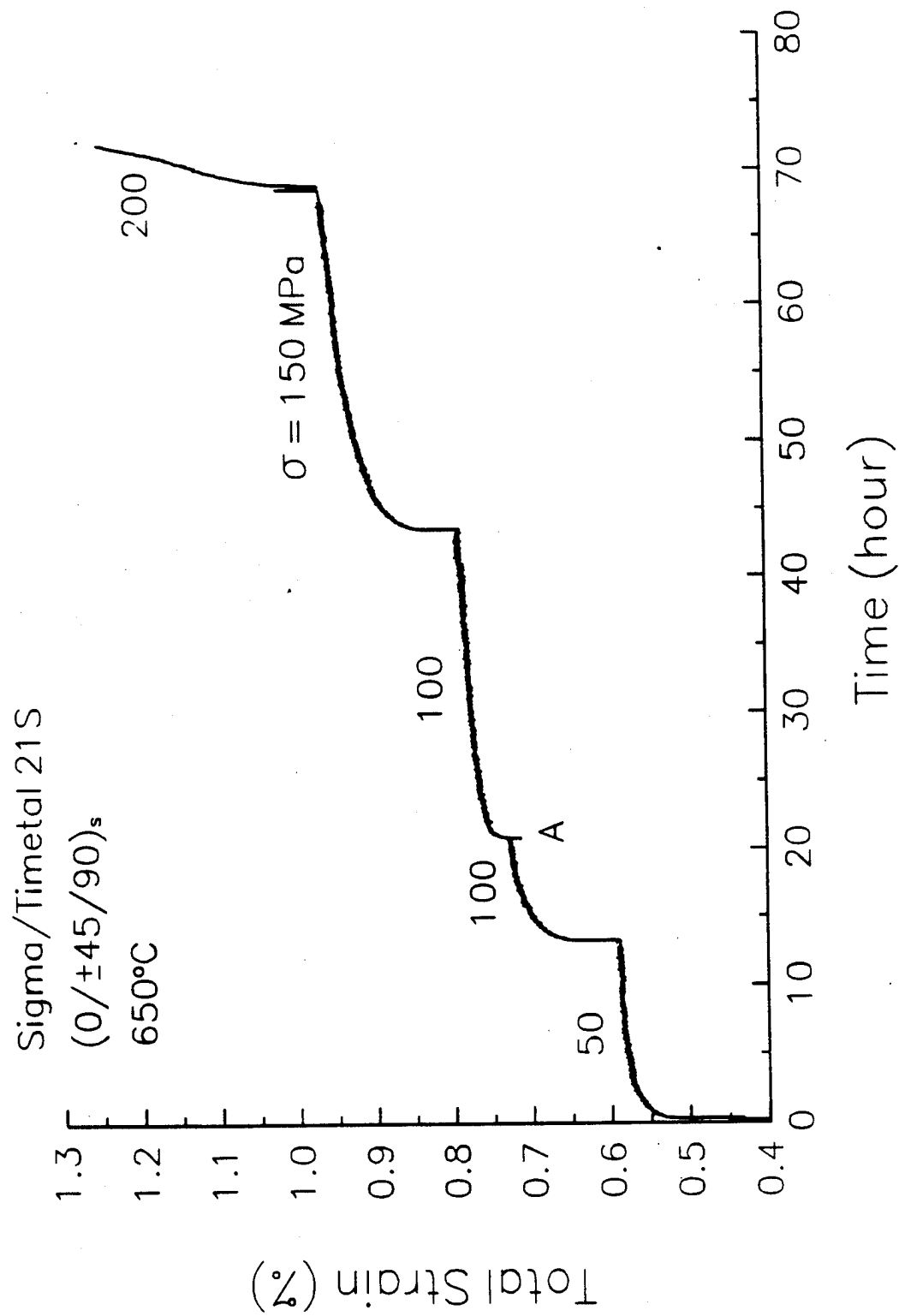


Figure 10. Total axial strain history measured in a multistep creep test for a  $(0/\pm 45/90)_s$  Sigma/Timetal 21S laminate at  $650^\circ\text{C}$

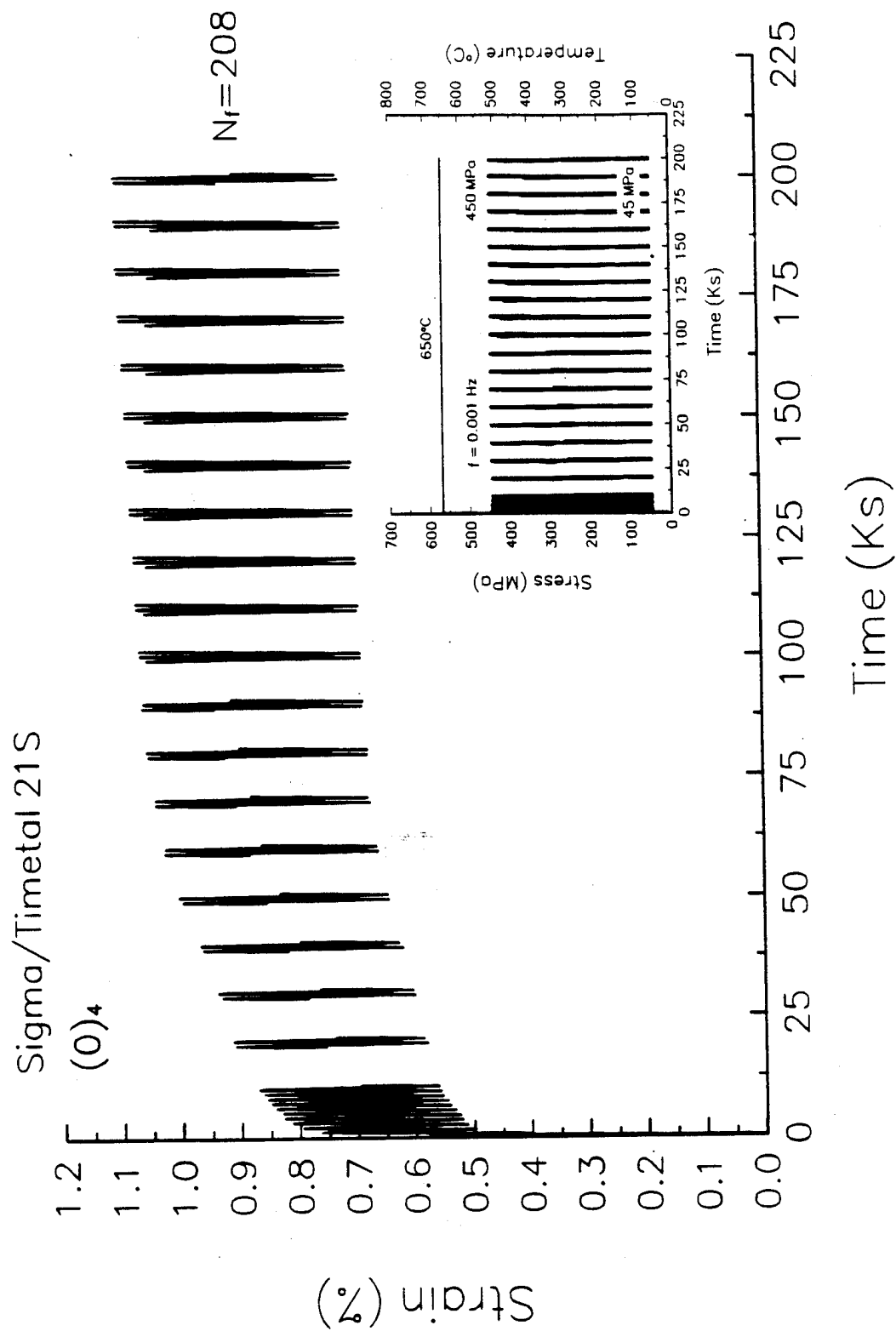


Figure 11. Total axial strain history measured for a  $(0)_4$  Sigma/Timetal 21S laminate at  $650^\circ\text{C}$  under the slow load cycles shown in inset

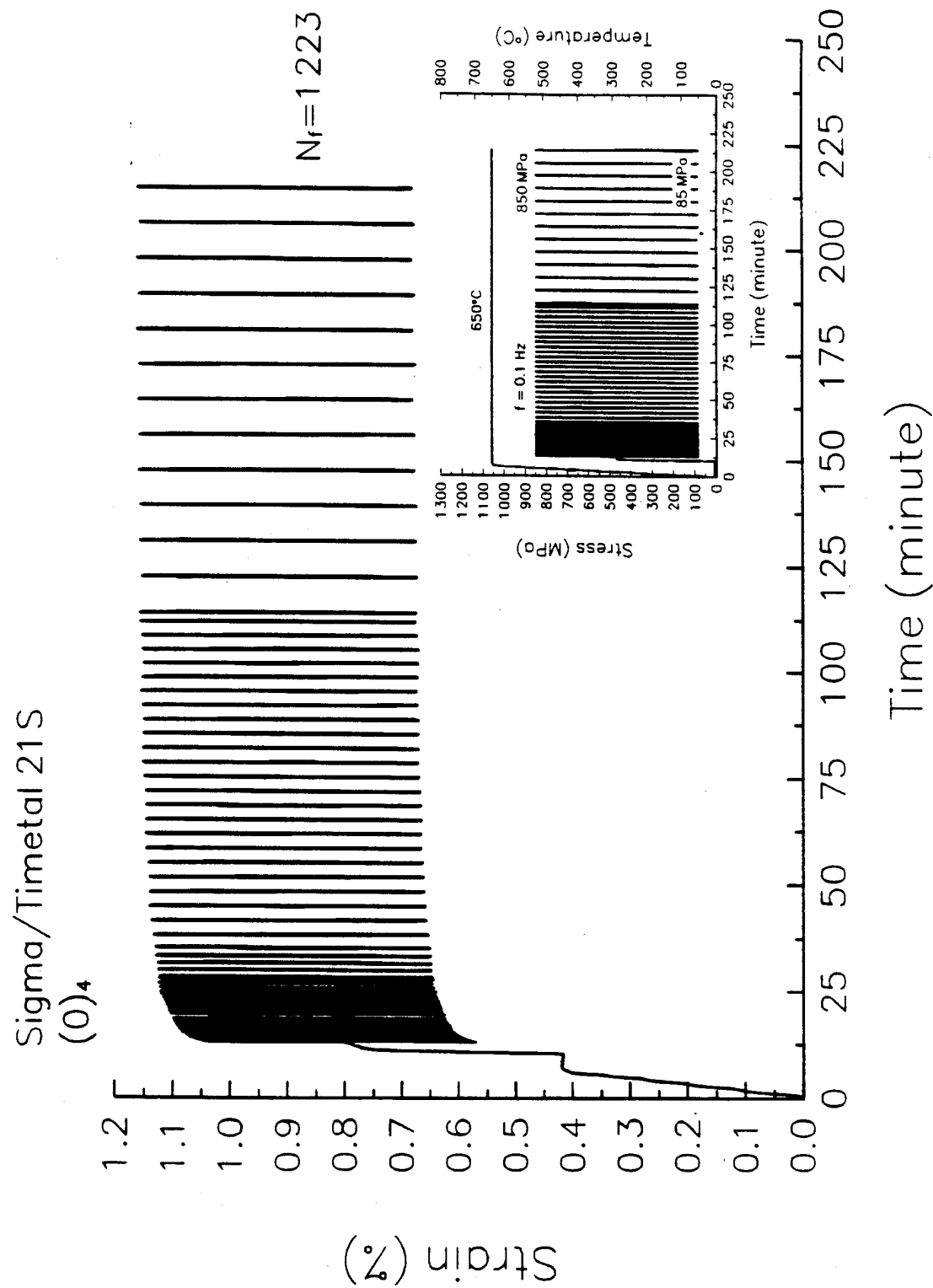


Figure 12. Total axial strain history measured for a  $(0)_4$  Sigma/Timetal 21S laminate at 650°C under the fast load cycles shown in inset

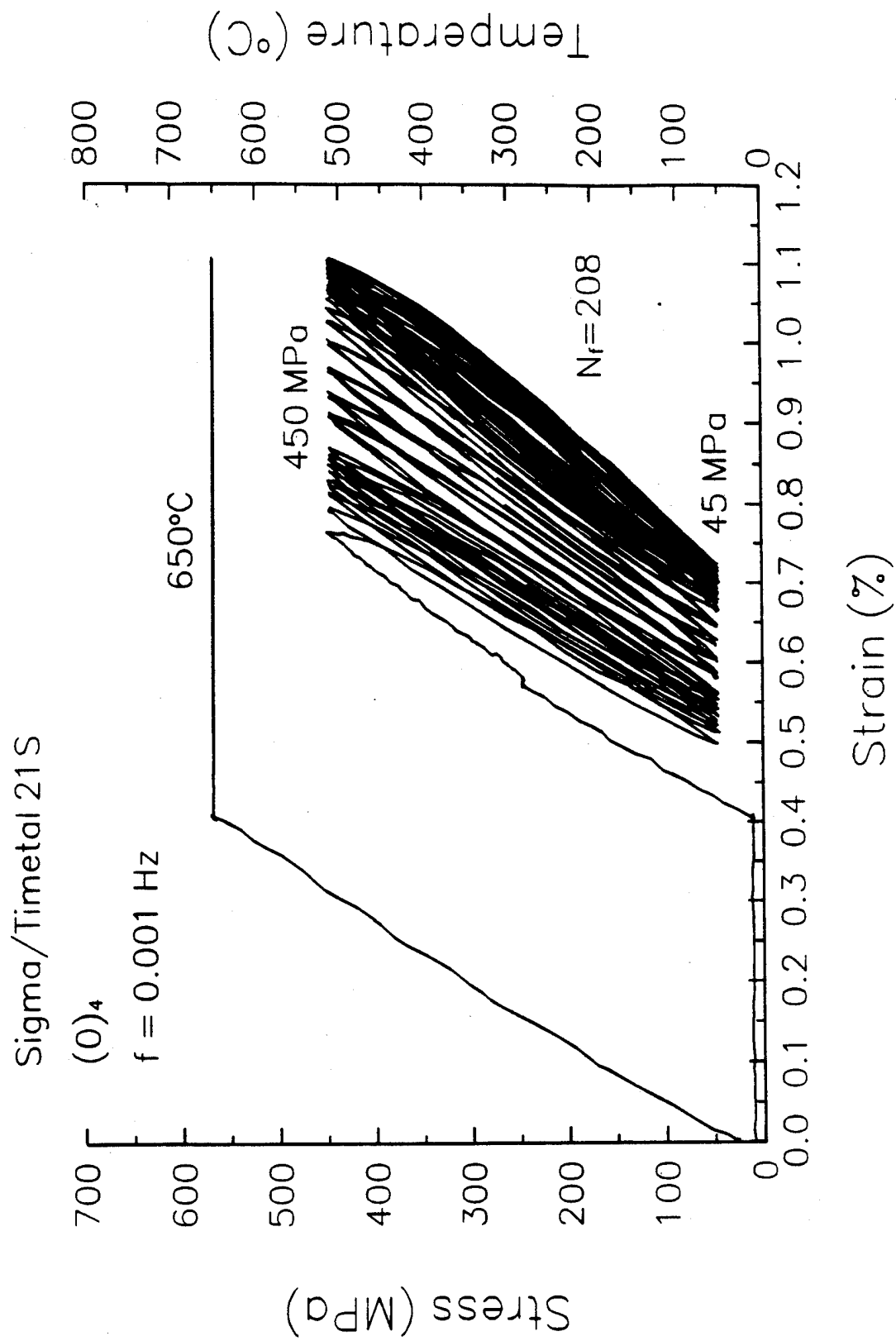


Figure 13. Stress-axial strain response measured for a (0)<sub>4</sub> Sigma/Timetal 21S laminate under the slow load cycles shown in inset of Fig. 11.

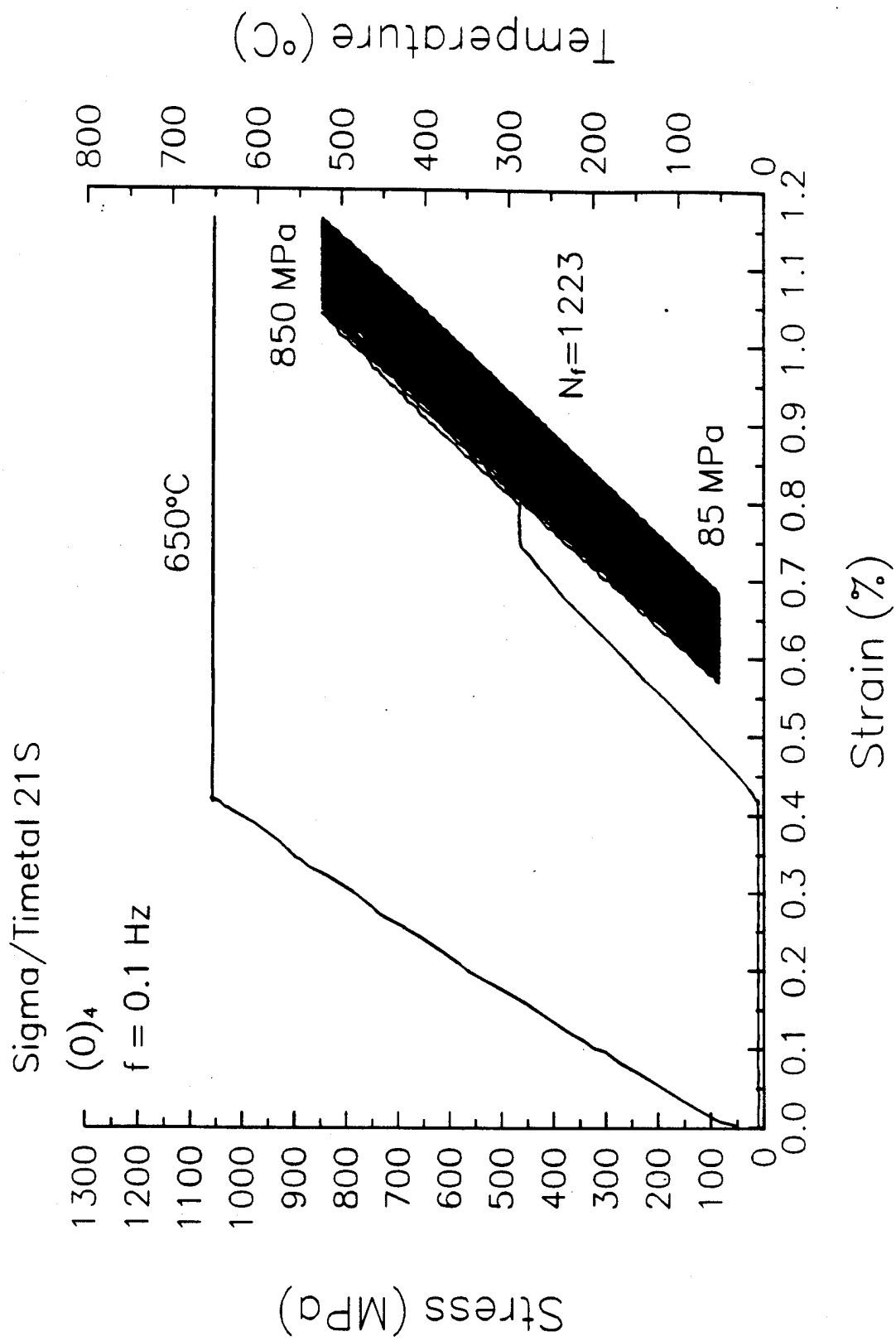


Figure 14. Stress-axial strain response measured for a  $(0)_4$  Sigma/Timetal 21S laminate under the fast load cycles shown in inset of Fig. 12

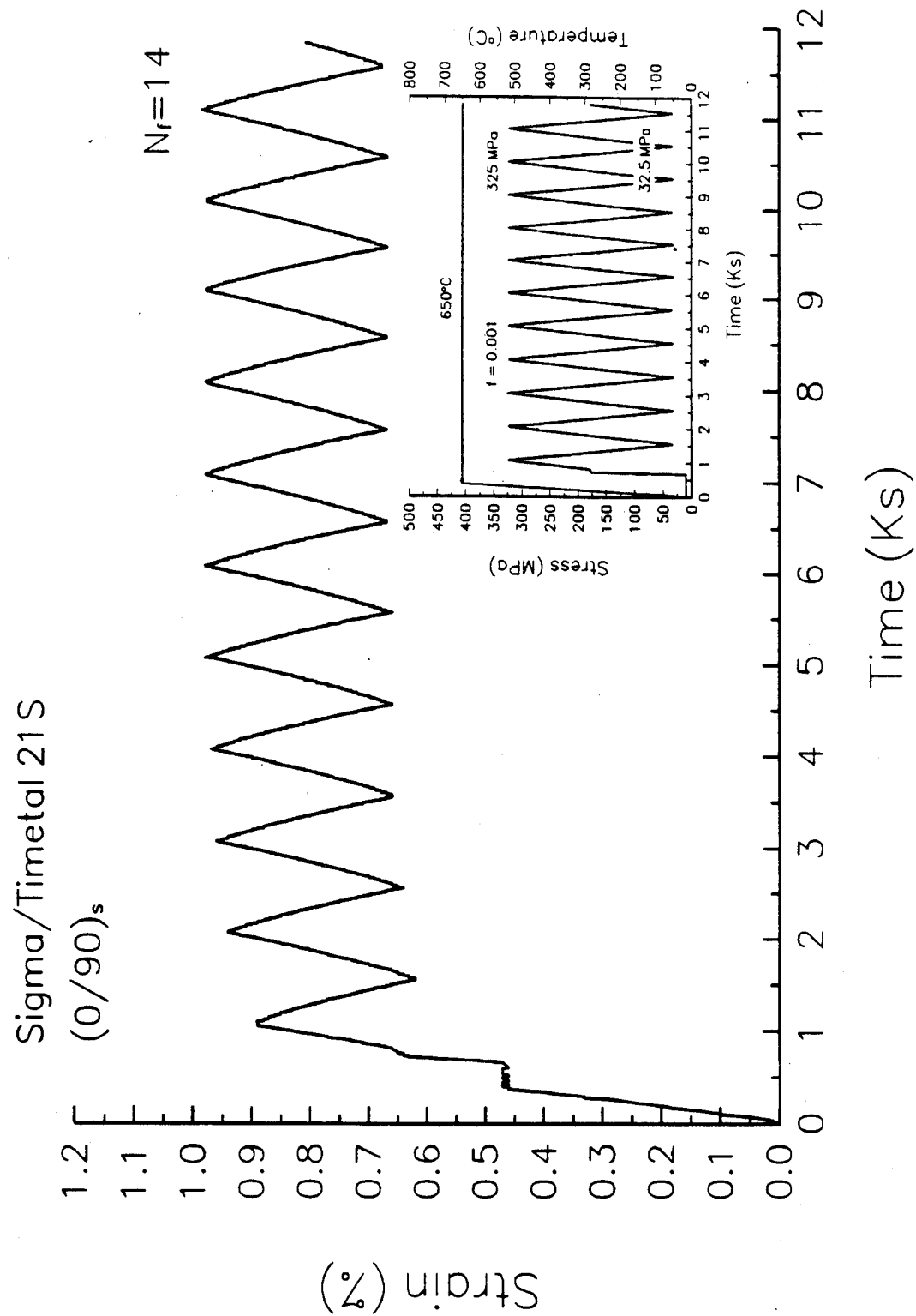


Figure 15. Total axial strain history measured for a (0/90)<sub>s</sub> Sigma/Timetal 21S laminate at 650°C under the slow load cycles shown in inset

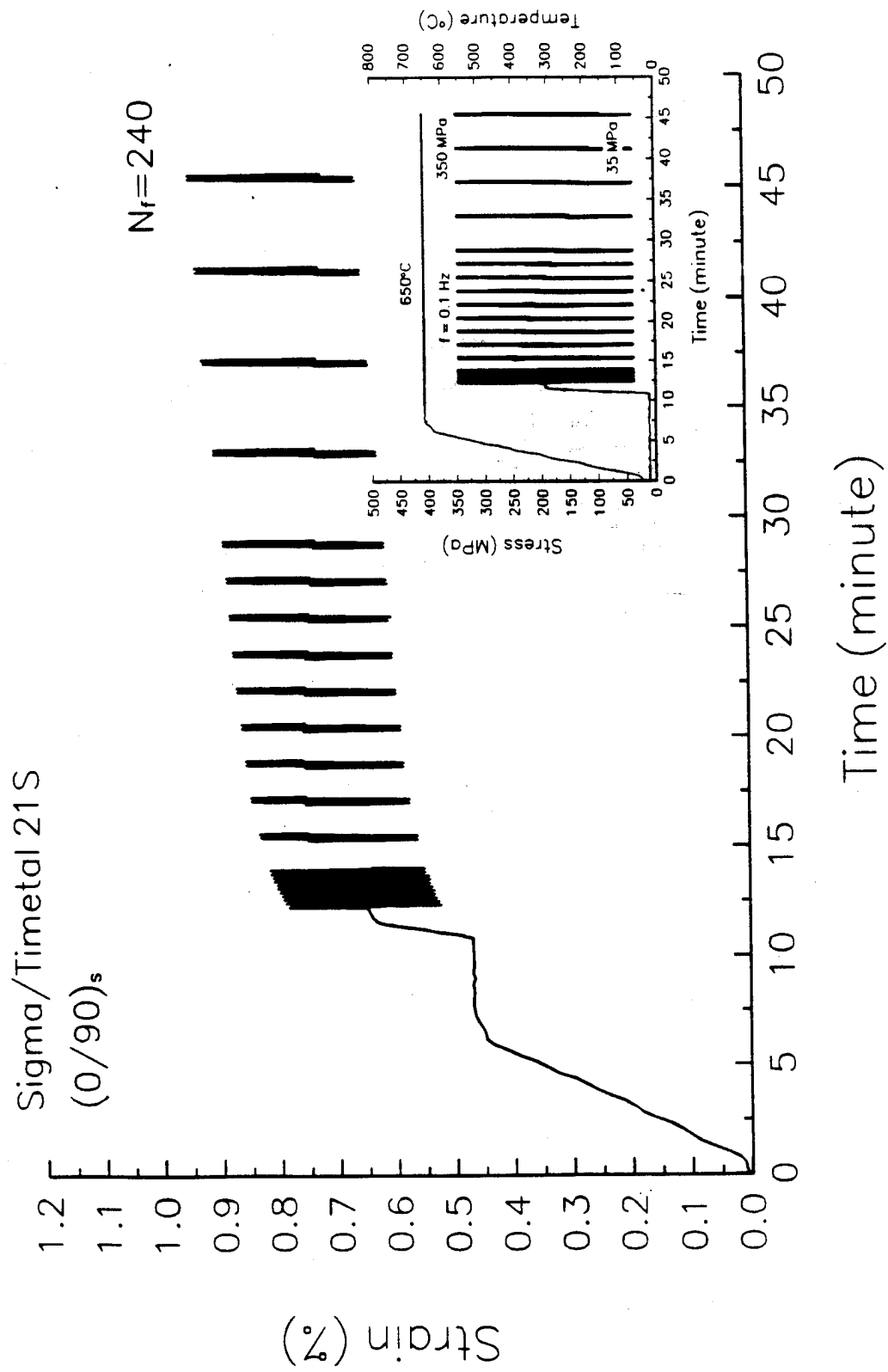


Figure 16. Total axial strain history measured for a  $(0/90)_s$  Sigma/Timetal 21S laminate at  $650^\circ\text{C}$  under the fast load cycles shown in inset

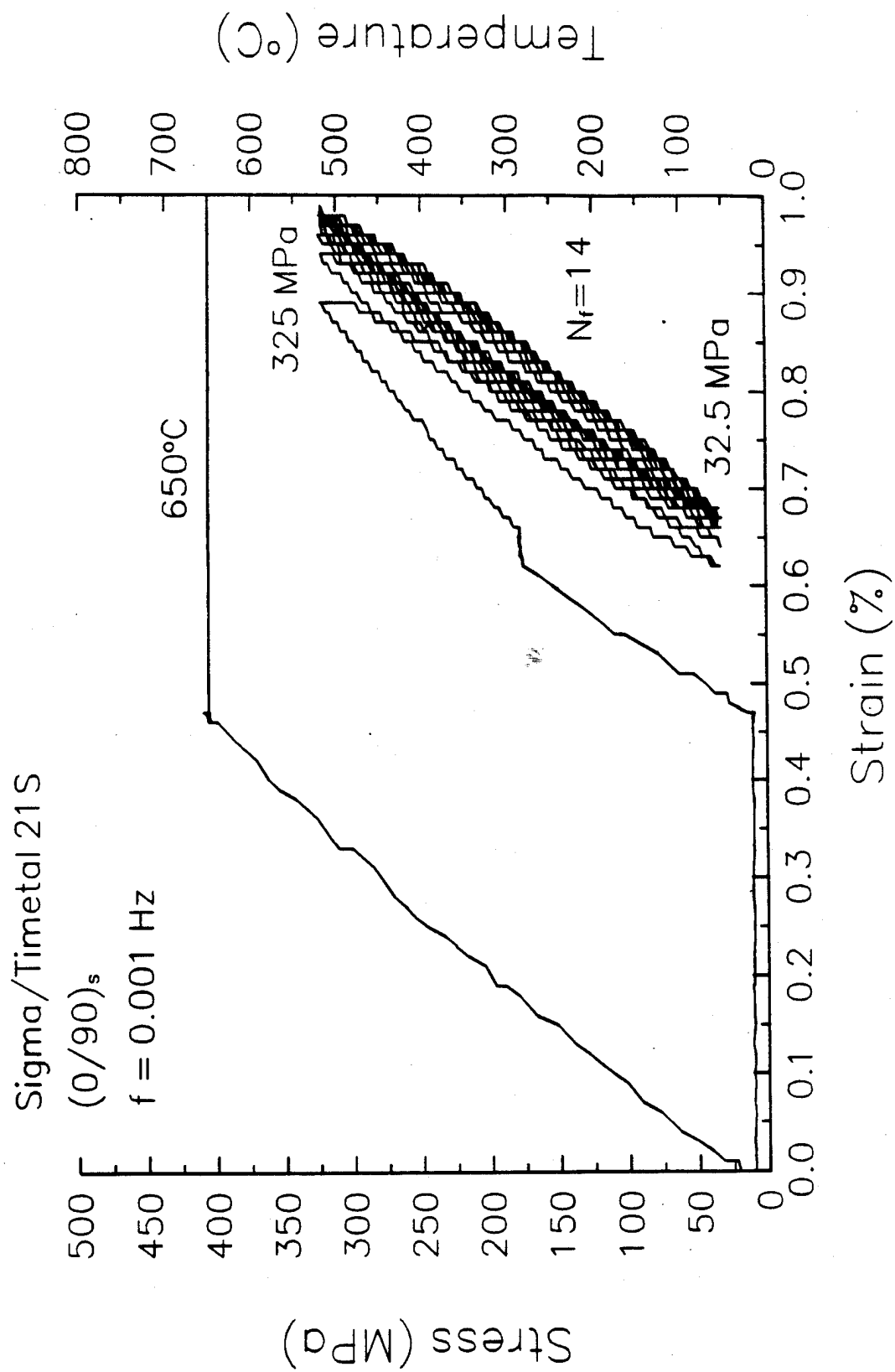


Figure 17. Stress-axial strain response measured for a  $(0/90)_s$  Sigma/Timetal 21S laminate under the slow load cycles shown in inset of Fig. 15

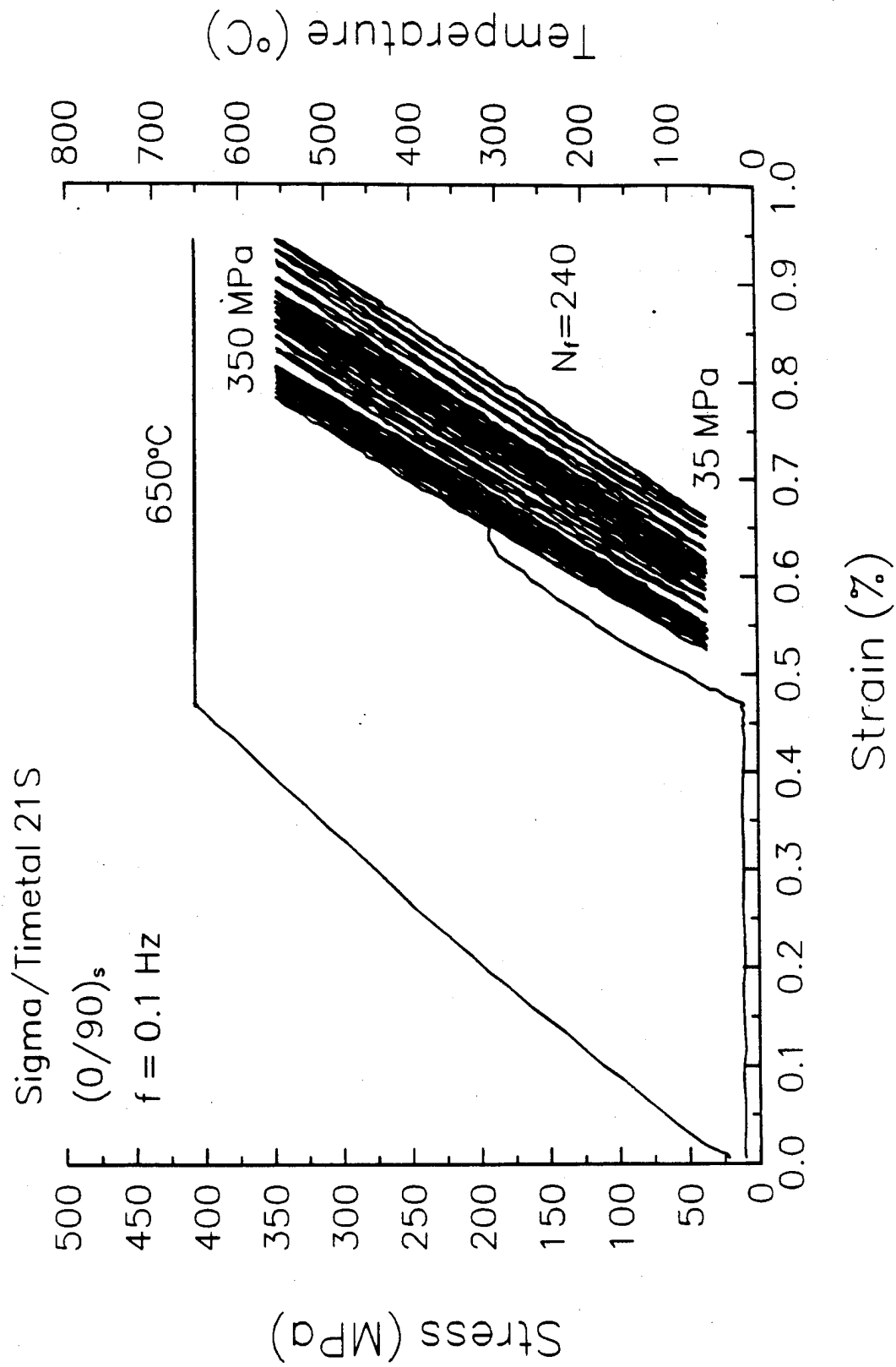


Figure 18. Stress-axial strain response measured for a (0/90)<sub>s</sub> Sigma/Timetal 21S laminate under the fast load cycles shown in inset of Fig. 16

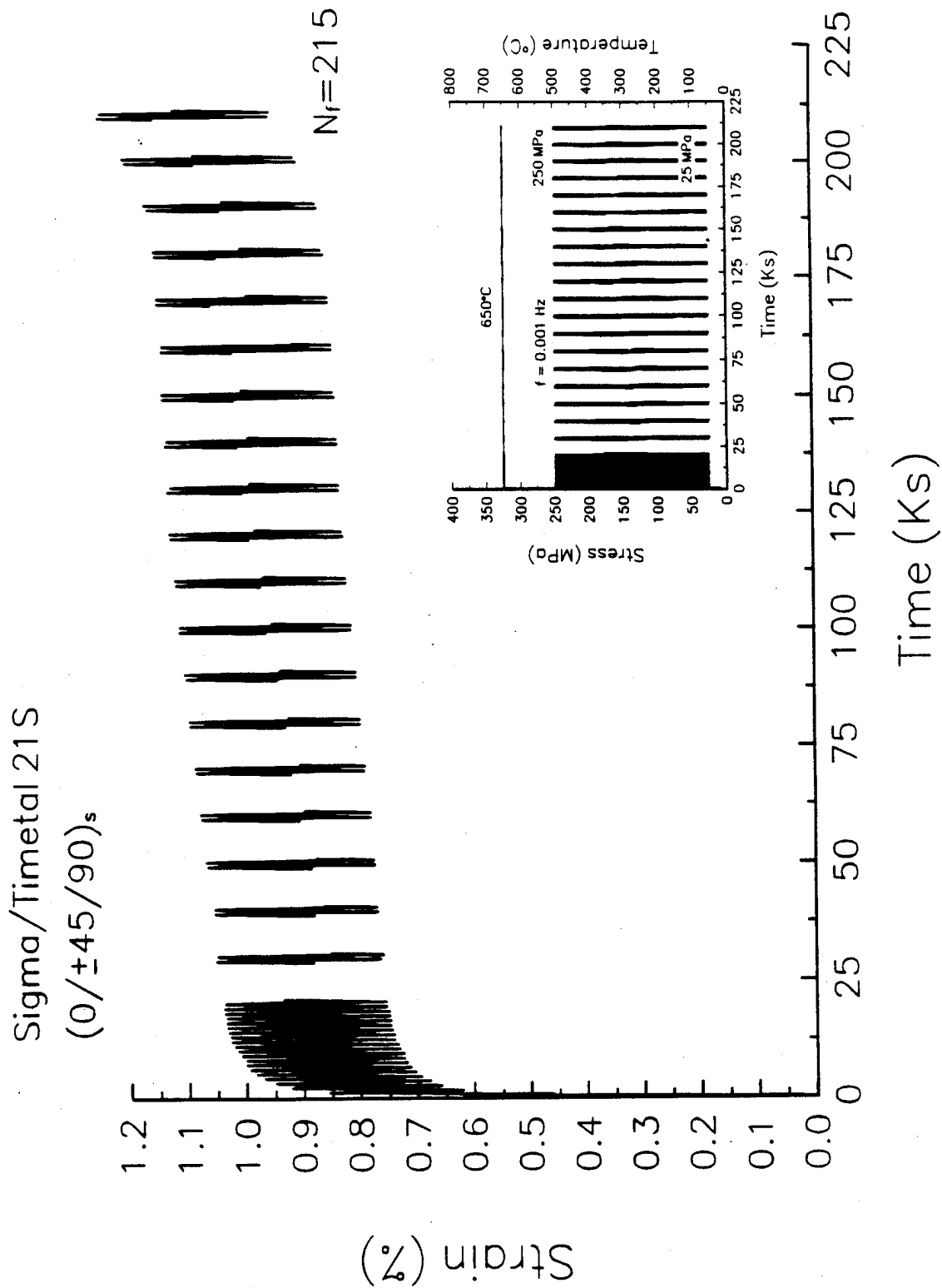


Figure 19. Total axial strain history measured for a (0/±45/90)<sub>s</sub> Sigma/Timetal 21S laminate at 650°C under the slow load cycles shown in inset

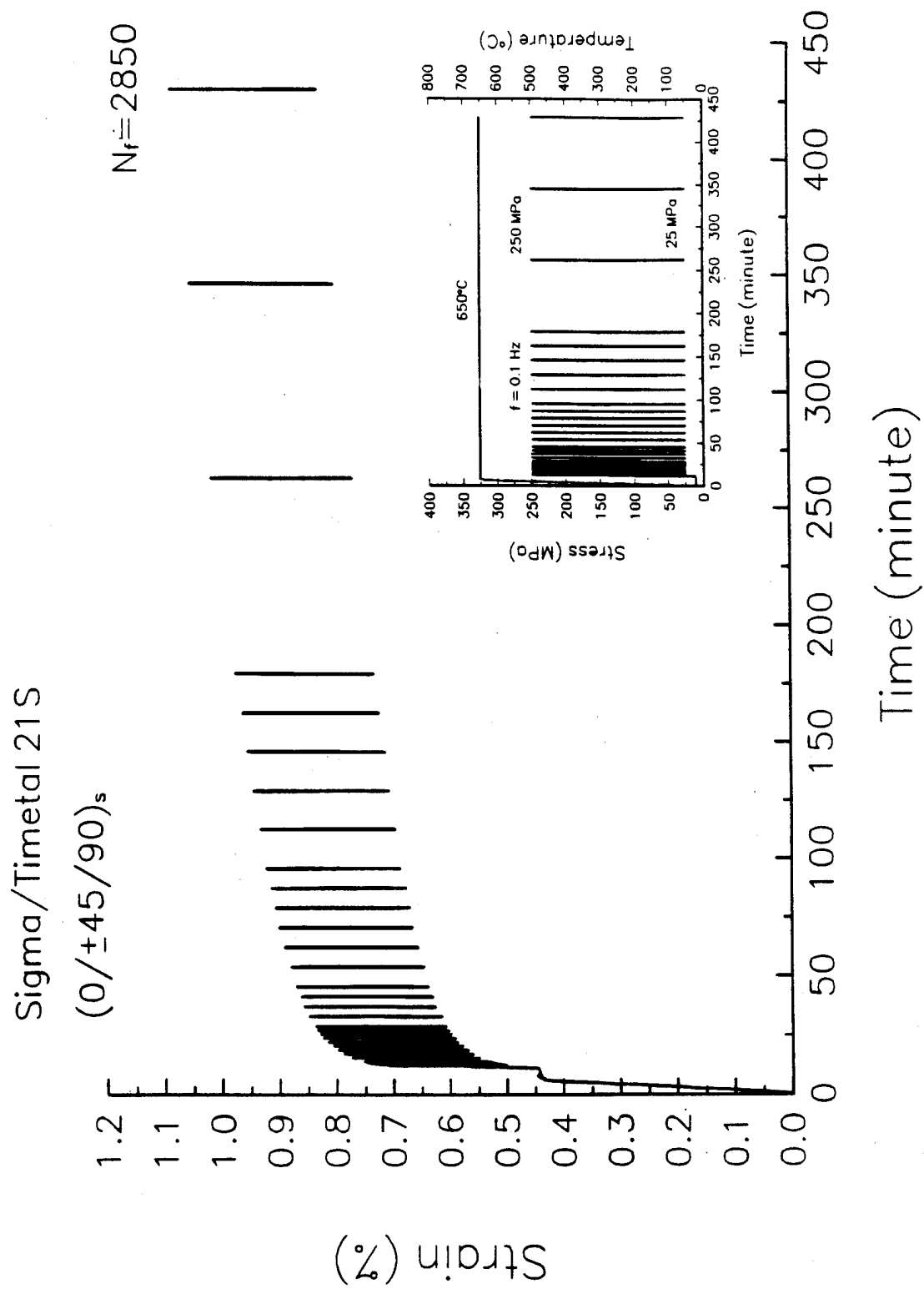


Figure 20. Total axial strain history measured for a (0/±45/90)<sub>s</sub> Sigma/Timetal 21S laminate at 650°C under the fast load cycles shown in inset

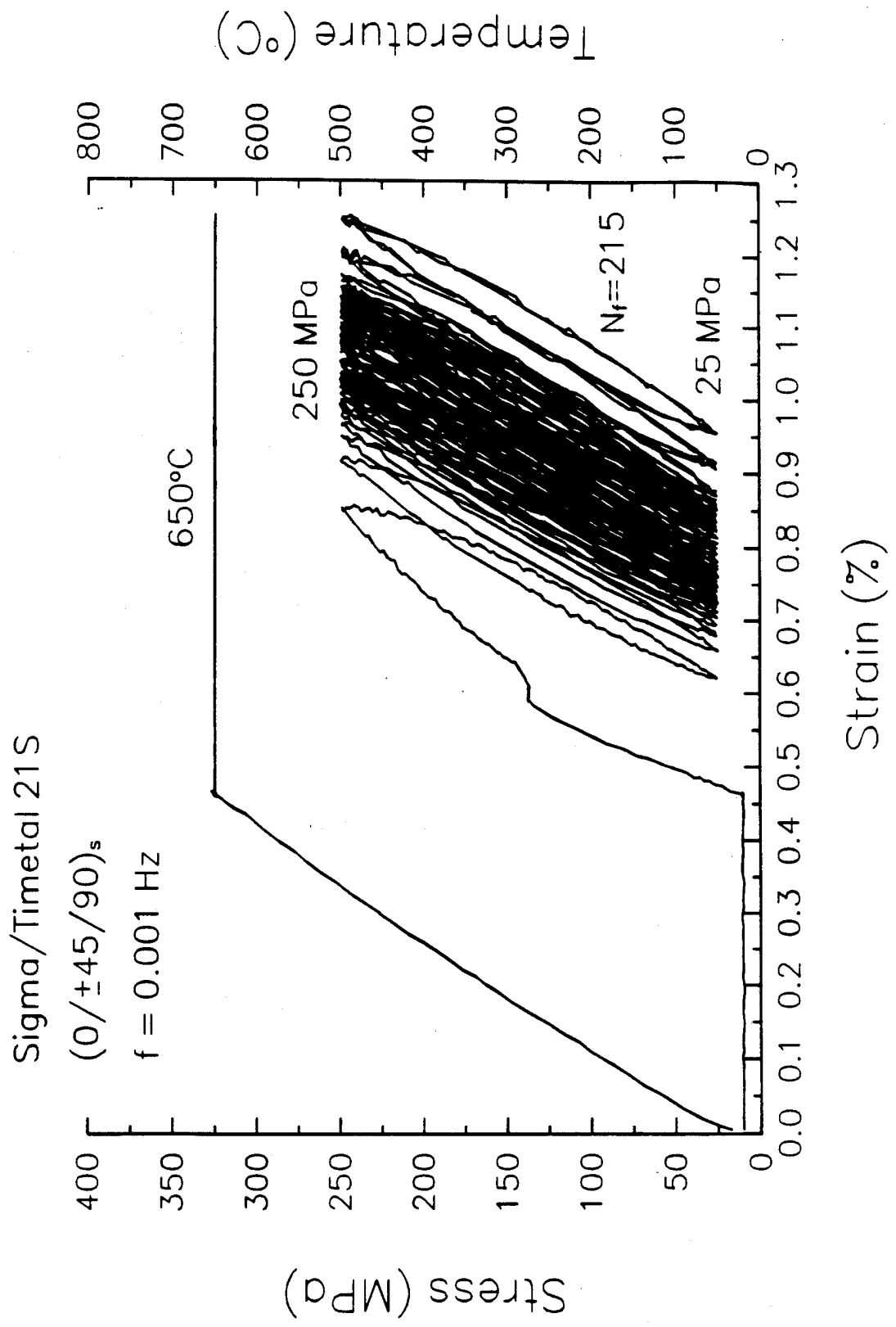


Figure 21. Stress-axial strain response measured for a (0/±45/90)<sub>s</sub> Sigma/Timetal 21S laminate under the slow load cycles shown in inset of Fig. 19

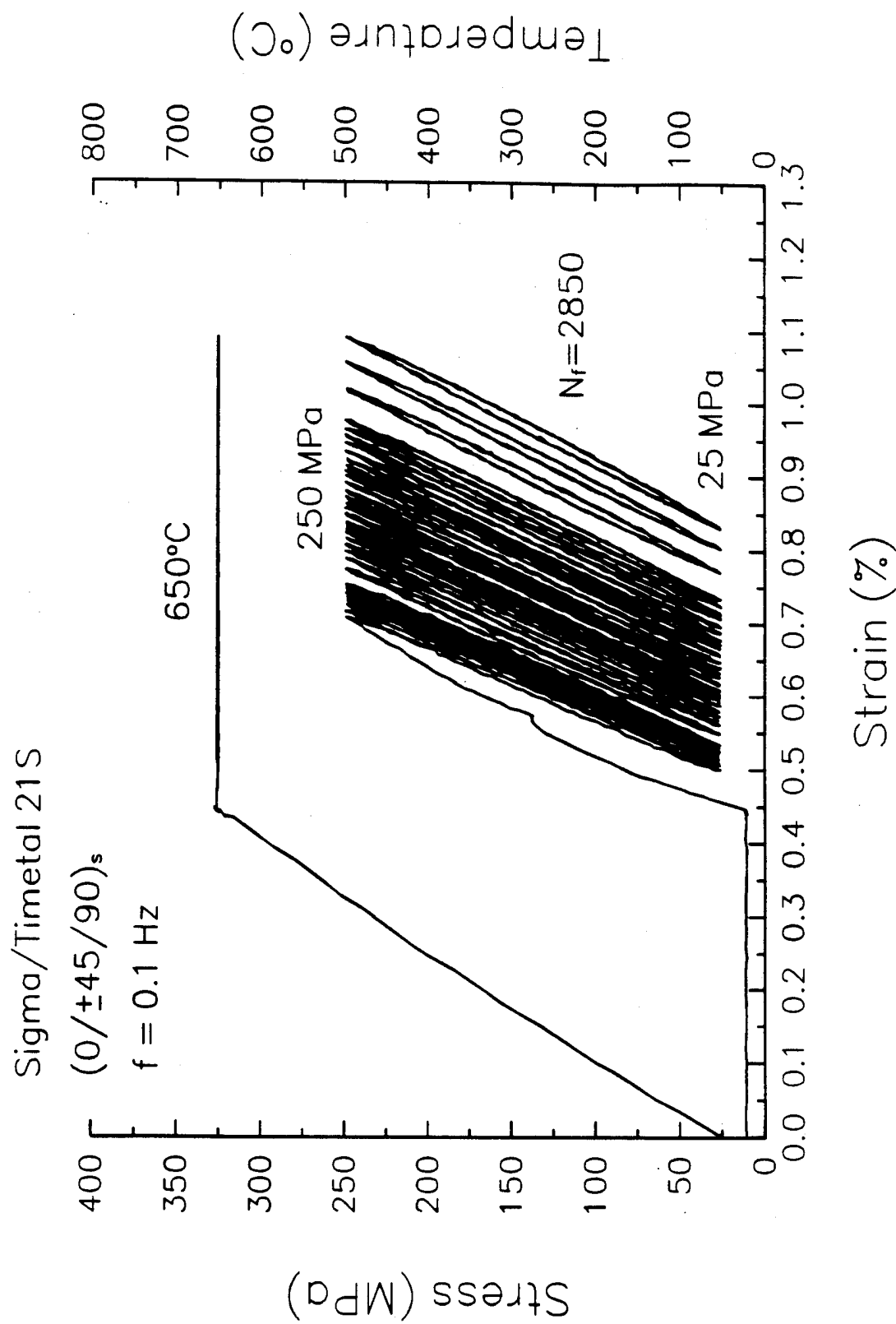


Figure 22. Stress-axial strain response measured for a  $(0/\pm 45/90)_s$  Sigma/Timetal 21S laminate under the fast load cycles shown in inset of Fig. 20



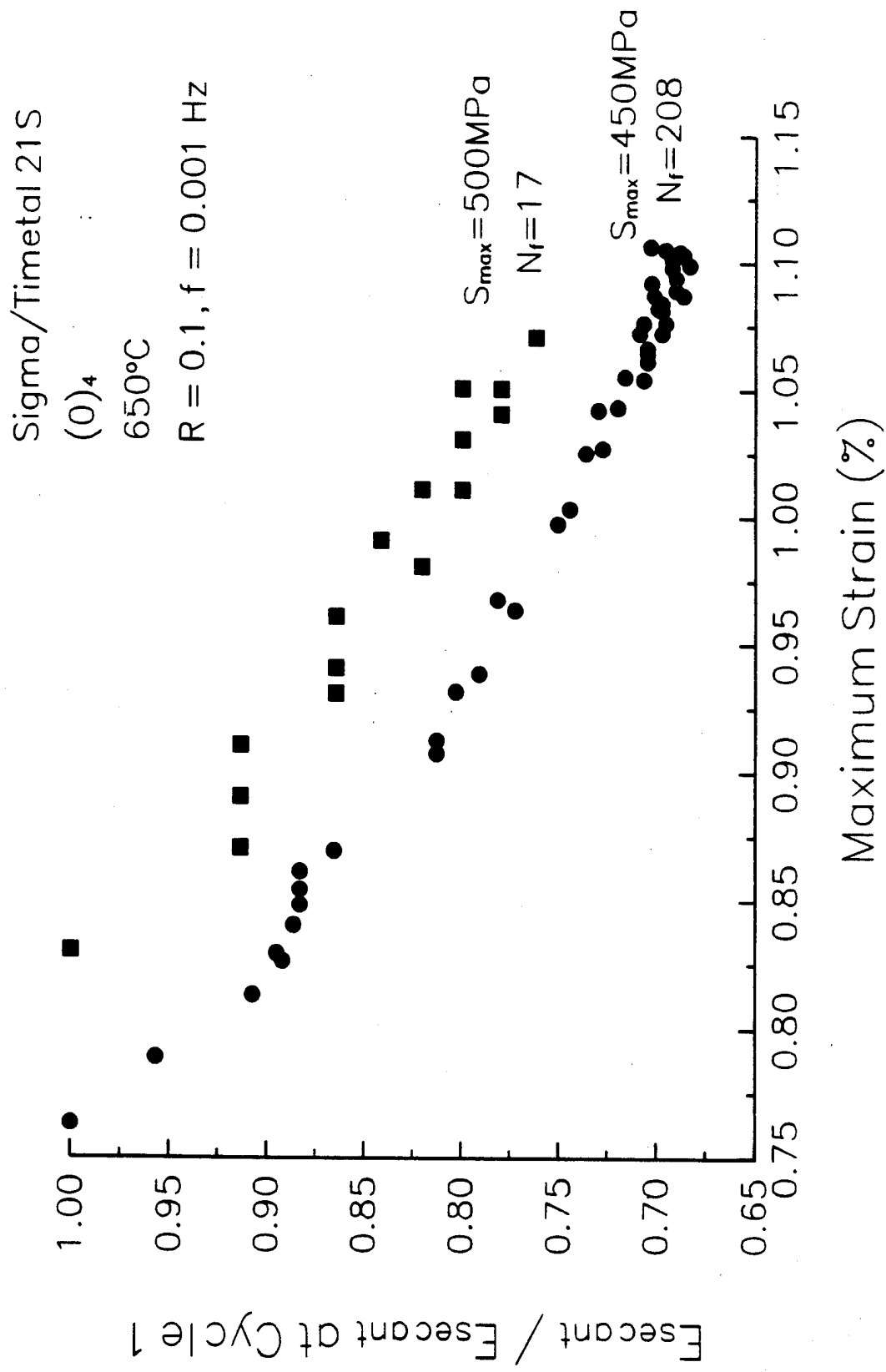


Figure 24. Variation of secant modulus measured in two (0)<sub>4</sub> Sigma/Timetal 21S laminates subjected to cyclic loading at 650°C



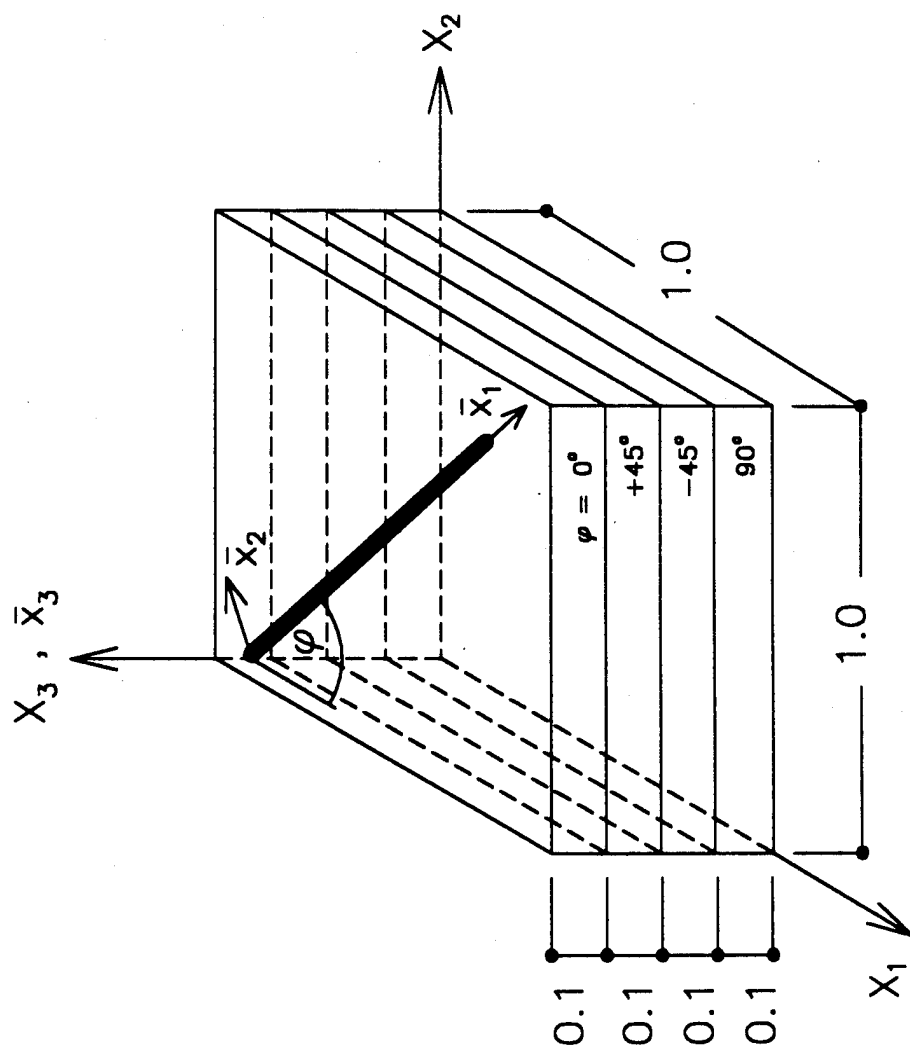


Figure 26 Finite element model of a  $(0/\pm 45/90)_s$  laminate

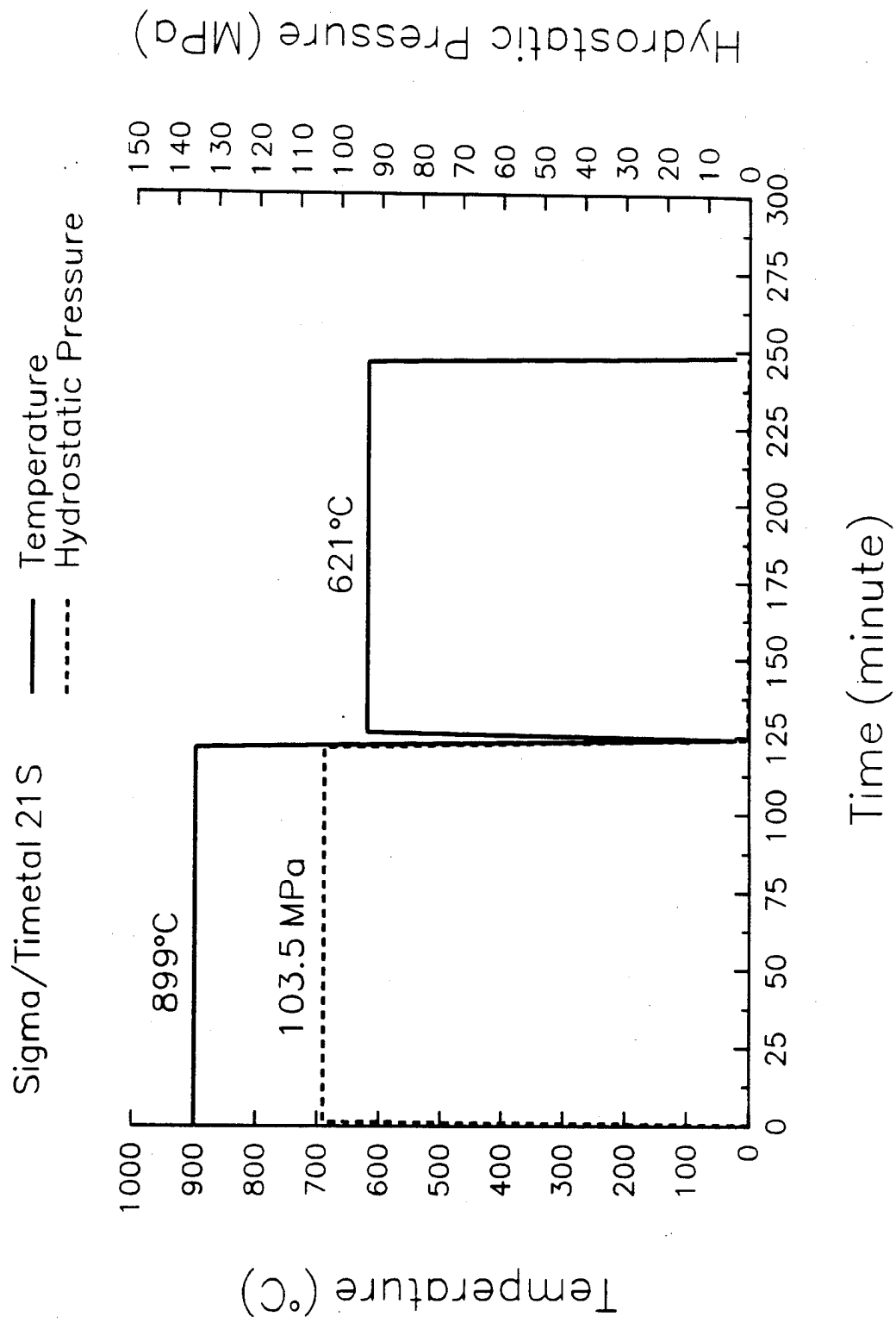


Figure 27 Thermomechanical loading applied to Sigma/Timetal 21S laminates in fabrication by hot isostatic pressing and cooling

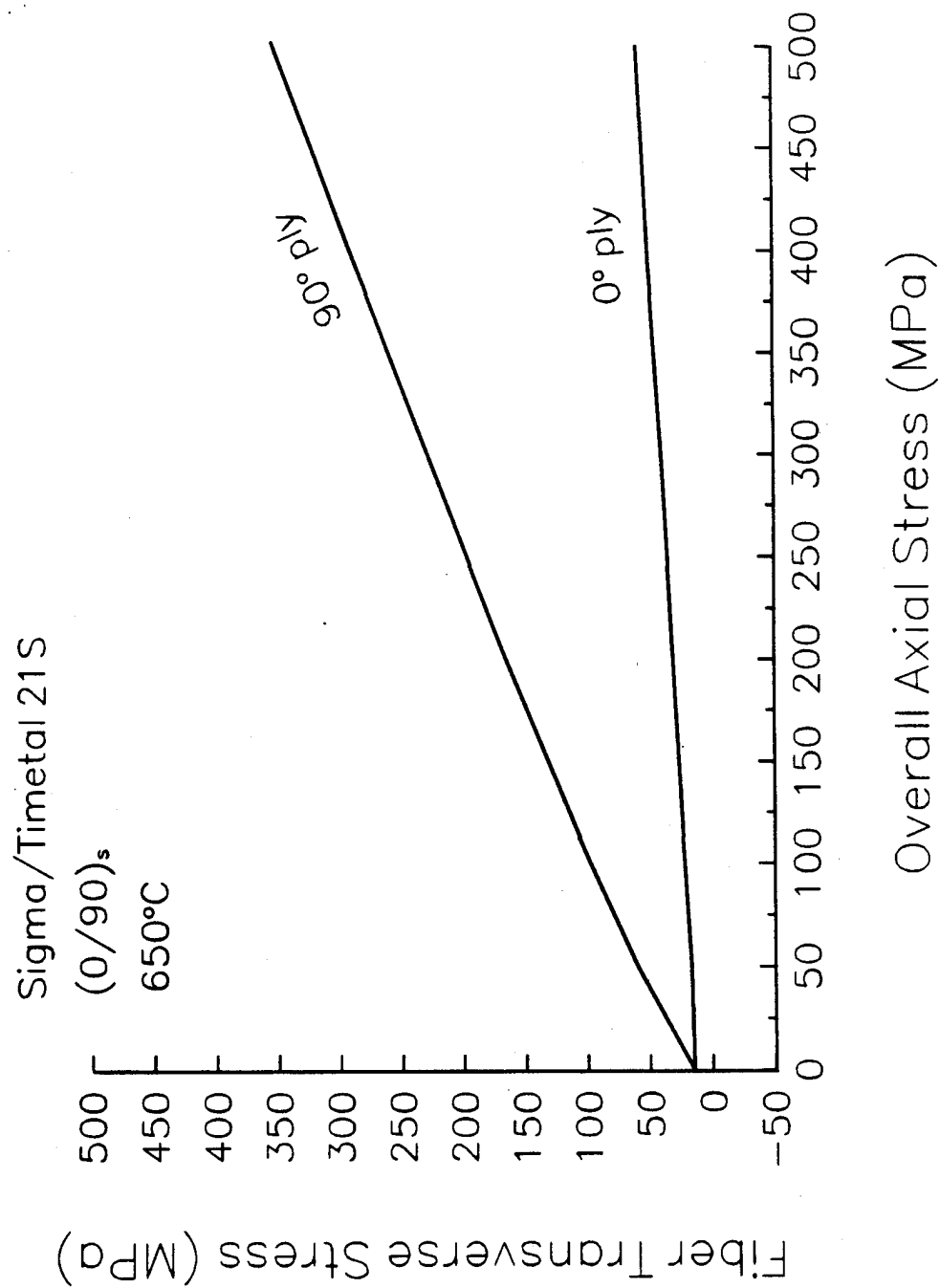


Figure 28 Variation of the transverse normal stress in fully bonded fibers of a Sigma/Timetal 21S (0/90)<sub>s</sub> laminate with the overall axial stress

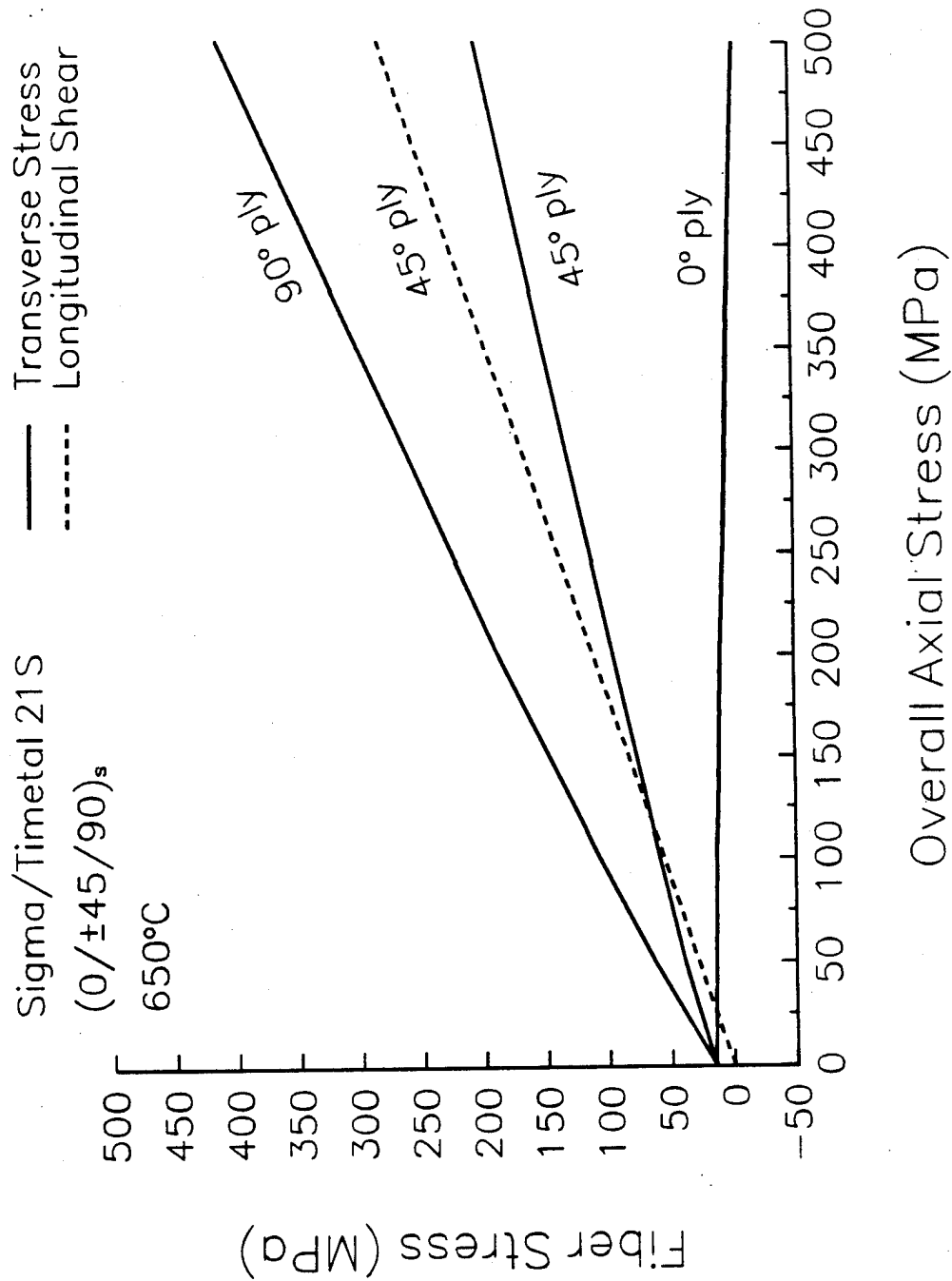


Figure 29 Variation of the transverse normal stress, and longitudinal shear stress in fully banded fibers of a Sigma/Timetal 21S (0/±45/90)<sub>s</sub> laminate with the overall axial stress

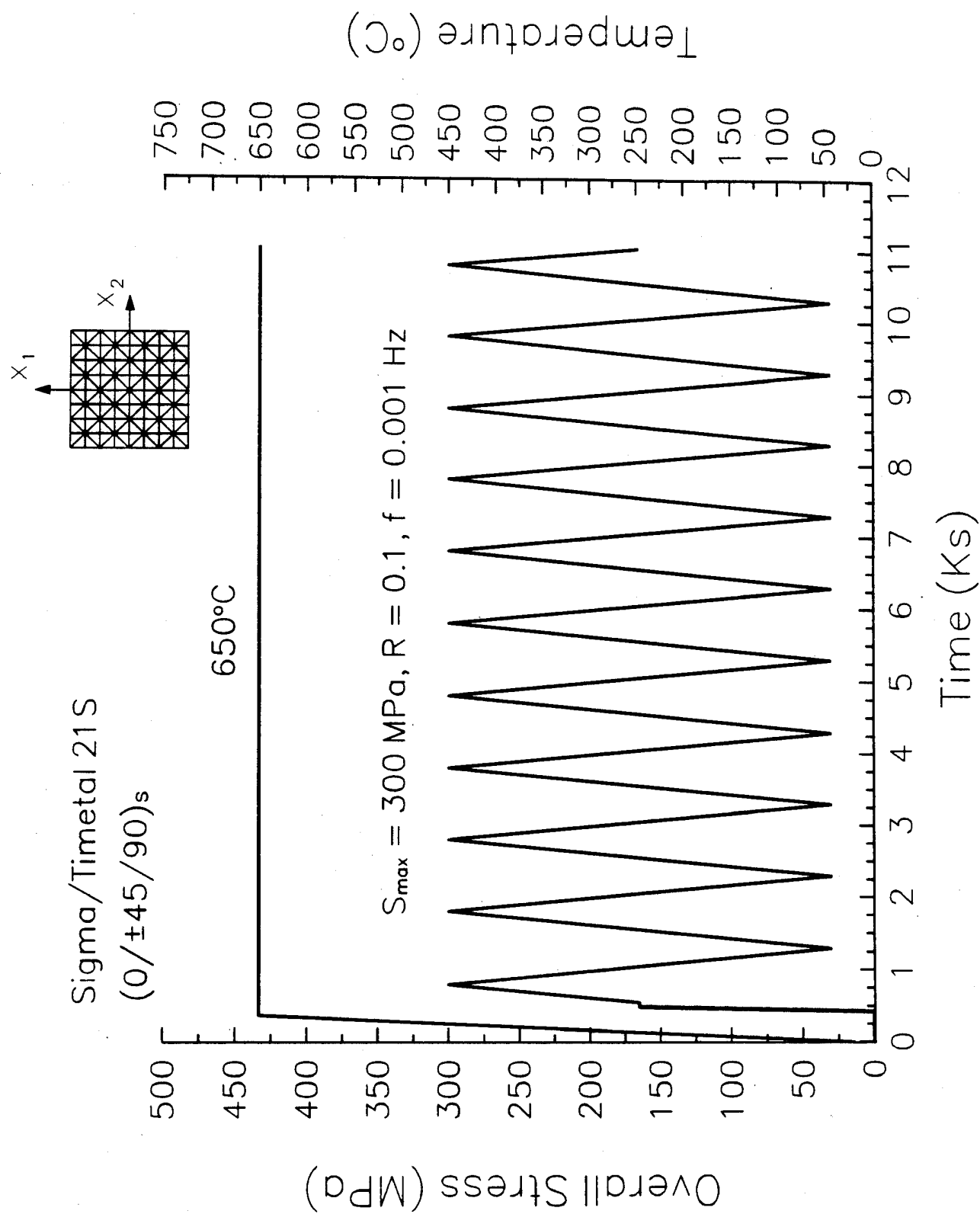


Figure 30 Isothermal cyclic loading applied to a Sigma/Timetal 21S (0/±45/90)<sub>s</sub> laminate

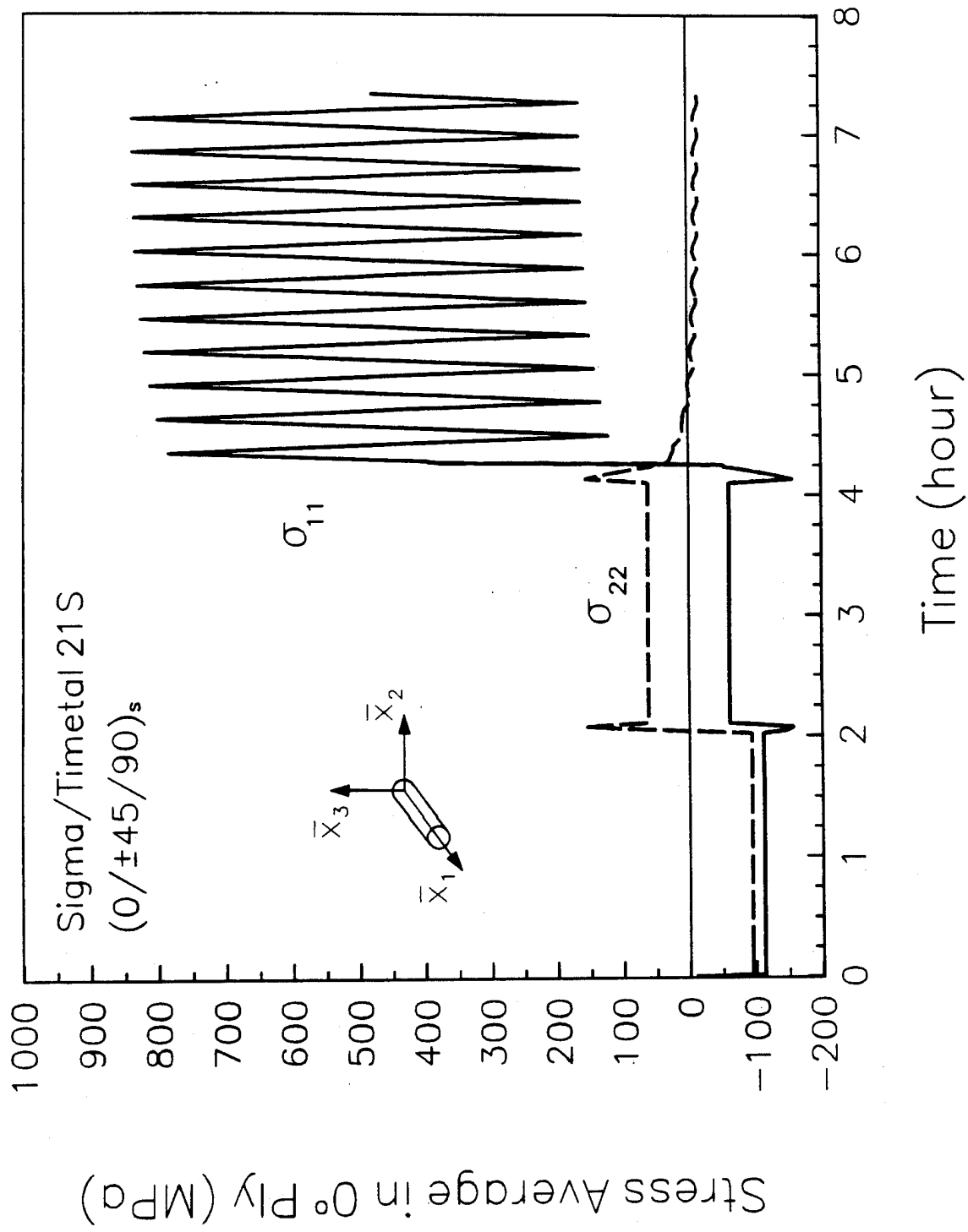


Figure 31 Stress average computed in the 0° ply of a Sigma/Timetal 21S (0/±45/90)<sub>s</sub> laminate subjected to HIP and isothermal cyclic loading

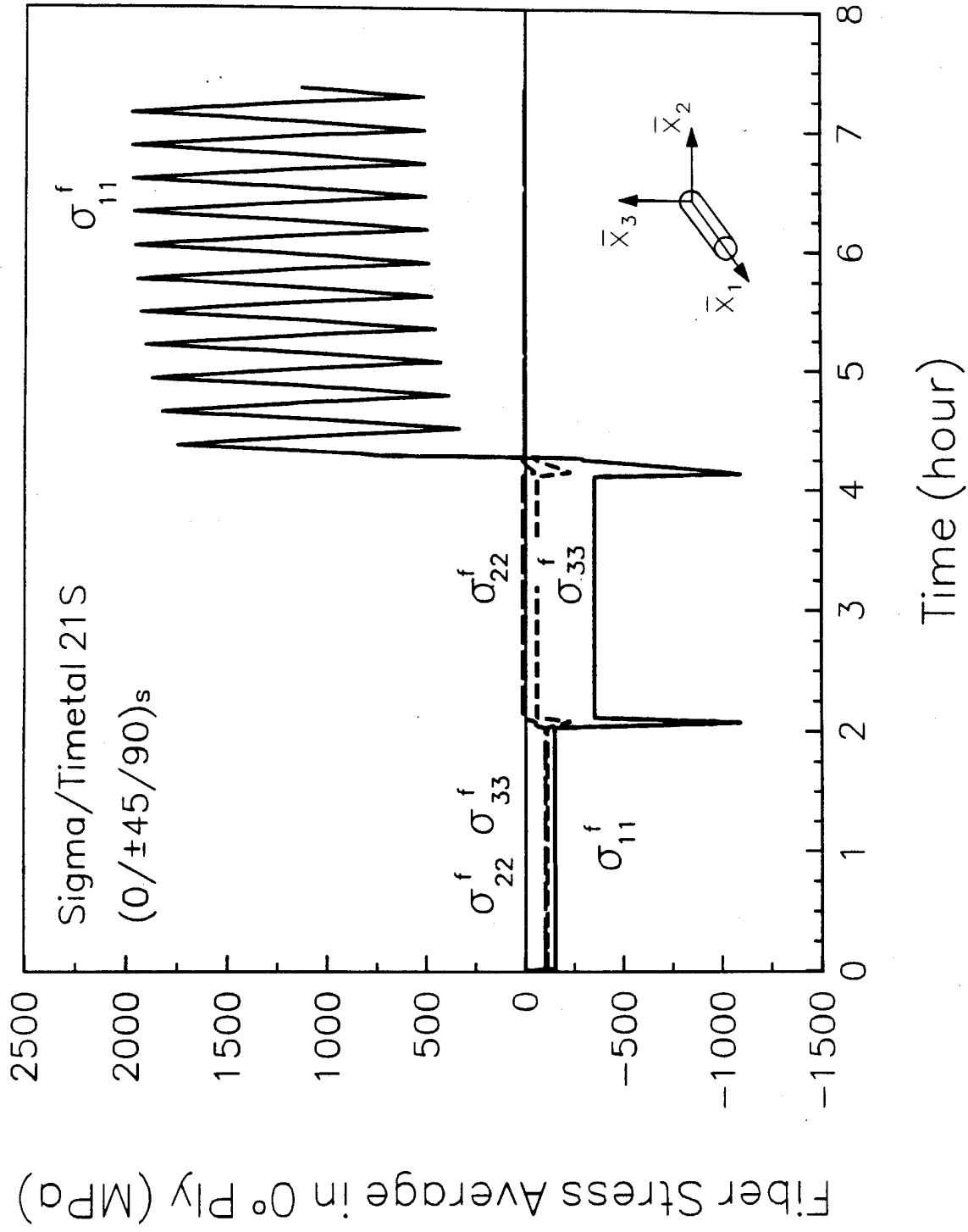


Figure 32 Fiber stress average computed in the 0° ply of a Sigma/Timetal 21S (0/±45/90)<sub>s</sub> laminate subjected to HIP and isothermal cyclic loading

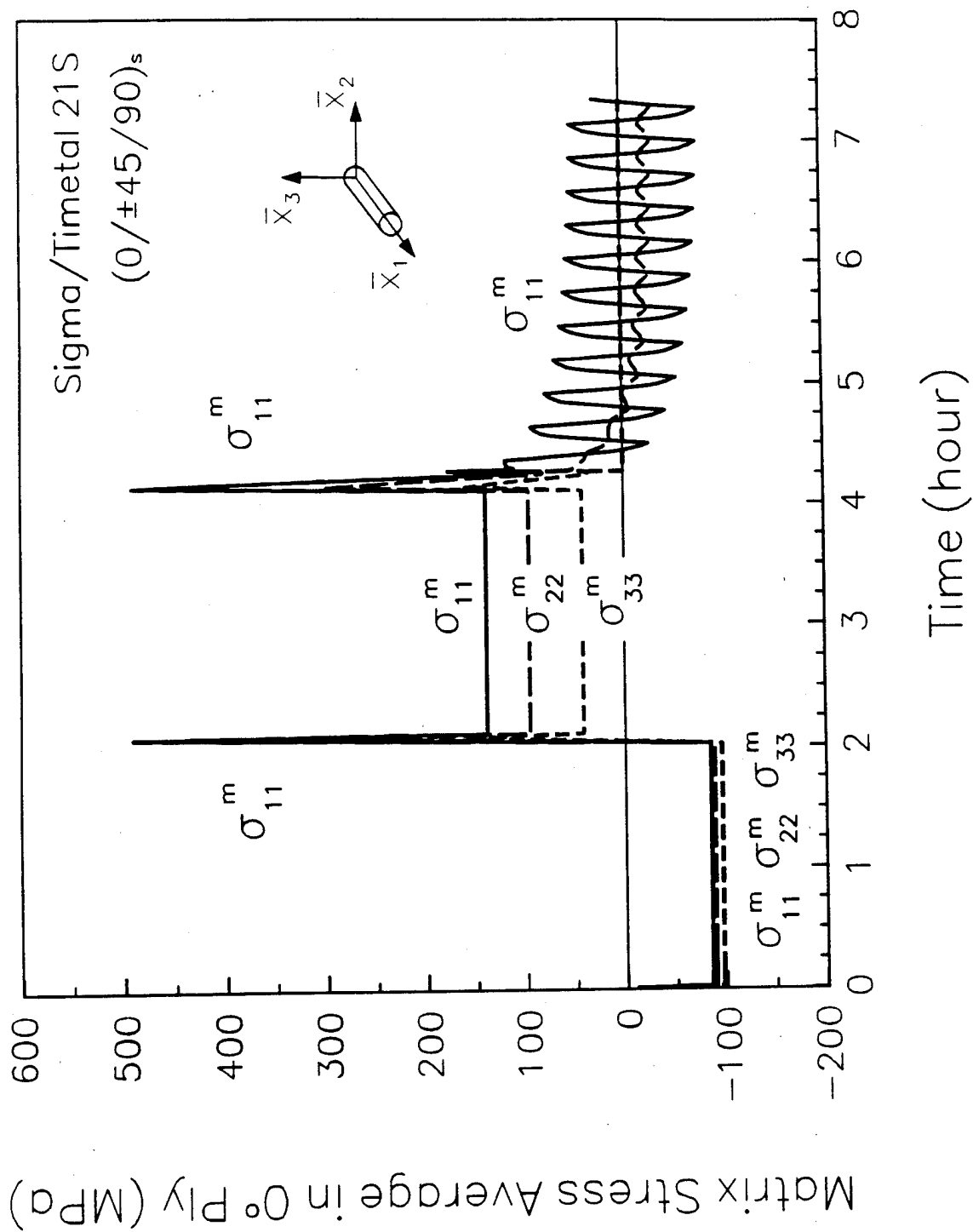


Figure 33 Matrix stress average computed in the 0° ply of a Sigma/Timetal 21S (0/±45/90)<sub>s</sub> laminate subjected to HIP and isothermal cyclic loading

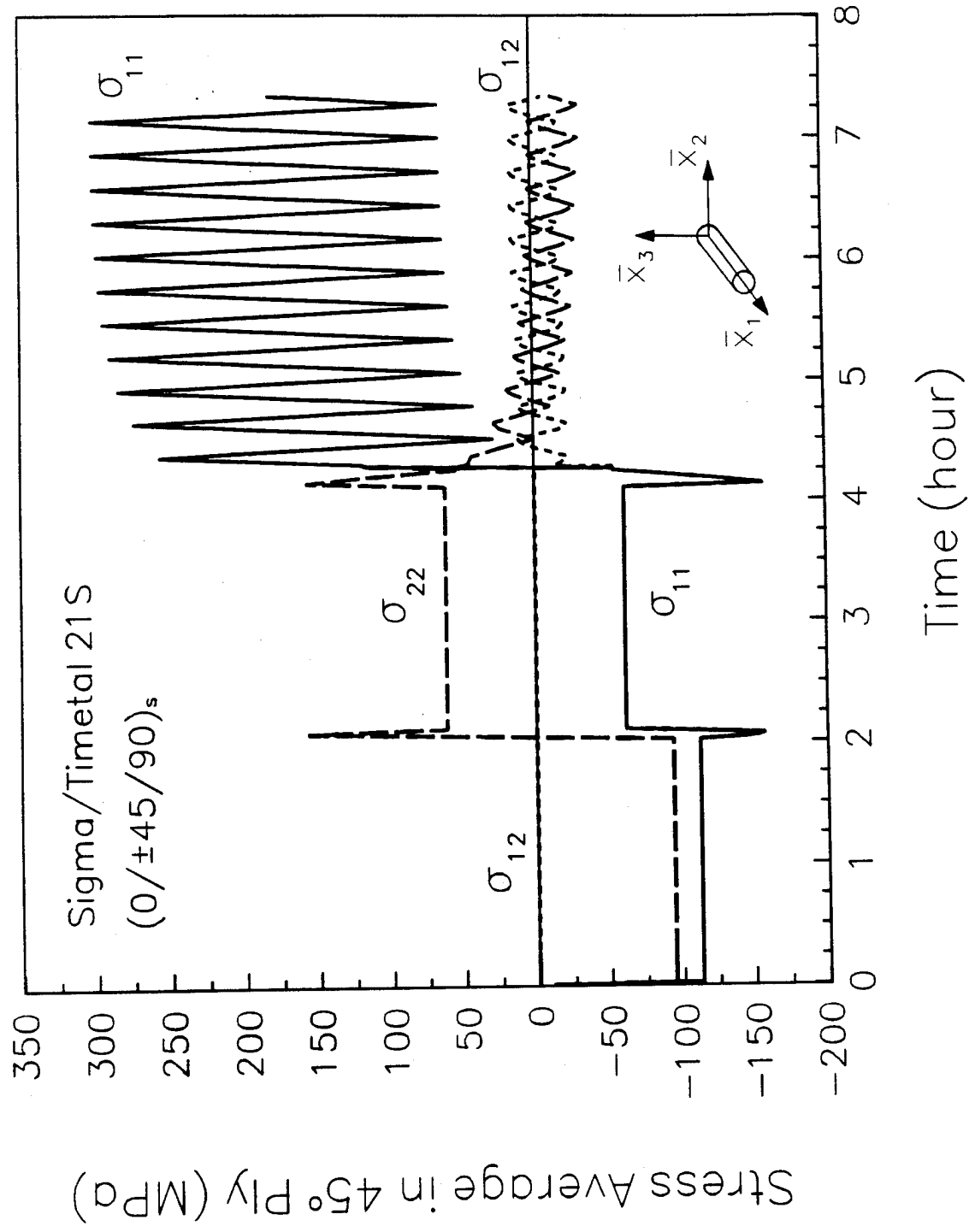


Figure 34 Stress average computed in the 45° ply of a Sigma/Timetal 21S (0/±45/90)<sub>s</sub> laminate subjected to HIP and isothermal cyclic loading

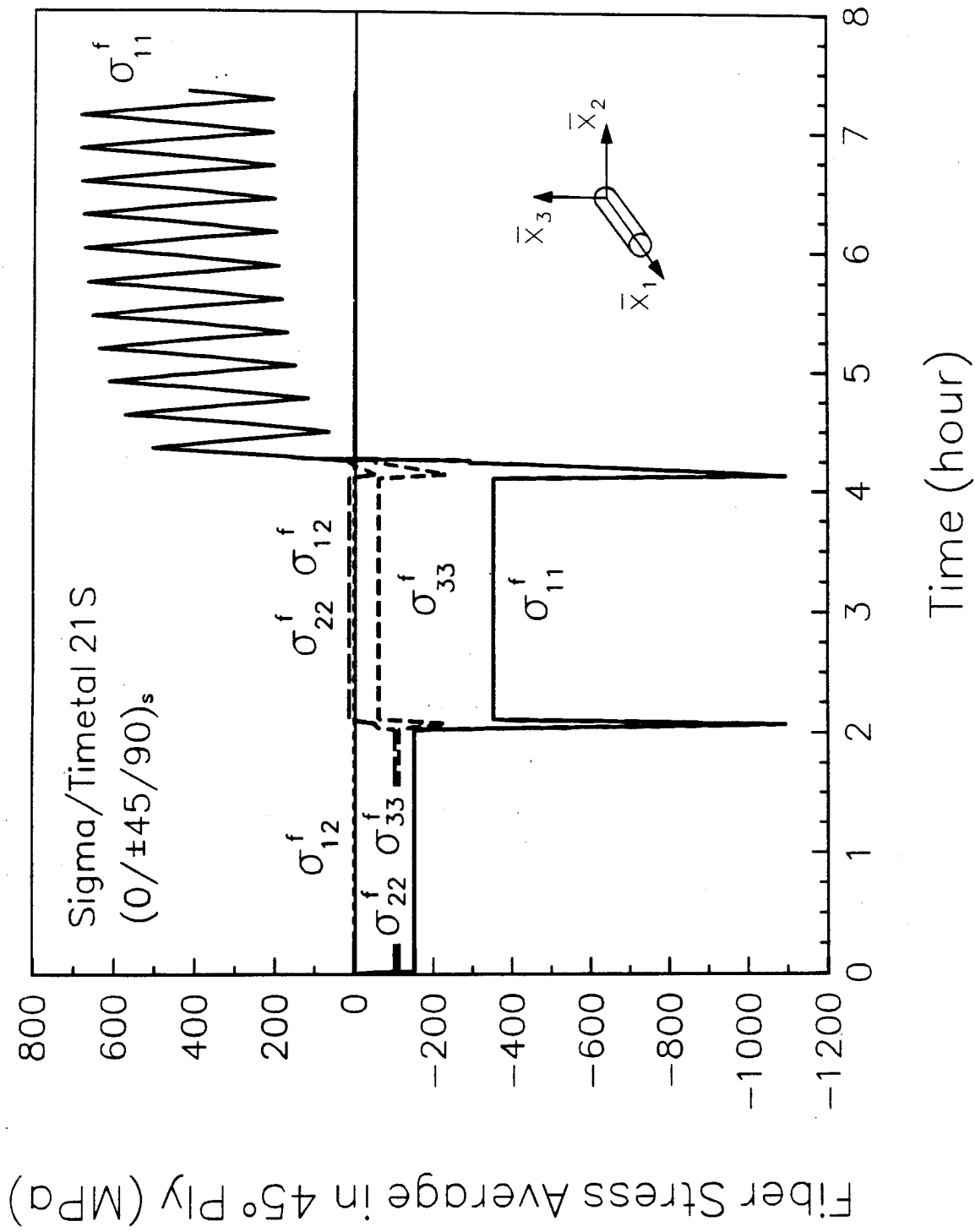


Figure 35 Fiber stress average computed in the 45° ply of a Sigma/Timetal 21S (0/±45/90)<sub>s</sub> laminate subjected to HIP and isothermal cyclic loading

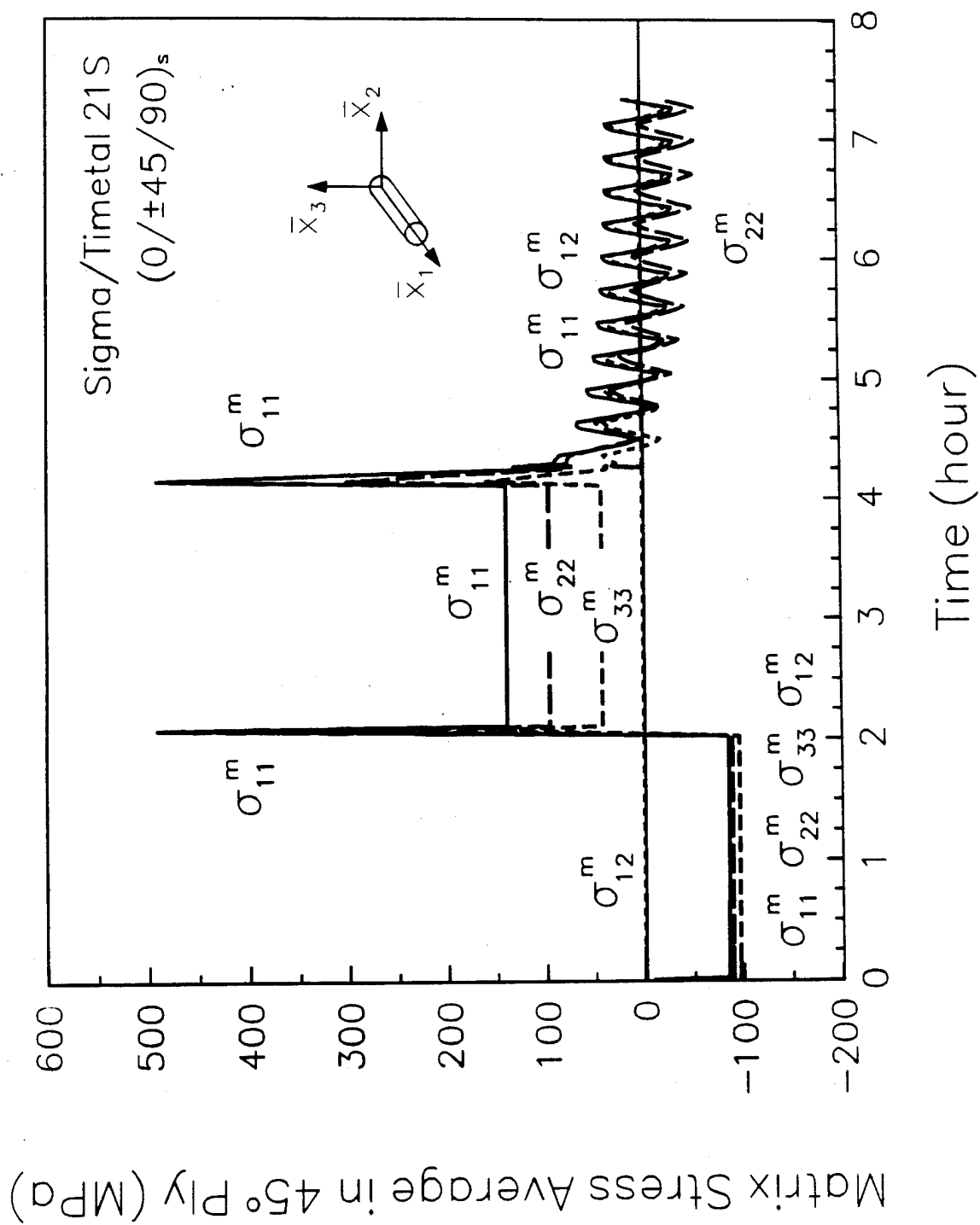


Figure 36 Matrix stress average computed in the 45° ply of a Sigma/Timetal 21S (0/±45/90)<sub>s</sub> laminate subjected to HIP and isothermal cyclic loading

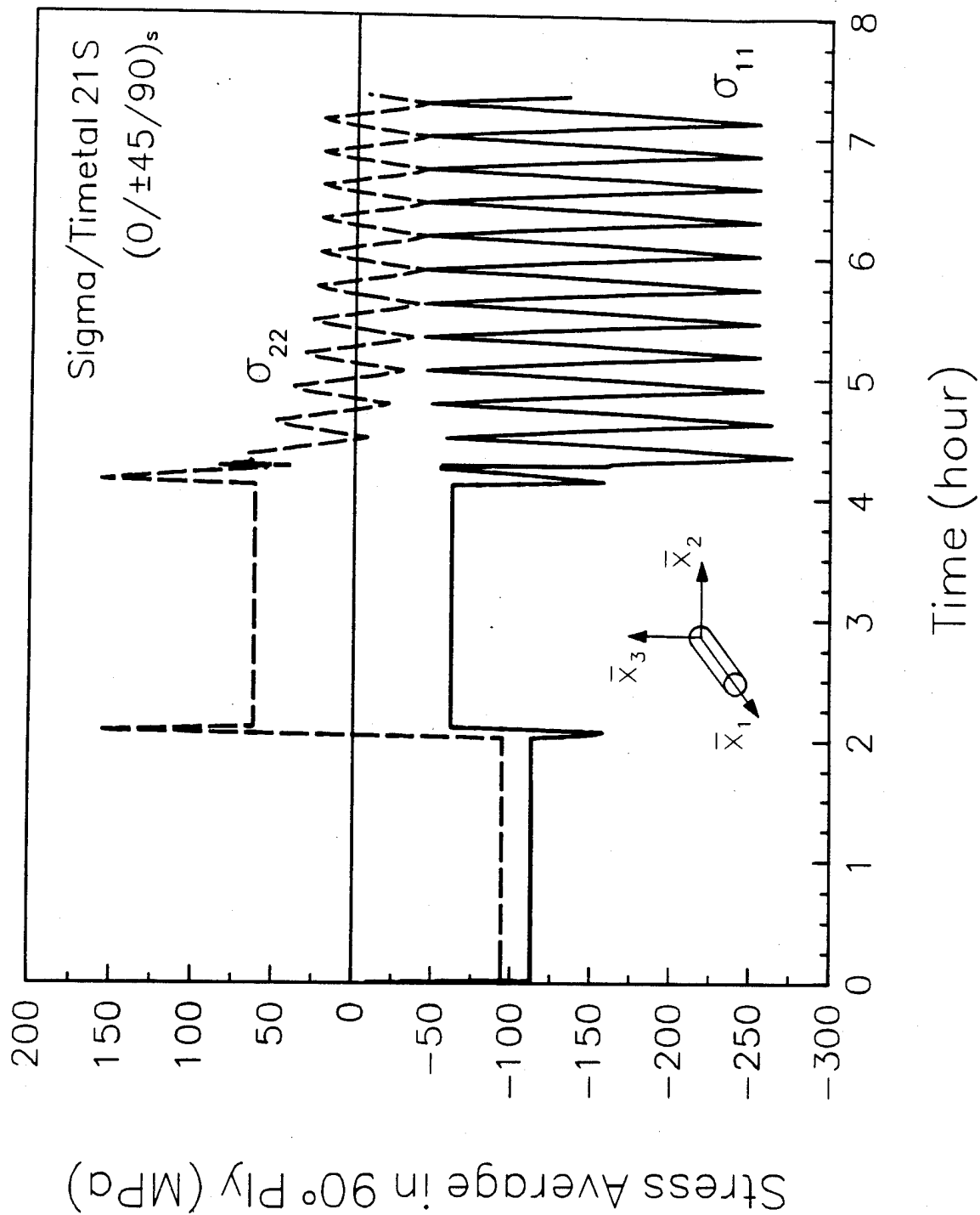


Figure 37 Stress average computed in the 90° ply of a Sigma/Timetal 21S (0/±45/90)<sub>s</sub> laminate subjected to HIP and isothermal cyclic loading

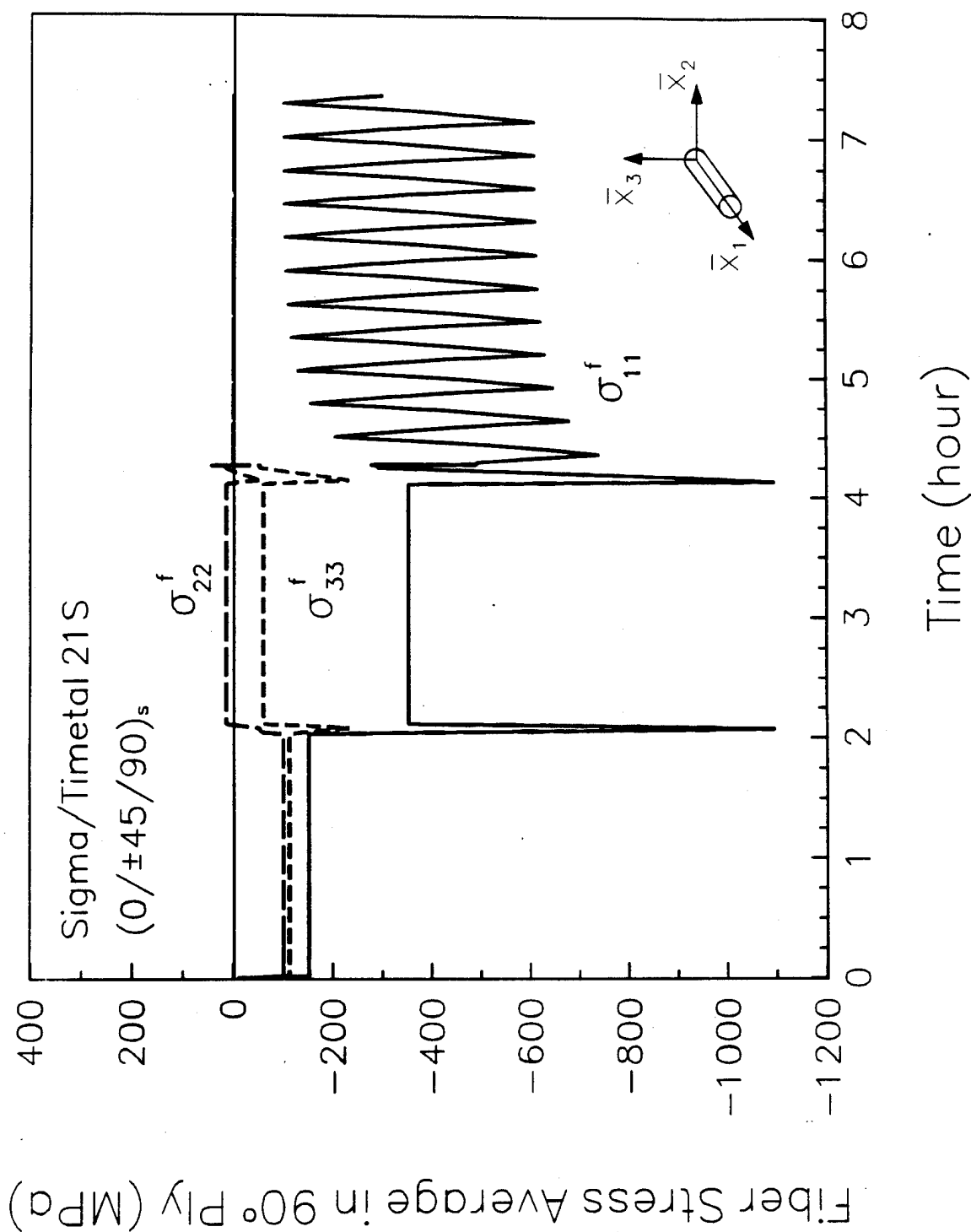


Figure 38 Fiber stress average computed in the 90° ply of a Sigma/Timetal 21S (0/±45/90)<sub>s</sub> laminate subjected to HIP and isothermal cyclic loading.

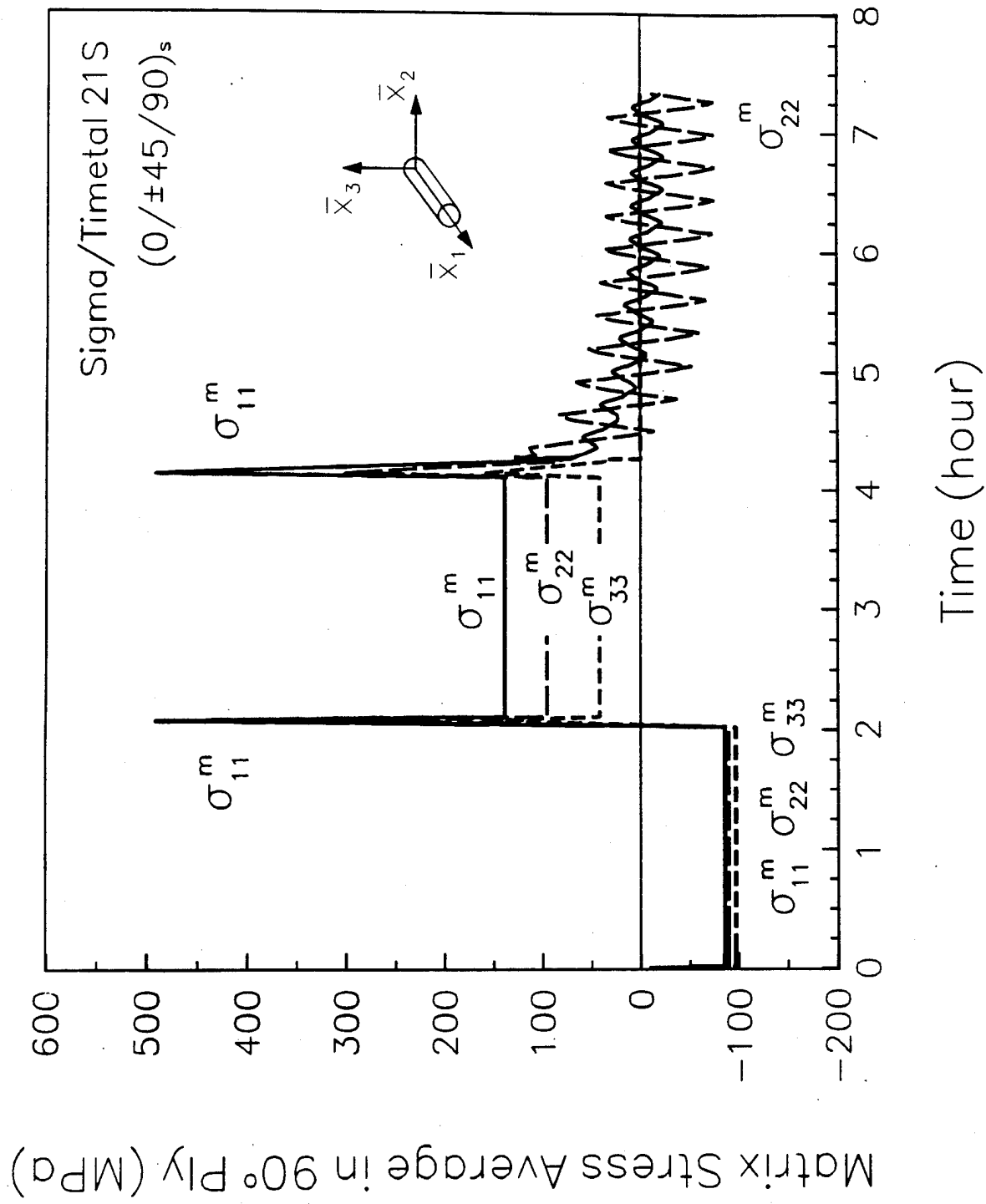
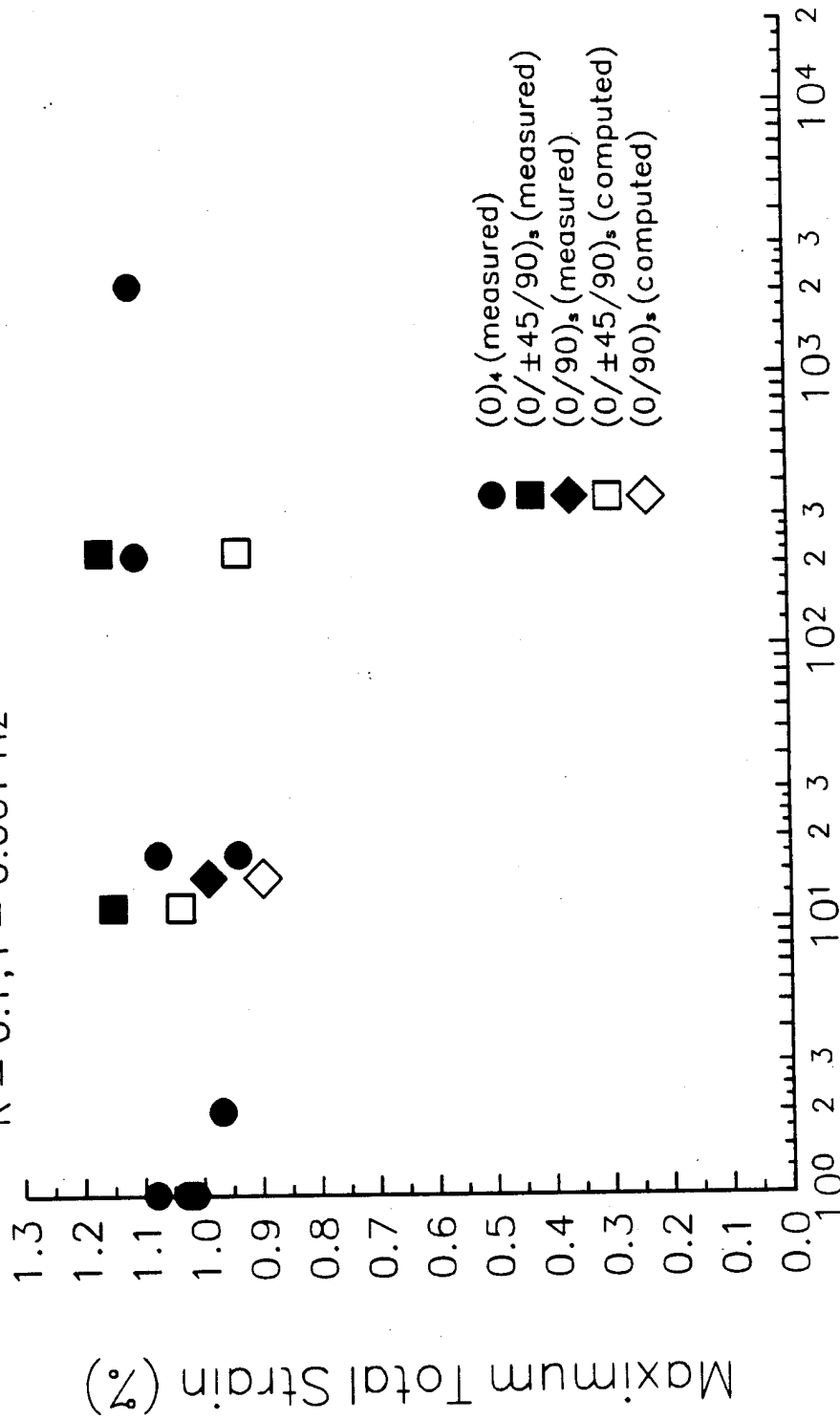


Figure 39 Matrix stress average computed in the 90° ply of a Sigma/Timetal 21S (0/±45/90)<sub>s</sub> laminate subjected to HIP and isothermal cyclic loading

Sigma/Timetal 21S

650°C

$R = 0.1, f = 0.001 \text{ Hz}$



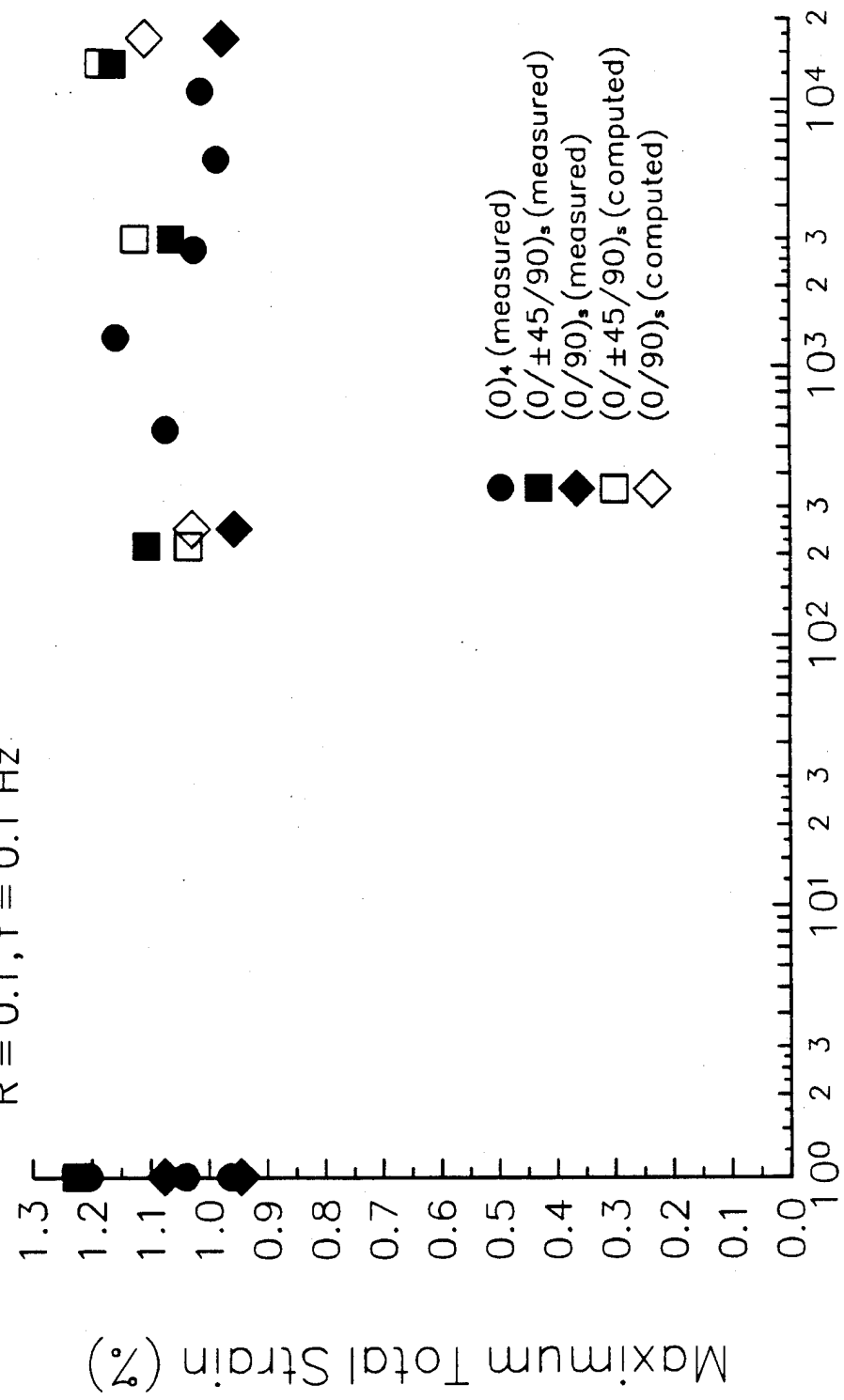
Number of Cycles at Failure

Figure 40 Measured and computed maximum overall axial strains in Sigma/Timetal 21S laminates under isothermal fatigue loading conditions shown in Table 2 for the slow cycle at 0.001 Hz

Sigma/Timetal 21S

650°C

R = 0.1, f = 0.1 Hz



Number of Cycles at Failure

Figure 41 Measured and computed maximum overall axial strains in Sigma/Timetal 21S laminates under isothermal fatigue loading conditions

# REPORT DOCUMENTATION PAGE

Form Approved  
OMB No. 0704-0188

Public reporting burden for this collection of information is estimated to average 1 hour per response, including the time for reviewing instructions, searching existing data sources, gathering and maintaining the data needed, and completing and reviewing the collection of information. Send comments regarding this burden estimate or any other aspect of this collection of information, including suggestions for reducing this burden, to Washington Headquarters Services, Directorate for Information Operations and Reports, 1215 Jefferson Davis Highway, Suite 1204, Arlington, VA 22202-4302, and to the Office of Management and Budget, Paperwork Reduction Project (0704-0188), Washington, DC 20503.

1. AGENCY USE ONLY (Leave blank)		2. REPORT DATE September 14, 1995		3. REPORT TYPE AND DATES COVERED Final Technical Report	
4. TITLE AND SUBTITLE Static and Fatigue Damage in High Temperature Composites (1A)				5. FUNDING NUMBERS F-4962092-J-0391	
6. AUTHOR(S) G. J. Dvorak and Y.A. Bahei-El-Din					
7. PERFORMING ORGANIZATION NAME(S) AND ADDRESS(ES) Department of Civil Engineering and Center for Composite Materials and Structures Rensselaer Polytechnic Institute Troy, NY 12180-3500				8. PERFORMING ORGANIZATION REPORT NUMBER	
9. SPONSORING/MONITORING AGENCY NAME(S) AND ADDRESS(ES) Dr. Walter Jones Air Force Office of Scientific Research 110 Duncan Ave., Suite B115 Bolling Air Force Base, Washington, D.C.				10. SPONSORING/MONITORING AGENCY REPORT NUMBER	
11. SUPPLEMENTARY NOTES					
12a. DISTRIBUTION/AVAILABILITY STATEMENT unlimited				12b. DISTRIBUTION CODE	
13. ABSTRACT (Maximum 200 words) This final report presents the experimental and theoretical work performed in our research program on static and fatigue damage in high temperature composites. The theoretical part focused on development and implementation of a new Transformation Field Analysis (TFA) for inelastic laminates, which employs unit-cell, periodic array models, as well as averaging micromechanical models together with any constitutive law for thermo-viscoplastic and other inelastic deformation. Moreover, we have initiated modeling of damage by debonding and frictional sliding at the fiber interface, using the TFA computational scheme and the finite element method.					
14. SUBJECT TERMS Static, fatigue damage, high temperature composites				15. NUMBER OF PAGES 92	
				16. PRICE CODE	
17. SECURITY CLASSIFICATION OF REPORT unclassified	18. SECURITY CLASSIFICATION OF THIS PAGE unclassified	19. SECURITY CLASSIFICATION OF ABSTRACT unclassified	20. LIMITATION OF ABSTRACT		

## GENERAL INSTRUCTIONS FOR COMPLETING SF 298

The Report Documentation Page (RDP) is used in announcing and cataloging reports. It is important that this information be consistent with the rest of the report, particularly the cover and title page. Instructions for filling in each block of the form follow. It is important to stay *within the lines* to meet optical scanning requirements.

**Block 1. Agency Use Only (Leave blank).**

**Block 2. Report Date.** Full publication date including day, month, and year, if available (e.g. 1 Jan 88). Must cite at least the year.

**Block 3. Type of Report and Dates Covered.** State whether report is interim, final, etc. If applicable, enter inclusive report dates (e.g. 10 Jun 87 - 30 Jun 88).

**Block 4. Title and Subtitle.** A title is taken from the part of the report that provides the most meaningful and complete information. When a report is prepared in more than one volume, repeat the primary title, add volume number, and include subtitle for the specific volume. On classified documents enter the title classification in parentheses.

**Block 5. Funding Numbers.** To include contract and grant numbers; may include program element number(s), project number(s), task number(s), and work unit number(s). Use the following labels:

C - Contract	PR - Project
G - Grant	TA - Task
PE - Program Element	WU - Work Unit Accession No.

**Block 6. Author(s).** Name(s) of person(s) responsible for writing the report, performing the research, or credited with the content of the report. If editor or compiler, this should follow the name(s).

**Block 7. Performing Organization Name(s) and Address(es).** Self-explanatory.

**Block 8. Performing Organization Report Number.** Enter the unique alphanumeric report number(s) assigned by the organization performing the report.

**Block 9. Sponsoring/Monitoring Agency Name(s) and Address(es).** Self-explanatory.

**Block 10. Sponsoring/Monitoring Agency Report Number.** (If known)

**Block 11. Supplementary Notes.** Enter information not included elsewhere such as: Prepared in cooperation with...; Trans. of...; To be published in.... When a report is revised, include a statement whether the new report supersedes or supplements the older report.

**Block 12a. Distribution/Availability Statement.** Denotes public availability or limitations. Cite any availability to the public. Enter additional limitations or special markings in all capitals (e.g. NOFORN, REL, ITAR).

DOD - See DoDD 5230.24, "Distribution Statements on Technical Documents."

DOE - See authorities.

NASA - See Handbook NHB 2200.2.

NTIS - Leave blank.

**Block 12b. Distribution Code.**

DOD - Leave blank.

DOE - Enter DOE distribution categories from the Standard Distribution for Unclassified Scientific and Technical Reports.

NASA - Leave blank.

NTIS - Leave blank.

**Block 13. Abstract.** Include a brief (Maximum 200 words) factual summary of the most significant information contained in the report.

**Block 14. Subject Terms.** Keywords or phrases identifying major subjects in the report.

**Block 15. Number of Pages.** Enter the total number of pages.

**Block 16. Price Code.** Enter appropriate price code (NTIS only).

**Blocks 17. - 19. Security Classifications.** Self-explanatory. Enter U.S. Security Classification in accordance with U.S. Security Regulations (i.e., UNCLASSIFIED). If form contains classified information, stamp classification on the top and bottom of the page.

**Block 20. Limitation of Abstract.** This block must be completed to assign a limitation to the abstract. Enter either UL (unlimited) or SAR (same as report). An entry in this block is necessary if the abstract is to be limited. If blank, the abstract is assumed to be unlimited.